ALMA MATER STUDIORUM - UNIVERSITÀ DI BOLOGNA

DOTTORATO DI RICERCA IN
MONITORAGGIO E GESTIONE DELLE STRUTTURE E DELL'AMBIENTE - SEHM2

Ciclo XXXIII

08/A1 - Idraulica, Idrologia, Costruzioni Idrauliche e Marittime
ICAR/02 - Costruzioni Idrauliche e Marittime e Idrologia

INNOVATIVE TECHNIQUES FOR THE HYDRAULIC AND HYDROLOGICAL VARIABLES ASSESSMENT

Presentata da:
Giada Molari

Supervisore:
Prof. Alessio Domeneghetti

Co-supervisore:
Prof. Attilio Castellarin

Coordinatore del Dottorato:
Prof. Alessandro Marzani

Esame Finale - Anno 2021

Opposition is the mainspring of life,
the element of infinite progress.

Acknowledgements

I humbly take the opportunity to acknowledge all the people, institutions and public bodies that have contributed to this work. All these research activities were performed with the contribution of Travedona-Monate Municipality (Varese, Italy) under a research agreement with the Department of Civil, Chemical, Environmental and Materials Engineering (DICAM) of the University of Bologna.

The warmest thanks goes to my supervisor, Prof. Alessio Domeneghetti, for believing in me more than I could and for being the best role model I could wish for. I am very grateful to all my colleagues: thanks to my office mates Mattia and Lorenzo for having shared with me the everyday life, to Francesca for having involved me in the SMF world, to Simone for being the "top-fan" of my culinary experiments, to Alessio, Sara, Cristiana, Elena, Irene, Antonio, Roberto, Alberto, Attilio that, in their own way, played a part in making the PhD years serene. A work environment based on respect and collaboration. Having been part of it makes me lucky.

Many thanks to Hind Oubanas and Pierre Oliver Malaterre to host me at IRSTEA and for the research collaboration. It was a constitutive experience.

All this journey could not be possible without the support of people outside academic world. Thanks to my friends to be a constant in my life from several years. Thanks to the *magic* Lori, whose passion always lights up my thoughts. Thanks to my family to be near me in every moment. Thanks to you Matteo, for supporting me in less serene periods with patience and comprehension.

Abstract

This Thesis focuses on two main research topics: (1) the use of innovative techniques for the evaluation of main hydraulic variables of natural rivers (e.g. river bathymetry, discharge, water level) and (2) the monitoring and hydrological modelling of Monate Lake (Varese, Italy). Regarding the research topic (1), the work addresses three main issues: the river bathymetry estimation based on space-borne data, the river discharge assessment by means of Data Assimilation (DA) approaches, the use of satellite altimetry information in hydraulic modelling.

Notwithstanding the pivotal role of river bathymetric information in hydraulic applications, its availability is limited. In order to overcome the inability of satellite Digital Elevation Model (DEM)s in describing the submerged part of the river, the Slope-Break (SB) method, exclusively based on topographic information (i.e. river channel width and elevation), is proposed (Domeneghetti, 2016). A Matlab-tool (RiBEST) is proposed, based on the SB approach for an automatic estimation of river bathymetry, exploiting a satellite DEM (i.e. SRTM). Testing this approach on three different study areas (i.e., Po River (Italy), Limpopo River (Mozambique) and Clarence River (Australia)), the results are encouraging, demonstrating how SB method is suitable in the description of the submerged part. Moreover, the SRTM cross-sections modified by means of RiBEST are exploited to implement i) two 1-D hydraulic models for Po and Limpopo River, ii) a 2-D hydraulic model for Clarence River, underling the benefits of river bathymetry knowledge in the hydraulic modelling.

Secondly, the research refers to the assessment of DA approaches for river discharge estimation. In particular, a 4D-Var method is exploited, based solely on space-borne information (i.e. water surface elevations from SWOT) and global available data (i.e. prior discharge value from a global hydrological model - WBM). The challenge is to improve our capability to estimate the river discharge by using remotely sensed data only (e.g. cross-sections profiles derived from SRTM modified with RiBEST tool, water surface data observed from SWOT) referring to a 132-km Po River stretch. The results show a good representation of river discharge, in particular for low flows (i.e. 0 - 2000 m^3/s).

Thirdly, a comprehensive and cross-missions view of the potential of satellite altimetry

mission for hydraulic modelling calibration is addressed. Each satellite series (i.e. ENVISAT, TOPEX/Poseidon, Jason-2, etc...) has its own characteristics such as accuracy, spatial and temporal resolutions. The last one is the most limiting property in the use of data, thus Multi-Mission series (MM) are proposed, combining information provided by all single-missions. Generally, altimetry time series prove to be suitable in reproducing the observed water levels, while MM series ensures a uniform behaviour along the study area, providing additional benefits in case of low frequency series.
Regarding point (2), the main scope is the understanding of water dynamics of the Monate Lake (Varese, Italy) taking advantage of a monitoring network data and hydrological investigations. This work is dedicated to the implementation of semi-distributed conceptual models for a basin with seasonally variable catchment size. In particular, the variation of the additional groundwater watershed area is considered to be strictly dependent to precipitation variability. Generally, the proposed models reproduce the lake dynamics.

Contents

Premise

This PhD project takes part of the PhD program Structural and Environmental Health Monitoring and Management (SEHM^2) relative to the monitoring in general, spacing among several topics and application, touching different ambits of monitoring. Relevant examples are health monitoring of civil and industrial structures and infrastructures, performance monitoring of networks (gas, water, electric, telephone, road, rail, etc.), monitoring and managing air and hydrogeological systems. In particular, my PhD project has been funded by a convention between the Municipality of Travedona-Monate (Province of Varese, Italy) and DICAM (Department of Civil, Chemical and Environmental Engineering) of the University of Bologna.

For this reason the present work is divided into two parts. The Part 1 is relative to the investigation of innovative approaches for the study of hydraulic variables. The steep declining of the world's in-situ gauge stations of the last 30 years has led the research of alternative and/or complementary inland water measuring techniques. Particular importance is given to space-borne data thanks to the growing availability of satellite instruments and missions. The Chapter 1 presents a comparison between traditional (i.e. in-situ campaigns) and innovative approaches, listing a several literature investigations about river bathymetry, discharge and water levels estimation, topics explored in details in the following part of the thesis. The knowledge of river cross-section shape, and consequently of river bathymetry, is fundamental in order to implement hydraulic and hydrological model describing the water body behaviour realistically. Since the satellite DEM are unable to describe the submerged cross-section portion, several studies have widely investigated techniques to estimate the river *thalweg*. In the Chapter 2 a tool for the river bathymetry estimation is presented. Basing on a pure geometric approach for river depth assessment, this tool can automatically *correct* the cross-section profile provided by satellite information and evaluate hydraulic parameters (i.e. hydraulic radius, flow area, wetted perimeter). The benefits of this approach have been tested on hydraulic modelling for three different study cases.

Remote sensing approaches to measure hydraulic parameters (such as water surface elevation, river and lakes width) are strongly consolidated. Nevertheless, river discharge

estimation directly from satellite is still a current challenge. Data Assimilation (DA) methods are becoming increasingly popular in hydraulic-hydrological applications. They combine available information from observations (remotely sensed or in-situ) and mathematical models simulations to provide an optimal estimation of unknown variables (i.e., river discharge) and parameters (i.e., roughness coefficient, bed elevation). The Chapter 3 illustrates the estimation of river discharge using an algorithm implemented by the Institut national de recherche en sciences et technologies pour l'environnement et l'agriculture (IRSTEA) that combines hydraulic model and a DA approach. The prior bathymetric information is retrieved exploiting the tool presented in the previous chapter.

The final part is relative to the satellite altimetry information, whose use is now well consolidated for the hydraulic model calibration. The Chapter 4 aims to depict a wide comparison of different altimetry satellite missions, focusing on the main features characterising each satellite series. In particular, the temporal resolution and the number of observations can strongly restrict these satellite information in hydraulic applications. For this reason, an innovative approach to overcome these main limitations is presented.

The Part 2 is dedicated to the presentation of Monate Lake case study, the main motivation that have driven to the building of the monitoring network and the performed activities in collaboration with University of Bologna. In particular, the amount of measured data have allowed the implementation of hydrological model to study the lake behaviour in all its complexity.

Part 1

CHAPTER 1

Traditional and innovative methods for hydraulic variables estimation

The water you touch from rivers is the last of the one that went and the first of the one that comes. Similarly the present time.

Leonardo da Vinci
(1452 - 1519)

This Chapter contains:

1.1 Introduction

"The core of sustainable development and critical for socio-economic development, energy and food production, healthy ecosystems and for human survival itself; the heart of adaptation to climate change, serving as the crucial link between society and the environment", as United Nations (UN) defines *water*. As the global population grows, there is an increasing need to balance all of the competing commercial demands on water resources so that communities have enough for their needs. Continental waters provide water supply for various human activities. These mainly include water for drinking, irrigation, industrial and energy production. In accordance with Food and Agricultural Organization (FAO), agriculture and industry accounts for 70% and 19% of global water withdrawal respectively (Figure 1.1). Moreover at the human level, water cannot be seen in isolation from sanitation. Together, they are vital for reducing the global burden of disease and improving the health, education and economic productivity of populations.
Monitoring of inland waters is mandatory for a better understanding of the water cycle, sustainable management of water resources in various sectors at regional or catchment scale. It is also vital for forecasting natural hazards such as flooding events, which have major impact on economics. The 90% of natural disasters are weather-related, including floods and droughts (United Nations International Strategy fro Disaster Reduction (UNISDR), *The human cost of weather related disaster*, 2015); moreover, around two-thirds of the world's transboundary rivers do not have a cooperative management framework, affecting the efficiency of flooding events monitoring and control (Swedish International Water Institute (SIWI), *Transboundary waters: cooperation from source to sea*, 2018).
Caring of the surveillance of national territory for managing its own resources is the basic idea for the environmental conservation. A significant example is the United States Geological Survey (USGS) agency, born in 1879 with the task of classifying public land, examine geological structures, mineral resources and all elements of the United States domain. In particular the monitoring of surface and groundwater is entrusted to National Water Information System (NWIS): nowadays the information are available for about 1.7 millions of gauged stations in whole national territory, provided by manual and automatic procedures and freely available. Thinking on a global scale, the principal source of accessible data on river flows is the Global Runoff Data Centre (GRDC) operated by the German Federal Institute of Hydrology. The GRDC maintains a database of historic daily mean river flows, and some associated metadata, covering 6000 stations in over 120 countries.

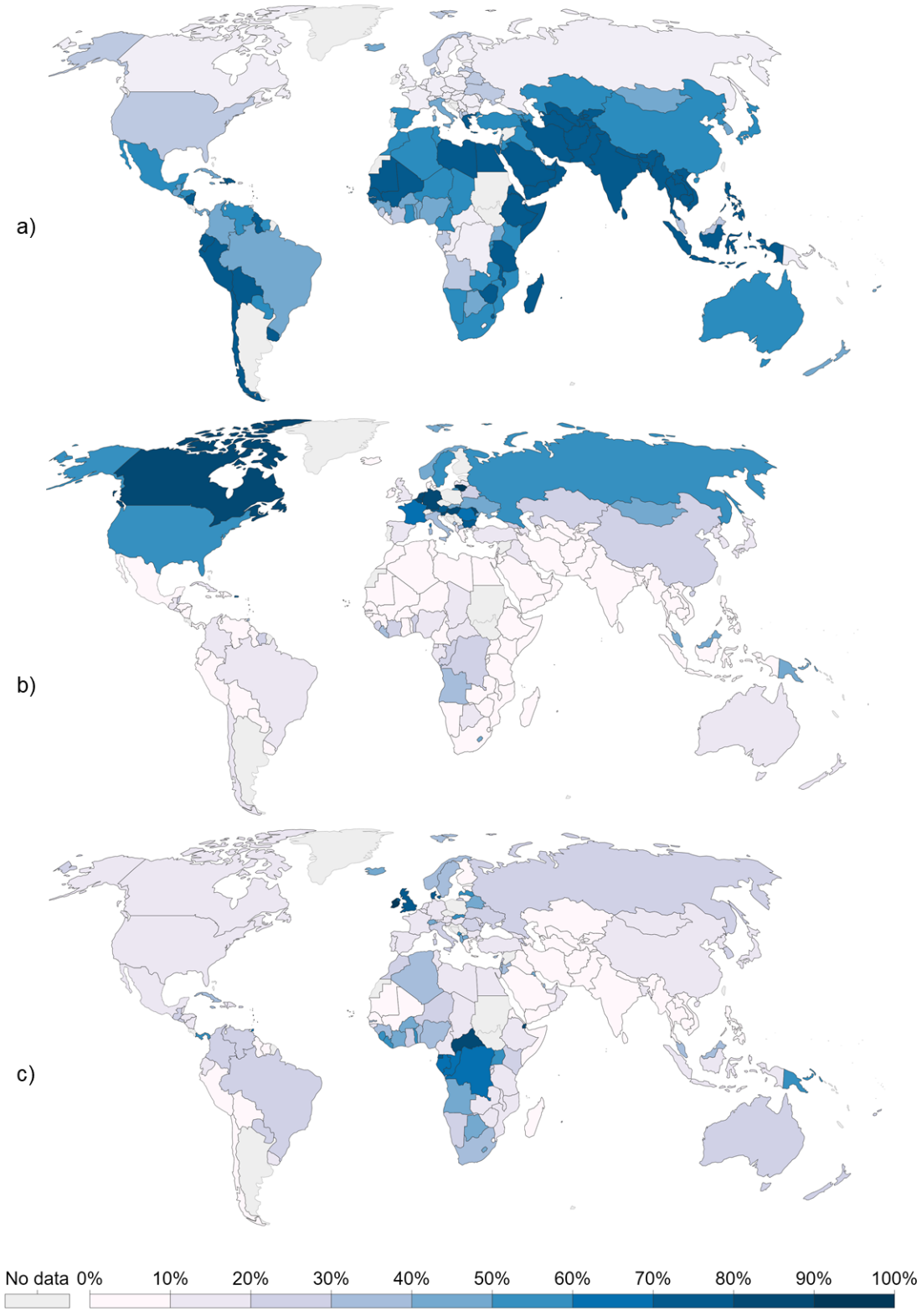

Figure 1.1: Agricultural (a)), industrial (b)) and municipal (c)) water as a share of total water withdrawals, 2005 (Ritchie, 2017).

Data are provided by countries (generally the National Hydrological Services) under a standard licence, enabling GRDC to make data available on request for non-commercial usage.

Despite of the pivotal role of in-situ information, the drop-off in measurements from the mid-1980s, due to the expensive cost of the measurement procedures (i.e. specific tools, qualified personnel, monitoring networks maintenance) and the operative difficulties for transboundary water or in remote areas, makes in-situ information hard to be collected for most of the water bodies in the world. Even in places where stream gauges exist, legal and institutional restrictions often make the data unavailable for scientific purposes. (Alsdorf and Lettenmaier (2003), Harmancioglu et al. (2003), Milzow et al. (2011), Gleason and Hamdan (2017), Figure 1.2). For this main reason, innovative water measuring techniques have caught on about 30 years ago. In particular, recent studies (see e.g. Schumann et al., 2009; Bates et al., 2013; Domeneghetti et al., 2014; Schumann et al., 2016) demonstrate the feasibility and potentially convenience of remote sensing data in various hydrological-hydraulic applications, especially in ungauged or poorly gauged areas.

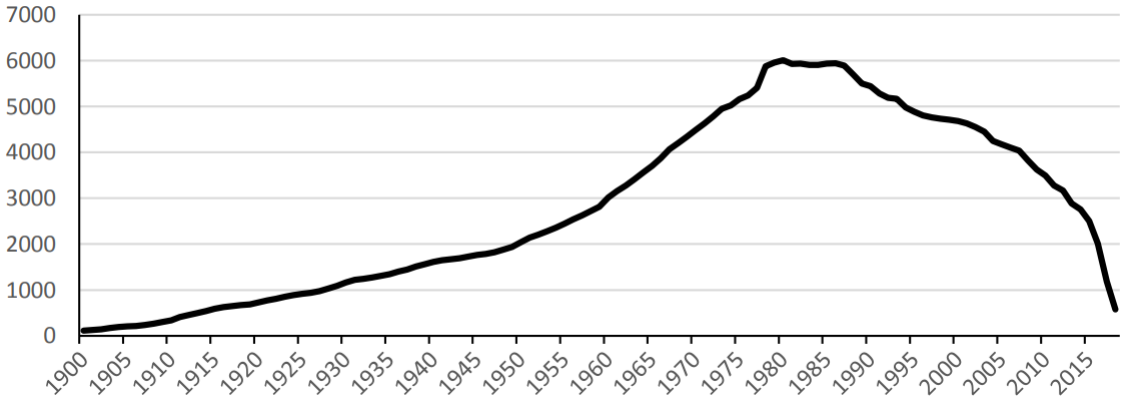

Figure 1.2: Number of GRDC stations providing daily data each year. ©GRDC

Remote sensing sensors detect and classify the objects and elements on Earth, using the sun as a source of illumination (passive sensors) or providing their own source of energy (active sensors). Most passive systems used by remote sensing applications operate in the visible, infrared, thermal infrared, and microwave portions of the electromagnetic spectrum. They include accelerometers, imaging radiometer and spectrometers, measuring land and sea surface temperature, vegetation properties, cloud and aerosol properties. The majority of active sensors operate in the microwave band of the electromagnetic spectrum, which gives them the ability to penetrate the atmosphere under most conditions. Radio Detection and Ranging (RADAR) sensors, altimeters and scatterometers are active sensors. These types of instruments are useful for measuring the vertical profiles of aerosols, forest structure, precipitation and winds, sea surface topography, and ice (Brivio

et al., 2006).

Each sensor is characterized by a series of resolutions (i.e. radiometric, spatial, spectral, temporal) depending on the satellite's orbit and sensor design (Campbell and Wynne, 2011). In particular, spatial resolution is defined by the size of each pixel within a digital image and the area on Earth's surface represented by that pixel, the temporal resolution is the time it takes for a satellite to complete an orbit and revisit the same observation area. These two information play an important role in how data from a sensor can be used.

Initially the exploitation of satellite data was dedicated to the monitoring of wide water bodies, such as oceans, seas, lakes (Birkett and Mason, 1995; Pereira-Cardenal et al., 2011). In the last decade several sensors and tools have been developed for the study of inland water bodies (Archer et al., 2018; Hawker et al., 2018; Shastry and Durand, 2019). Remote sensing have represented - and still represents - an appealing alternative means of obtaining several type of information. Potential advantages of a remote sensing approach include greater efficiency, expanded coverage, increased measurement frequency and lower cost respect with the traditional monitoring techniques. In addition, remote sensing methods provide exciting opportunities to examine long segments of rivers with continuous coverage and high spatial resolution. Since maintaining gauges in remote area puts field personnel at risk, *non-contact* methods are exploited to estimate hydraulic variables (i.e. streamflow, water levels) such as small unmanned aircraft systems (i.e. drones), helicopters, or fixed-wing aircraft. All this instruments, being very expensive, strongly affect the economical availability, limiting survey campaigns (Legleiter and Kinzel, 2020). The space-borne information often are freely available, allowing the assessment of not instrumented and remote areas.

Nevertheless these innovative approaches present some limitations. Depending on the sensor used, the data quality is function of the climate conditions (i.e. presence of clouds; see Batini et al., 2017). Moreover, limited spatial and temporal resolutions can strongly constrain the field of application (i.e. high detailed land description, hourly and fast water levels variations). In this context, several researches have aimed at proposing approaches exploiting space-borne data for the hydraulic variables estimation (i.e. water levels, river discharge, cross-section shape), highlighting how the satellite data can potentially be a valid alternative to in-situ information. The following sections (Sections 1.2, 1.3, 1.4) present the main research topics of this PhD, while Section 1.5 reports the main motivations and goals at the base of this work.

1.2 River bathymetry information: fundamental concepts, open problems and investigated estimation methods

Accurate modelling of river flow dynamics is fundamental for flood prediction as well as land management and risk analysis. Estimation of depth and flow velocity, and consequently of river discharge, is essential for floodplain risk assessment. The main difficulty in the implementation of hydraulic models is that they require an amount of different data (e.g., hydrological and topographic data), specific to the survey area; in particular, river bathymetric information is pivotal for the prediction of floodplain inundation (Neal et al., 2015).

The core input data for most environmental models is a topographic map of the study area in a digital form, or DEM. DEMs can be obtained from various combinations of surveying tools and data techniques spacing from traditional ground surveying such as total stations, various form of Global Positioning System (GPS) systems and echo sounders, topographic contour maps, or through remote sensing techniques applied to air or space-borne imagery acquired by Light Detection and Ranging (LiDAR), the Shuttle Radar Topography Mission (SRTM) or the Advanced Spaceborne Thermal Emission and Reflection Radiometer (ASTER). Each DEM has a different spatial resolution, which may affect the accuracy of model applications. Adoptable techniques of river geometry sampling range among traditional approaches and more innovative methodologies such as multibeam sonars mounted to ships (Conner and Tonina, 2014) or single beam sonars to small watercraft (Merwade et al., 2008; Pasternack and Senter, 2011).

Furthermore, even at the catchment scale, it is not economically and practically feasible to measure along the total length of a number of streams, especially considering that river geometry might not be stable over time (Buffington, 2012; Soar et al., 2017). These circumstances together drive to the fact that accurate bathymetry information is typically limited to developed areas and major rivers, while most part of the globe can count, almost exclusively, on remotely sensed topographic data, such as space-borne DEMs. Amongst available products, SRTM is nowadays available at almost global scale (i.e. covering about 80% of the globe) with a resolution of 1 arc-second (nearly 30 m resolution). In the last years, the relationship between geomorphologic land features and SRTM vertical elevations error has been widely investigated (Yan et al., 2015; Schumann et al., 2014; Iwahashi et al., 2017), and shown to be influenced by specific terrain characteristics (such as terrain slope, presence of buildings and tree canopy; Ludwig and Schneider, 2006).

Space-borne instruments can measure river water surface elevation, slope width, while river bottom and channel shape assessment is far more challenging (Alsdorf et al., 2007). The remote sensed information are affected by limitations, in particular for the reconstruction of the submerged part because of the radar inability of penetrating the water surface. In this context of data scarcity, the research community proposes different approaches to face the lack of river geometry information. Some studies combine the water levels and hydrodynamic models (Andreadis et al., 2007; Durand et al., 2008), meanwhile Neal et al. (2012a) propose to evaluate river bottom referring to empirical equations relating geometry to the catchment area (Leopold and Maddock, 1953). Legleiter and Roberts (2009) investigate the relationship among river thalweg and reflectance attenuation on the water column, using different optic sensors (i.e. ASTER, LANDSAT TM). An other line of research studies methodologies for river bathymetry determination during floods exploiting the principle of maximum entropy and flow velocity information, without the need of involving hydraulic quantities as energy slope and/or Manning's roughness (Moramarco and Singh, 2010; Moramarco et al., 2013). Mersel et al. (2013) investigated the possibility of estimating river bathymetry exploiting only water level and water width measured from satellite. Regardless of the approach adopted to infer the river bathymetry, the impact of a rough representation of the river geometry on a hydrodynamic model is still not completely depicted. Trigg et al. (2009) compared a one-dimensional (1-D) diffusive model based on simplified and rectangular cross sections with a hydrodynamic 1-D model based on a fully irregular channel. The outcomes underline the assumption of prismatic rectangular channel with flow area equivalent to the real one could reproduce water levels in large, shallow sloped rivers, while a proper simulation of floodplain water levels requires more detailed investigations. Similarly, Fewtrell et al. (2011) compared the skill of complex, fully irregular geometries and simplified rectangular geometries embedded in a 1-D hydrodynamic model coupled with a two-dimensional (2-D) one. They concluded that accurate estimates of the river conveyance capacity and cross section depth values were required for the predictions of far-field flood elevations.

Exploiting topographic relationship similar to those adopted by Mersel et al. (2013), Domeneghetti (2016) shown the potential of integrating simplified river bathymetry information into space-borne DEMs for the implementation of a 1-D hydraulic model. In particular, the study proved the potential for hydraulic modelling of spaceborne DEMs (e.g., SRTM) when enhanced by including the river bathymetry estimated based on remotely sensed data only.

The Chapter 2 further deals with river bathymetry estimation by presenting the RiBEST (River Bathymetry Estimation from SaTellite) tool, developed by the candidate: a Matlab-

based algorithm for automatic river depth detection and cross-section modification. Taking advantage of a DEM devoid of bathymetry information (i.e., satellite derived SRTM 30) RiBEST enables to (i) estimate cross-sections submerged portion; (ii) assess hydraulic parameters (such as flow area and hydraulic radius); (iii) modify river cross-sections including channel bathymetry. Beside RiBEST presentation, this study offers new insights on bathymetry estimation by proving the methodological soundness and tool robustness under different contexts: a) heavily human impacted river (Po River, Italy), b) remote areas (Limpopo River, Mozambique) and c) river partially constrained with vast floodplain areas (Clarence River, New South Wales, Australia). In addition, the methodology effectiveness is tested adopting two different hydraulic modelling schemes: 1-D (i.e. for Po and Limpopo Rivers) and 2-D models (i.e. Clarence River). In both cases, results are evaluated against those provided by numerical models (1-D and 2-D) implemented on detailed topography information.

1.3 Remote sensing data and mathematical models for river discharge assessment

River flow and hydrometric data are the essential foundations upon which improved river and water management strategies can be developed. River discharge is an important hydrological quantity that summarizes how the channelized streamflow forms combining climatological (i.e. precipitation) and geographical (i.e. soil moisture, land cover) factors. Detailed river flow information are pivotal for a wide variety of applications at the base of economical development and human safe, ranging among the management of water resources and flood warning and alleviation schemes. Observational records allow to interpreting hydrological trends, thus to develop approach of flood and drought episodes prediction (National River Flow Archive (NRFA)).
Commonly, the river discharge is equal to the product of the stream's cross-section area and its mean velocity, whose in-situ measurements are frequently non-trivial to determine. Among the traditional instruments for measuring the water velocity the hydrometric paddle-wheel is able to estimate the punctual speed, quantifying the number of rotations per minute performed by the propeller placed at the end of the fixed body. In streams featured by high depth and strong current, this tool has to be used in suspension; for low speed, it has to be fixed to pointed rods on the bottom. Other in-situ techniques are based on the use of ultrasound placed near the banks of the channel, measuring the speed of current that crosses the entire section river, quantifying the time spent in his displacement between two predetermined points.

As the measuring of discharge directly from space is not possible, some studies infer it by using remotely sensed hydraulic variables (i.e. water levels, surface velocity): in this way, different quantities can be measured separately through remote sensing and used, successively, for discharge estimation (Bjerklie et al., 2003; Legleiter et al., 2020). The analysis of Kinzel and Legleiter (2019) is based on the computation of river discharge exploiting flow velocity via Particle Image Velocimetry (PIV) of thermal image time series and cross-section area provided by a bathymetric LiDAR. Meanwhile since the strong correlation between river water levels and discharge, approaches based on satellite altimetry information prove a valid alternative for the river flow estimation (Birkinshaw et al., 2010; Tarpanelli et al., 2013b). In this context Smith and Pavelsky (2008) and Tarpanelli et al. (2011) investigate the potential of MODerate resolution Imaging Spectroradiometer (MODIS) for river discharge estimation: featured by moderate spatial resolution (i.e. 250 m) and by a short revising time interval this satellite product is suitable for flow dynamics and flood mapping representation. Moramarco et al. (2019) propose an approach based on the entropy theory for discharge monitoring, combining ground and satellite data of hydraulic variables (i.e., surface velocity, channel width, stage). In particular, MODIS datasets and ENVISAT altimetry provide velocity and surface water level, respectively. From 2022, the Surface Water and Ocean Topography (SWOT) mission will provide river discharge estimates globally from space, guaranteeing a good spatial resolution and coverage. Since its potential, many researches (Pavelsky and Durand, 2012; Gleason and Smith, 2014; Paiva et al., 2015; Durand et al., 2016) investigate the possibility of estimating river discharge using SWOT data by mean of statistical models and algorithms (i.e. River Kriging-RK). In particular, Durand et al. (2016) compares five several discharge algorithms evaluated on 19 study cases, reaching encouraging outcomes.
An other branch of studies seek the potential of mathematical approaches such as Data Assimilation (DA) for the assessment of hydraulic variables.

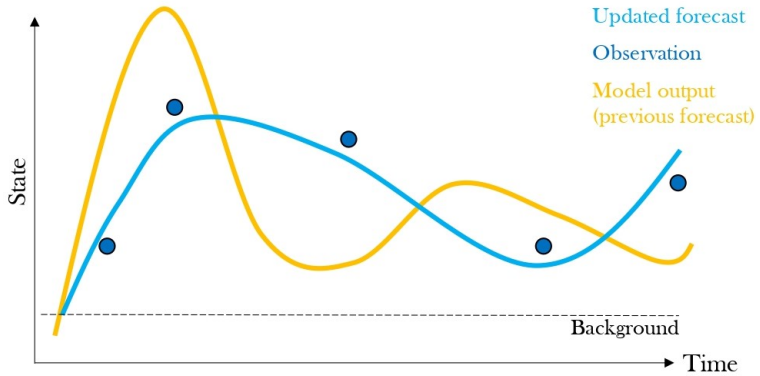

Figure 1.3: Schematic representation of DA methods.

At the beginning of 21th century DA started to be suitable on hydrological and hydraulic applications (Gauthier et al., 1999; Roux and Dartus, 2004; Honnorat et al., 2009). DA methods combine observations with model output with the objective of improving the latter: the main goal is to predict the state of a system, or its future, in the best possible way. Starting from a predicted state (i.e. hydraulic model output) affected by errors and exploiting a prior information (i.e. background), DA approaches obtain an updated forecast of the system closer to a series of observations by means of a fitting process (Figure 1.3). In geophysical science it refers to the concept of *inverse problem*: contrary to a *direct problem* that is based on cause-effect sequence, it aims to identify the unknown causes of given known consequences (Bertero et al., 2001).
Most of proposed DA methods in literature are based on the same statistical Bayesian theory proposed by Bayes (1763) and reformulated later by Laplace (1820) in the framework of statistical inference. Among them, variational DA has been the preferable approaches in operational geophysical applications. They seeks to find the best estimate of the unknown quantities via the minimization of a functional penalizing weighted distance from the observations and from the background, over a finite time window, called "assimilation window" (Oubanas, 2018). In particular, the 4D-Var method has been used in several applications, being adapted for nonlinear systems where heterogeneous variables are estimated simultaneously (Oubanas, 2018). The estimation of river discharge by mean DA approaches is widely investigated (Neal et al., 2009; Oubanas et al., 2018a; Wang et al., 2018; Li et al., 2020): starting from an hydraulic model characterized by uncertainties (i.e. river bathymetry, bed roughness coefficient) and a series of observations, the DA method can provide the river discharge trend on an observation period. Notwithstanding more inaccuracy and uncertainty can be introduced, recent approaches attempt to fully exploit remote sensed and globally-available data (i.e. satellite altimetry information and DEMs) in order to be suitable also in ungauged basins.
Moving towards to this perspective, the Chapter 3 illustrates the use of variational DA methods for the river discharge assessment basing on satellite information (i.e. SWOT water levels). A full Saint-Venant 1.5D-network hydraulic model is implemented on the Po River cross-sections derived from satellite DEM (i.e. SRTM). The 4D-Var estimation problem determinates discharge as well as the spatially distributed bed roughness coefficient simultaneously. This research topic was developed in collaboration with the research team at IRSTEA (Montpellier, France).

1.4 Measuring river water levels from satellite altimetry data: main limits and alternative approaches

Over the last thirty years hydraulic modelling has developed to such an extent that it can now provide high-quality flood risk maps (Merz et al., 2010), damage assessment (Luino et al., 2009), water resource management (Loucks and Van Beek, 2005), real-time flood forecasting and dynamic perspective in case of future scenarios (Bronstert, 2003). Hydraulic modelling describes the flood routing and, hence, tracks the propagation of a flood wave given as an input at an upstream location of a river channel to any downstream locations. The routing model requires an accurate geometric description of the river channel and floodplains, reliable input of river discharge and the calibration of the roughness parameter, considered as the most important factor that has an impact on predicting flow characteristics (Aronica et al., 1998; Bates and Anderson, 1996; Pappenberger et al., 2005). The model calibration generally consists in tuning the roughness parameter to minimize the misfit between simulated and observed output represented by flow or water level hydrographs. Typically, the calibration is done by using water level or discharge observations gathered at the gauged stations available along the river. Recently, scientific literature is enriched by studies on the integration of remote sensing and ground observations for hydraulic model calibration. Numerous examples use the flood extent derived by the backscatter value of Synthetic Aperture Radar (SAR) images to calibrate the roughness parameter (Andreadis and Schumann, 2014; Schumann et al., 2014; Wood et al., 2016; Matgen et al., 2011; Tarpanelli et al., 2013c); in some cases considering also the uncertainty in the flood extraction (Di Baldassarre and Montanari, 2009; Giustarini et al., 2015). Directly related to the water surface elevation, satellite altimetry has demonstrated its large potential in the calibration of 1-D or 2-D hydraulic models (Domeneghetti et al., 2014; O'Loughlin et al., 2013; Yan et al., 2015). Neal et al. (2012b) calibrated the hydraulic model LISFLOOD-FP for an 800 km reach of the Niger river in Mali using the laser altimetry data from Ice, Cloud and land Elevation Satellite (ICEsat). Differently from radar altimetry data that are collected with a given repeat period at the same locations, ICESat does not produce repeat-track measurements and, although considered the most accurate source of altimetry information, the hydrological community is still sceptical about monitoring rivers in a different way from the traditional adoption of fixed gauging stations (O'Loughlin et al., 2016). Similarly, CryoSat-2 satellite suffers from a limited use due to the almost annual repeat cycle (i.e., 369 days), which is considered

inadequate to represent river dynamics. However, its dense spatial sampling (about 7.5 km at the equator) can be extremely useful in deriving water level profiles that normally cannot be achieved. Schneider et al. (2018) used CryoSat-2 water level data to calibrate the Manning roughness coefficient each 10 km over the Po river main channel by using the DHI Mike 11 software (Liang et al., 2015). Compared with values calibrated through in situ measurements, CryoSat-2 showed a strong potential in calibrating the roughness coefficient at a detailed level with the consequent reduction of the over- and under-estimation of the high flows (Jiang et al., 2019). Concerning short-repeat and fixed-orbit missions radar altimetry (i.e., ERS-2, Envisat, and Jason-2), several examples have demonstrated their valid contribution in supporting the ground network for describing the hydrometric regime (Garambois and Monnier, 2015) and the potential benefits expected in case of its integration with in situ data (Domeneghetti et al., 2014). Most of these studies have focused on rivers larger in width than about 300 m, a limitation imposed by the along-track spatial resolution of delay/Doppler altimetry. The Fully Focused SAR (FF-SAR) processing, however, improves the along-track resolution of SAR altimetry up to the theoretical threshold of half of the antenna length (Egido and Smith, 2016; Vignudelli et al., 2019). Kleinherenbrink et al. (2020) have implemented the FF-SAR algorithm over lakes, canals, and ditches in Netherlands using CryoSat-2 full-bit-rate data. For cases where the altimetry track crosses the water bodies in a near-perpendicular angle, they have successfully derived the water level of a ditch as small as 5 m in width and located only 10 m away from a canal. Though more studies are required to indicate the potentials and limitations of FF-SAR, it is expected that the method would open an unprecedented opportunity to monitor smaller water bodies. Moreover, when the future SWOT mission will be fully operational, for rivers wider than 100 m, a 2-D river mapping at 10-70 m resolution will be available (Biancamaria et al., 2016).

Concerning the use of short-repeat and fixed-orbit missions radar altimetry for the calibration of the hydraulic model, two limitations are the most relevant and worth to be analysed: the length (duration) of the time series and the revisit time of the satellite. The importance of the duration (i.e., years of observation or number of overpasses) of the satellite mission has been analysed by Domeneghetti et al. (2015a) who showed its impact on the estimation of the roughness coefficient. In particular, they found that sample sizes of 2.5 years can be considered sufficient to the calibration process in case of using ERS-2 and Envisat time series. However, an extension of similar investigations to other satellites is desirable to assess the potential of current and past altimetry missions for hydraulic simulations. Also, the revisit time, typically 10 to 35 days for altimetry missions, represents a limitation for hydrodynamic applications. A possible solution is the development

of approaches that consider the use of multiple missions (MM) to derive densified time series in specific locations. Tourian et al. (2016) transferred the water level information coming from four satellite missions (Jason-2, Envisat, SARAL and CryoSat-2) and, hence, several virtual stations, to specific locations of the river coincident with the ground monitoring stations along the Po, Mississippi, Congo and Danube rivers. The combination of the altimetry data has been carried out with the hydraulic concepts of wave travel time and celerity of the flow calculated with the geometric characteristics of the river, such as length of the reach, slope and width. A successive study of (Tourian et al., 2017) analysed a similar approach over the Niger river and obtained river discharge by assimilating altimetric and in situ river discharge with a Kalman filter approach. Boergens et al. (2017) integrated water level measurements of Envisat, SARAL and Jason-2 by using ordinary kriging in the main channel of the Mekong River. All these attempts to increase the frequency of sampling of the river water surface are valuable contributions especially for hydrological applications and for deriving more frequent discharge time series. However, the value of MM time series has never been tested in hydraulic modelling.

Moving from previous considerations, the present work investigates three main aspects that are still only partially analysed in the literature:

1) the comparison of the available altimetry data in terms of their performance for the calibration of hydraulic models. Specifically, the analysis provides a comprehensive comparison of different satellite altimetry products available to the research community and covering nearly 27 years, such as: Envisat (E), Envisat extended mission (EX), TOPEX/-Poseidon (TP), SARAL/AltiKa (SA), Jason-2 (J2) and Jason-3 (J3), Sentinel 3A (S3A) and Sentinel 3B (S3B). Despite not directly analysed, the potential of ERS and CryoSat is also presented;

2) the assessment of the effect of the record length (i.e., number of available satellite measurements, in relation to different data products) on the calibration reliability. The study investigates the possible accuracy of the model calibration in relation to the record length of the altimetry product adopted for its execution. This info could be beneficial not only at the early stages of a mission, but also when historical time series are limited in length (perhaps due to missing values or mission interruption). Findings of such evaluation might serve a modeller when called to evaluate the extent of the calibration period;

3) the potential use of the use of MM satellite time series in the process of hydraulic model calibration. These synthetic altimetry time series result from the combination of different single-mission time series and overcome the spatial and temporal sampling limits that characterize a given single mission (Tourian et al., 2016). The construction of MM time series represents a recent frontier towards a larger exploitation of altimetry data provided

from the overall set of past and on-going satellite missions. Thus, the evaluation of its potential for the implementation of an accurate and reliable hydraulic model constitutes an element of interest for the hydrologic community.
Although not claiming to provide a general statement and ranking of the altimetry products, this study aims at delivering a comprehensive and cross-missions view of the potential of current and past altimetry data. The analysis is implemented along the Po river in the stretch between the gauged stations of Borgoforte (basin area equal to 62.450 km^2) and Pontelagoscuro (basin area equal to 70.091 km^2), for a direct comparison with other studies. The hydraulic simulation is carried out with the Hydrologic Engineering Center's River Analysis System (HEC-RAS) software package (Hydrologic Engineering Center, 2001) in a quasi-2D configuration. This study is presented in Domeneghetti et al. (2021).

1.5 Research questions

As introduced in the previous section, the use of satellite data in hydraulic and hydrological applications is common and continuously increasing. However, there are still a number of open issues concerning its potential and fields of applications. The lack of global datasets of hydraulic variables of interest (such as discharge, river depth, river width) represents a strong restriction for investigating variables relationships and hydraulic modelling. In this context, the use of satellite information can give a push in this sense, offering new solutions and perspectives for many hydrological and hydraulic applications.
Remote sensing products allow to examine remote areas, providing the opportunity of investigating also ungauged water bodies. Notwithstanding the quasi global coverage of satellite data, thinking at global scale is always complex. For example, the available sensors for discharge estimation limit the analysis of water courses characterized by remarkable dimensions (widths of a few hundred meters). SWOT will partly overcome these limits by observing water courses with a width of 50-100 m worldwide. Although the remarkable step forward, it follows that a large part of existing rivers will remain invisible to satellite sensors. Several studies investigate criteria that, based on topographic and hydrological information relative to the main streams, allow the extraction of more detailed information along the non-instrumented and non-detectable tributary branches. The main objective is therefore the creation of large-scale hydraulic variable datasets (Beck et al., 2016).
In this context, this dissertation aims to present some innovative approaches for the mon-

itoring, or the estimation, of hydraulic and hydrological variables. In particular, the proposed approaches focus on the use of specific space-borne information (e.g. space-borne DTM, satellite altimetry), analysing in details limitations and potential of their use.

The common thread of the proposed investigation is the understanding of how, and in which measure, the satellite data could integrate, substitute or be complementary to traditional measuring techniques for some hydraulic and hydrological applications. Although a single answer would be inappropriate, the potential of the satellite data is a function of the user's needs of the satellite product. Undoubtedly, the birth of satellite monitoring brought new prospectives in hydraulic applications, mainly for its positive economic impact on monitoring activities, being most of the space-borne products freely-available.

Among most commonly used satellite-derived data for hydraulic applications there are Digital Terrain Models (DTM). The spatial resolution is discriminating in the choice of these satellite products. Analysis relative to the description of river channel geometry does indeed become troublesome if the DEM pixel size has the same order of magnitude of river width. On the contrary, DEMs featured by rougher definition can be suitable for large scale studies, decreasing the analysis computational costs. Moreover, the user has to consider bias and inaccuracy characterizing the DEM: Chapter 3 refers to SRTM-30 (i.e. 30 meters) since the wide amount of researches relative to its elevation bias and limitations.

Also, in the ambit of satellite altimetry, the temporal frequency of satellite overpasses, number of available observations in a period of interest and data accuracy strongly influence the range of applicability of these satellite products (Chapter 4). Last but not least, the reliability of proposed methods exploiting satellite data plays an important role; for this reason all the studies proposed in the Thesis have been validated presenting a direct comparison with in-situ measurements.

The first part of this thesis focuses on the river bathymetry estimation, pivotal issue for hydraulic modelling and applications. The Chapter 2 presents an automatic tool (RiBEST) for river hydraulic parameters assessment (i.e., river thalweg, flow area, wetted perimeter, hydraulic radius), exploiting satellite DEMs (i.e., SRTM). The benefits of this approach have been tested on hydraulic modelling for three different study cases: a) an heavily human impacted river (Po River, Italy), b) a naturally shaped river in remote areas (Limpopo River, Mozambique) and c) a river partially constrained with vast floodplain areas (Clarence River, New South Wales, Australia). For this reason, the first research questions is:

Can the integration of a simplified river bathymetry description into a space-borne DEM sustain proper 1-D and 2-D hydraulic modelling?

Chapter 3 regards the assessment of river discharge. Since its impossibility to be measured directly from satellite, this work aims to exploit space-borne information (i.e., water surface elevation from SWOT) in a DA framework for the estimation of river flows. The proposed 4D-Var method, implemented in collaboration with IRSTEA (Montpellier, France), aims at combining available satellite observations with hydraulic model output (i.e., Simulation and Integration of Controls for Channels (SIC^2)), assessing river discharge and Strickler coefficient at the same time. The inaccuracies of observations and in the description of river channel can affect the estimation process. Starting from this consideration, the aim of this research is to exploit cross-sections profile derived from RiBEST and thus posing the following question:

How a better knowledge of the river shape (e.g. river bathymetry) might impact the discharge estimating using DA techniques?

The final part (Chapter 4) is dedicated to the investigation of the use of satellite altimetry information in the hydraulic model calibration. Several satellite missions are considered (i.e., Envisat, Envisat extended mission, TOPEX/Poseidon, SARAL/AltiKa, Jason-2 and Jason-3, Sentinel 3A and Sentinel 3B) with the objective of evaluating their performance in hydraulic model calibration. Moreover, an innovative dataset, Multi-Mission series, for overcoming the main satellite limitations (i.e., time resolution, number of data) is tested. Thus, the main research questions that this work investigation attempts to answer are:

Which satellite altimetry series are more suitable for hydraulic model calibration? Can multi-mission approach overcome single-mission limitations?

CHAPTER 2

RiBEST: a tool for the river bathymetry and hydraulic parameters assessment

Try to change our traditional attitude towards building programs. Instead of imagining that our main job is to instruct a computer on what to do, let's instead focus on explaining to humans what we want a computer to do.

Donald Knuth

This Chapter contains:

2.1 Slope Break Method (SB): fully-geometric approach for bathymetry estimation

As introduced before (see Section 1.2), satellite DEMs are unable of describing the river submerged part, not allowing a reliable river cross-section reconstruction. This strong limitation have induced the research community of investigating approaches to improve the representativeness of river geometry in satellite products. In particular, several morphological methods have been proposed in the literature. Among more complex approaches, the Slope Break Method (SB) considers two linear relationships between the river section width (w) and the related height (h; expressed as elevation in meter a.s.l.), one referred to low flow condition and one for moderate - high flows (Mersel et al., 2013; Domeneghetti, 2016).

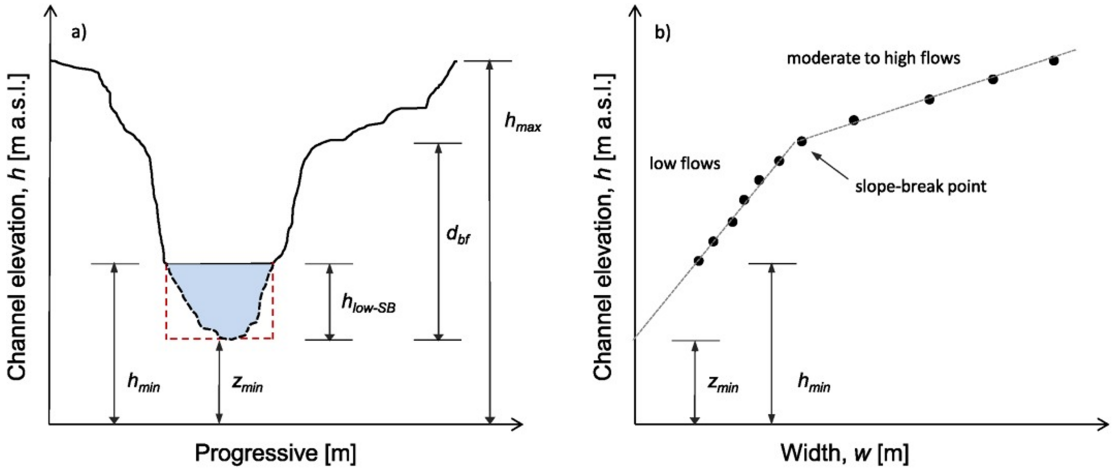

Figure 2.1: On the left: a generic river cross-section with real submerged part (black) and reconstructed one (dash red). On the right: empirical relationship among width (w) and elevation (h) (Domeneghetti, 2016)

Starting from the minimum gauged water level (h_{min} Figure 2.1), SB extrapolates w-h relationships for a series of elevations with an incremental step (e.g., 50 cm). The identification of linear links is performed computing the derivatives (i.e. finite forward difference; dh/dw) for all the possible h-w pairs. The mean derivative ($\overline{dh/dw}$) is calculated for four initial points, considering the subsequent dh/dw values as long as they deviate from $\overline{dh/dw}$ for a value lower than 40%. At the h-w pair where this hypothesis is not satisfied (that is an abrupt change on dh/dw value) Slope-Break point is found and cross-section (CS) thalweg (z_{min} Figure 2.1) can be identified, exploiting the dh/dw computed referring to at least five w-h couples below the Slope-Break point. The CS is thus called "optimal" for the SB approach application. The number of w-h pairs considered as threshold is a

user-defined parameter introduced to limit the risk of adopting misleading relationships based on a limited CS portion.
Mersel et al. (2013) proved the validity of the SB method for bathymetry estimation using detailed topographic information available along several rivers located in different regions (namely, Gange, Upper Mississipi, Illinois and Rio Grande rivers). Domeneghetti (2016) investigated the SB potential for enhancing the topography description ensured by satellite-sensed DEM (such as the SRTM) and for estimating the decrease of model accuracy expected in case of lack of finer data. The SB method does not require in situ information and is solely based on topographic data, easy gettable from space-borne DEMs. It proves reliable in the reconstruction of the river geometry, allowing the implementation of a 1-D hydraulic model with satisfying performances (i.e., Mean Absolute Error (MAE) of 0.27 m and Root Mean Square Error (RMSE) of 0.35 m respect with the benchmark model). Findings of this latter study emphasized the potential of space-borne DEMs embedding bathymetry information to sustain large-scale analysis and global inundation modelling.

2.2 RiBEST: River Bathymetry Estimation from Satellite

RiBEST tool is a Matlab-based software applying SB method for river bathymetry estimation. The tool has been conceived in order to be adaptable to multiple topographic sources (DEM of different resolution and origin) and different contexts (data-poor or data-rich areas). As a matter of fact, inputs required are limited to the channel centerline of the river of interest and a DEM of the area (e.g., SRTM). This characteristic makes the tool straightforward and versatile. Flowchart of Figure 2.2 describes RiBEST's structure, which can be divided into four main sessions.

Part 1: Input reading
The tool requests two mandatory inputs: a DEM (e.g., space-borne data such as SRTM) and the centerline of the river stretch of interest. DEM information (i.e. spatial resolution, raster vertices coordinates) are automatically extracted and no direct inputs are demanded to the user. The tool can manage raster of any spatial resolutions provided as geotiff data type. River centerline identifies the planimetric extension of the river stretch of interest and is provided by the user as a shape file. DEM and shapefile must have the same reference system (i.e. with plane or geographic coordinates).

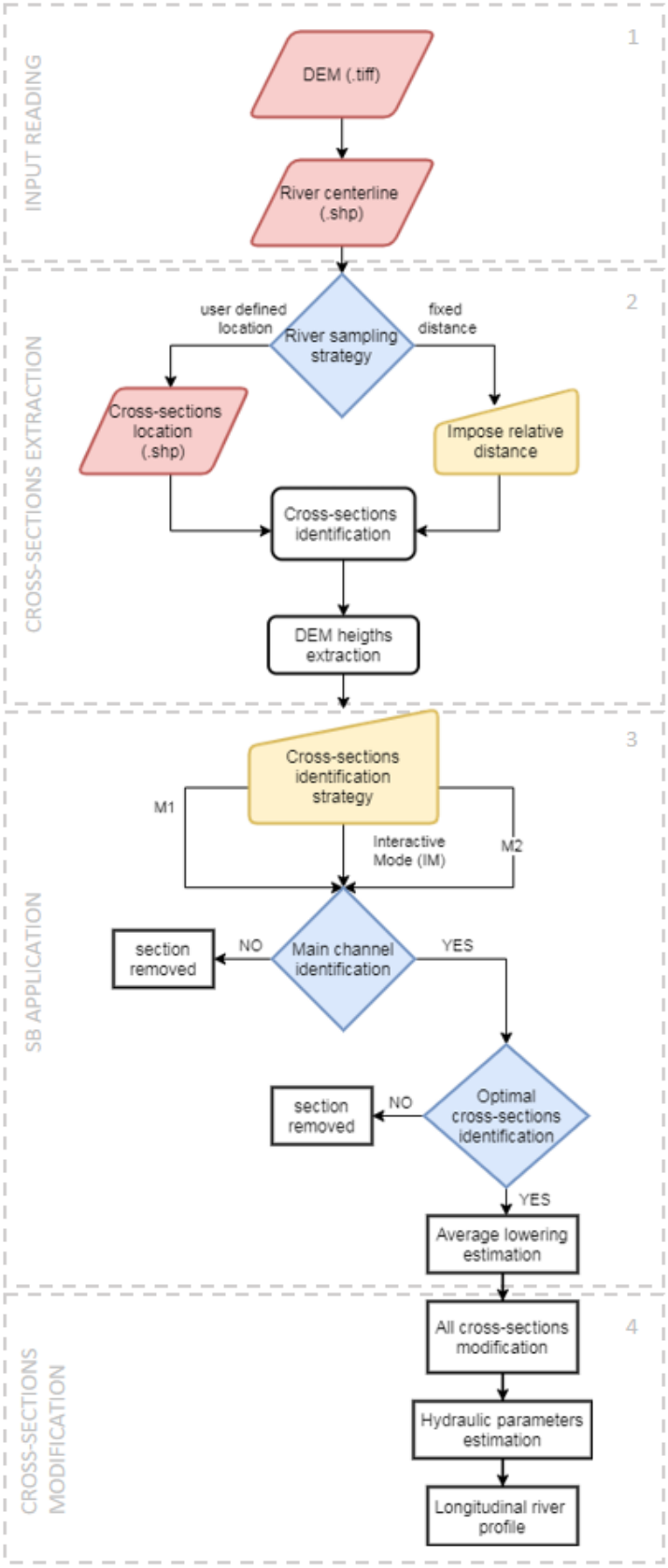

Figure 2.2: Flowchart of RiBEST tool structure.

Part 2: CS extraction

Regarding CSs position, the user can proceed with two options: "user defined location" or "fixed distance sampling". In the first case, CSs position is imposed by means of a shapefile provided by the user. Alternatively, the code automatically generates cross-sections perpendicular to the river centerline adopting a fixed step (e.g., 300 m, 500 m, etc.) indicated by the user. Once identified, the tool extracts the terrain elevation at each CS considering a user defined width.

Part 3: SB application

CS thalweg (z_{min}, Figure 2.1) is assessed after the identification of a linear relationship among w-h couples (five, at least) sampled below the SB point. Referring to low flow conditions, this relationship is characteristic of the main river channel, which is typically different from the relationship eventually identified among w-h couples located in the floodplains and relative to medium-high flows. Starting from this consideration, the correct identification of the main channel within each CS is fundamental to yearn for a realistic bathymetry estimation. RiBEST automatically selects the main channel exploiting two different methods. The first approach (M1) locates the channel as the river portion delimited by the highest points on the right and left side of the river centerline (upper panel, Figure 2.3); the second one (M2), moving separately to left and right from the centerline, delimits the main channel by looking for points having elevation equal or higher than previous one (bottom panel, Figure 2.3). Although flexible, these selection strategies might not ensure a proper identification of the main channel in every circumstance; perhaps, secondary channels might interfere with main channel selection in case of M1 approach, while M2 may fail due to discontinuities in river bed elevations. In order to overcome these limitations the modeller can adopt a third approach, namely IM, Interactive Method, which allows the user to check and choose the approach (M1 or M2) considered as the most appropriate for each CS. Adopting IM mode, the user can choose the best main channel selection strategy or remove the cross-section from SB application. Once the main channel is selected, the tool calculates the river channel width associated with potential water surface elevations sampled within the channel with a constant step of 50 cm. A counter quantifies points (i.e., the w-h couples) for which the mean derivative ($\overline{dh/dw}$) is computed. It considers the four initial points and the subsequent dh/dw values as long as they deviate from $\overline{dh/dw}$ for a value lower than 40%. If the counter is at least five, the section is optimal; vice versa it is neglected for the average lowering estimation. High dh/dw values imply poor channel width variation, typical feature of limited dimensions rivers.

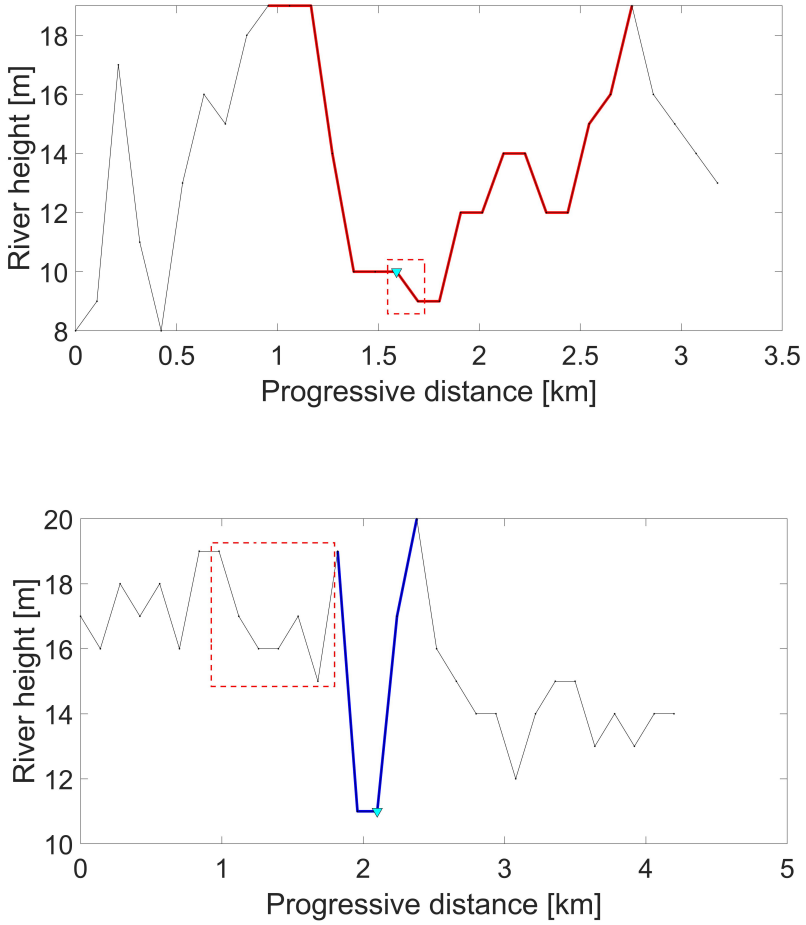

Figure 2.3: Upper panel reports an example of river channel selection using M1 (red line): the discontinuity in the river bed (red dashed line) makes the M2 selection not representative. Bottom panel depicts river channel selected by means M2 (blue line): in this case M1 would consider also the secondary channel (red dashed line) compromising the following process of bathymetry estimation. For both the images, satellite-derived CS profile and river channel centerline are represented by black line and light blue triangle, respectively.

Part 4: Cross-section geometry modification and hydraulic parameters estimation

The h-w values are linearly interpolated to find h value relative to w null (z_{min}). The difference between h_{min} and z_{min} represents the CS lowering to be applied in order to correct CS profile. An average lowering is calculated referring to optimal CS only and applied to the overall reach. RiBEST tool provides the modified CS profile, proposing two different CS shapes. In the first case, the average lowering value is applied to the segment consisting from all the points at the river centreline height (i.e. rectangular profile, upper panel Figure 2.4); in the second option, only segment central point depth is increased (i.e. triangular shape, upper panel Figure 2.4). For all the CSs for which the fluvial axis has a different height respect with adjacent points (thus h_{min} refers only to a single point instead of a segment), geometric modification is not applied.

Once CS are modified, RiBEST can evaluate flow area and hydraulic radius. Under full

channel hypothesis (i.e. water level in correspondence of the maximum channel elevation), flow area (A) and wetted perimeter (w_p) are calculated as sum of areas and segments between CS point couples respectively (bottom panel Figure 2.4). The hydraulic radius (R) is expressed as A and w_p ratio.

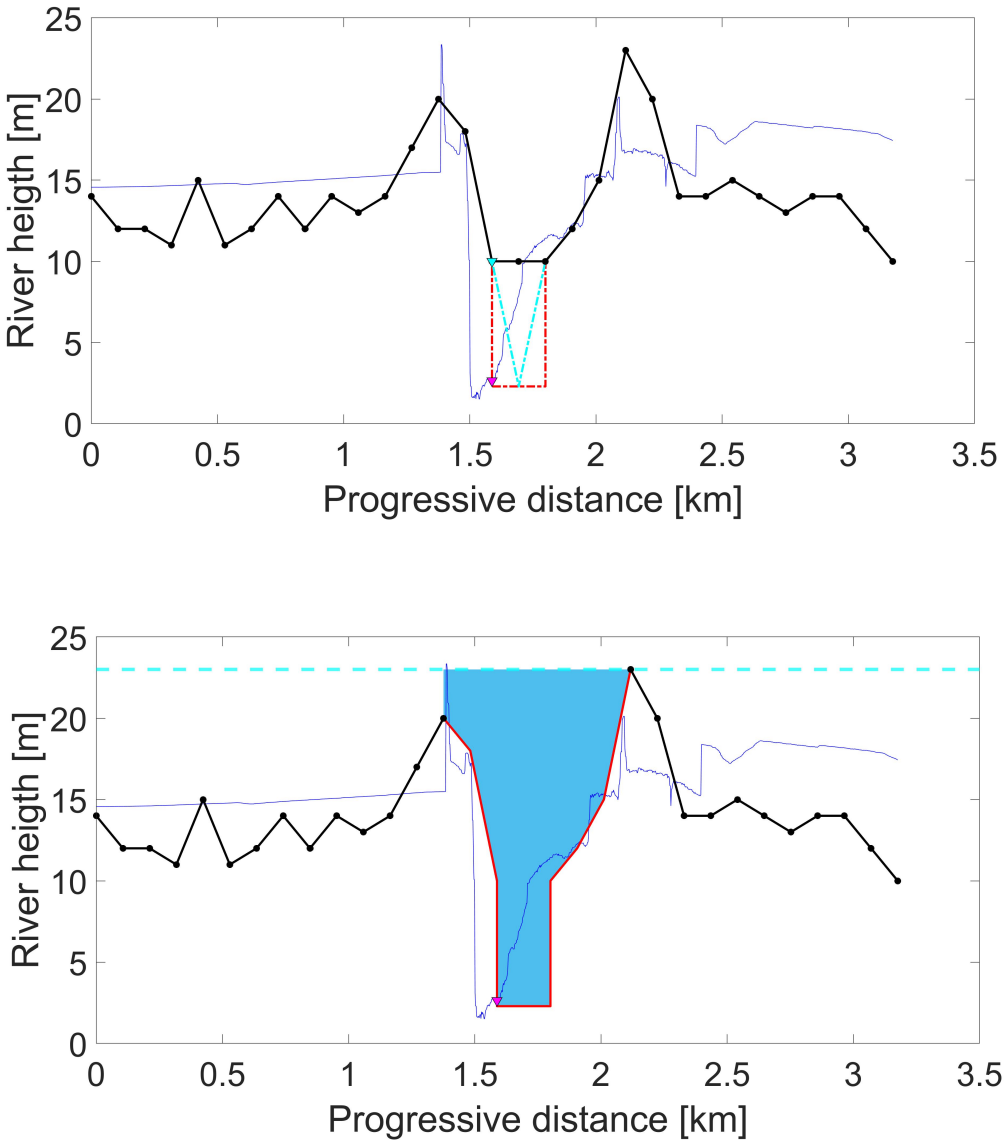

Figure 2.4: Upper panel: the satellite DEM CS (black line) after the geometric modification (dashed red and light blue lines); the blue profile is the reference one (i.e. LiDAR integrated with bathymetric in-situ information). Bottom panel: evaluation of flow area (blue area) and wetted perimeter (red line) of the main channel below the maximum water height from satellite DEM (dashed light blue line).

2.3 RiBEST analysis in different application contexts

2.3.1 Study areas and available in-situ data

To test RiBEST applicability and robustness, three different areas have been investigated: Po River (Italy), an example of heavily human impacted river, Limpopo River (Mozambique) located in a remote areas and Clarence River (New South Wales, Australia) featured by the presence of vast floodplains. The choice falls on the following river reaches for several reasons. Firstly, the river width is generally greater than the spatial resolution of adopted satellite DEM (i.e. Po river width spans 200 and 500 meters, Limpopo 100-700 m and Clarence 150-800 m). Moreover, these stretches are sinuous and unbraided, presenting a single-channel shape, a condition under which the SB method have been developed (see Part 3 Section 2.2). Finally, ground surveyed data are available in all cases (i.e. detailed in-situ information, water levels data) enabling the validation of model application.

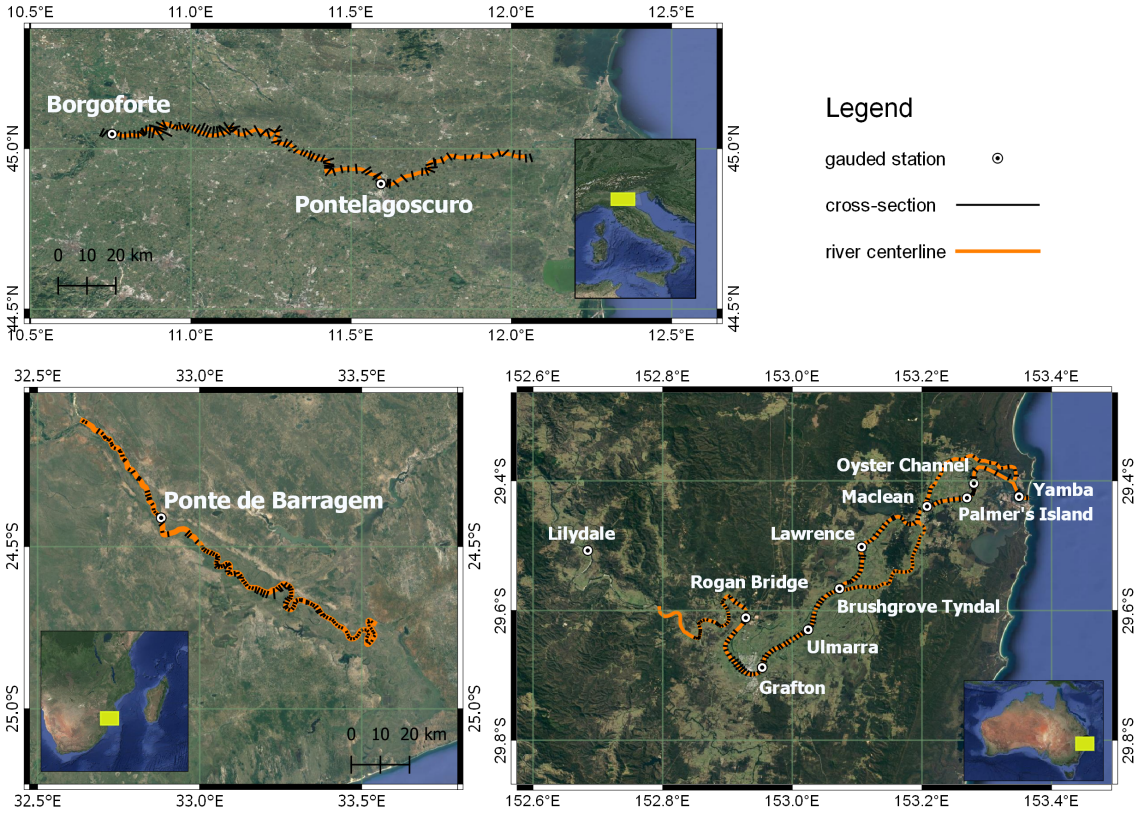

Figure 2.5: Study areas: on the top the Po River (Italy), on the bottom left the Limpopo River (Mozambique) and on the bottom right the Clarence River (New South Wales, Australia).

The Po River (upper panel Figure 2.5) is the longest Italian river with an overall basin extent of about 86859 km^2, a total length of 650 km and more than 140 tributaries. The vast floodplains, typically protected by a continuous embankment, are characterized by a reservoir capacity of about 450 Mm^3 with a width ranging from 200 m and 5 km.
In particular this study is referred to the 132 km-stretch that goes from the gauging station of Borgoforte to the beginning of the river delta. The upper panel of Figure 2.5 depicts the survey area, showing the gauging stations (i.e. Borgoforte, Pontelagoscuro) where the Po River Basin Authority (Autorità di Bacino Distrettuale del Fiume Po (AdBPo), `https://adbpo.gov.it/`) is responsible of in-situ monitoring of hydrological variables (i.e. water levels, river flow). In order to test the validity of the proposed method, a detailed knowledge of the riverbed topography is needed. The reference DEM integrates a LiDAR-2m DEM acquired in 2005 by AdBPo with topography information from multibeam sonar and traditional surveys (i.e. more than 100 river CSs provided by Agenzia Interregionale per il Fiume Po (AIPO); see Camorani et al., 2006). Moreover, a series of maximum high watermarks observed in the aftermath of a major flood event occurred along the Po river is exploited for hydraulic model validation.

The Limpopo River (left bottom panel Figure 2.5) is one of the major rivers of Mozambique. It extends from the Witwatersrand mountains in South Africa to the Indian Ocean with a length of 1700 km and a hydrographic basin of about 415000 km^2. Only after the Olifants River enters Limpopo River, its main tributary, Limpopo River becomes navigable to the sea. In its extension, the basin covers a wide range of climates including tropical rainy conditions along the coast of Mozambique, tropical dry savannah and hot dry steppe further inside in Zimbabwe, until cool arid slopes in the mountainous areas of South Africa (Reali, 2018). The selected river stretch is South-East of hydrographic basin, with a length of about 166 km. As depicted in Figure 2.5, the last 50 km near the river mouth have been not detected: the water course presents limited channel width (i.e. under 90 m) restricting the CS profile description from the satellite DEM.
Detailed terrain information (i.e. 1m-LiDAR, UAV-derived topography) proposed in previous studies (Reali, 2018; Mazzoleni et al., 2020) are not exploitable for this analysis, since they refer to only a 30 km-stretch of this survey river portion. Notwithstanding the lack of a monitoring network and of a high resolution DEM, a series of 129 CSs measured in field are exploited in phase of validation. In 2010 a detailed field bathymetric campaign was performed as a joint effort of the National Directorate of Water and Resource Management together with two local consultancy companies, Salomon LDA and Consultec LDA, by means of Total Station and RTK-GPS tools, guaranteeing a resolution of 0.5 m

and vertical accuracy of about 2 cm (Mazzoleni et al., 2020).

The Clarence River (right bottom panel Figure 2.5) is the largest river in mainland Australia South of the Tropic of Capricorn, with a total length of 394 km, drainage area of 22700 km^2 and 24 tributaries. The Clarence river has a long history of flooding, with more than high flow events recorded since 1839 (i.e. since the European settlement). Four events having larger than 10 years average recurrence interval occurred in 2001, 2009, 2011, and 2013 and almost caused the overtopping of the levee systems protecting the main urban areas, namely Grafton, Ulmarra, and Maclean (Huxley and Farr, 2013). Accurate modelling of river flow in low and high periods is also essential to support biodiversity programs (Rogers et al., 2016).
This study focuses on the 128 km (i.e. 135 km of main stem; 165 km considering also branch 1 from Brushgrove to MacLean and branch 2 from MacLean to Yamba) long river reach from Lilydale to Yamba, the river mouth. The Australian Bureau of Meteorology provides measured discharge data at Lilydale (`http://www.bom.gov.au/waterdata/`), while water level gauge stations at 11 locations (Rogans Bridge, Grafton, Ulmarra, Brushgrove, Tyndale, Maclean, Palmers Island Bridge, Lake Wooloweyah, Oyster Channel, Yamba) are maintained by the New South Wales Manly Hydraulics Laboratory (`http://new.mhl.nsw.gov.au/`). The reference DEM is derived from a 1m LiDAR having a vertical accuracy of ±30 cm and horizontal accuracy of ±80 cm (New South Wales Land and Property Management Authority, 2010; `https://elevation.fsdf.org.au/`). This dataset was resampled using the Geo Editor for Modeling (Hilton, 2017) to a 30 m resolution as this resolution allowed the optimal trade-off between model accuracy and computational time (Grimaldi et al., 2018). Bathymetric data are available from Copmanhurst to Yamba (∼100 km); morphologic and hydraulic analysis allow the assessment of a river bathymetry that is effective for the implementation of raster-based flood forecasting models in the narrow river reach from Lilydale to Copmanhurst (Grimaldi et al., 2018). The terrain data were modified to include the levee system. For this analysis 154 CSs are used (116 for the main stem, 23 and 15 for branch 1 and 2, respectively), derived from two field surveys completed in 1960s (Huxley and Farr, 2013) and November 2015 respectively (Grimaldi et al., 2018).

2.3.2 Satellite-borne DEM

SRTM is an international project of U.S. National Geospatial-Intelligence Agency (NGA) and U.S. National Aeronautics and Space Administration (NASA) obtaining a satellite DEM on a quasi-global scale from 56°S to 60°N. In the first version of SRTM,

the C-band radar signals with an interval of 1 arc-sec (30 meters) were available only for U.S.A, while the other countries were sampled in 3 arc-sec (i.e. 90 meters). Recently SRTM resolution has raised to 30 meters with global coverage. The analysis refers to SRTM version 4.1 provided by CGIAR-CSI (`http://srtm.csi.cgiar.org`). It has been decided to investigate SRTM potential because of: i) free availability for almost 80% of the globe; ii) high spatial resolution, primary factor that influences CSs description; iii) several studies have widely investigated its elevation bias. The removal of these inaccuracies is pivotal for the correct use of satellite-derived DEMs (Baugh et al., 2013). Yamazaki et al. (2017) proposed MERIT (Multi-Error-Removed Improved-Terrain), a high-accuracy global DEM by eliminating major bias components from existing DEMs using multiple satellite data sets and filtering techniques. Significant improvements were found in flat regions where river networks and hill-valley structures became clearly represented. Nevertheless, MERIT is characterised by a lower spatial resolution respect with SRTM 30 (i.e. 3 arc-sec spatial resolution, about 90 m at the equator), performing a coarser description for the most of available CSs, in particular for limited width sites. It has been demonstrated SRTM elevation bias is less evident in flat land, where the average vertical error is few meters (i.e. 2.6 m and 3.2 m, Koch et al., 2002; Falorni et al., 2005, respectively). Rodriguez et al. (2006) provides overall vertical error assessment for each continent, ranging from 4.7 m up to 9 m. C-band wave length adopted are unable of penetrating the dense canopy. For areas with considerable vegetation heights, SRTM altimetry is representative of an intermediate elevation among the real vegetation height and the bare ground, with an overall overestimation that depends on the adopted instruments, vegetation structure and other factors (i.e., Brown et al., 2009; Baugh et al., 2013). SRTM canopy heights effect is not considered in the analysis since all three study areas are characterised by sparse bush and tree cover with limited extent, bare ground or cultivated fields and lack of buildings. Nevertheless, SRTM CS profiles of Limpopo River seem to move upwards respect with in-situ data with a constant shift (i.e. 4-6 meters). This fact is also highlighted by Baade and Schmullius (2016) whose analysis were conducted in the Southern part of Kruger National Park, about 80 km west of Limpopo River. Comparing different DEM types (i.e. SRTM, TanDEM-X, ASTER), a SRTM mean positive offset of about 4.5 meters was estimated. It is in agreement with similar findings for South Africa in the SRTM C-band validation studies of Rodriguez et al. (2006), evaluating a continent global error of 5.6 meters. After these considerations, a 5-meters lowering has been applied to all SRTM data for Limpopo survey area.

Table 2.1: Hydraulic models information: flood event, boundary conditions and reference data for validation phase.

	Flood event	**Upstream condition**	**Downstream condition**	**Reference data**
Po River	January 2000	Hydrograph at Borgoforte	Normal depth (2‰) at the river delta beginning	Maximum observed CS water levels
Limpopo River	February 2000	Hydrograph at Ponte da Barragem de Macarretane	Normal depth (1.6‰) at the downstream section	Maximum simulated CS water levels by in-situ-based model
Clarence River	January 2011	Model Lidar+Bathymetry: measured discharge hydrograph at Lilydale. Models SRTM and SRTM+Ribest: discharge hydrograph predicted by the model Lidar+Bathymetry	Measured tidal levels at Yamba	Measured water level time series at 10 gauge stations. Remote sensing-derived flood event.

2.3.3 Numerical modelling

To detect how bathymetry knowledge affects hydraulic modelling, SRTM CSs modified by using RiBEST tool are exploited for the implementation of hydraulic models (i.e. 1-D model, 2-D model). In particular, the study refers to different models: i) two 1-D hydraulic models for Po and Limpopo River have been built using the HEC-RAS software; ii) a 2-D hydraulic model developed using LISFLOOD-FP for Clarence River (Bates et al., 2010). From now on, hydraulic model based on river CSs modified by RiBEST tool is called "SRTM-mod". All the model inputs and parameters are shown in Table 2.1.

1-D hydraulic model

Since its wide use for hydraulic modelling (Pappenberger et al., 2005; Mazzoleni et al., 2014), in this work the one-dimensional version of the HEC-RAS model is used, solving the Saint–Venant equations using the finite-difference method (Preissman, 1961) to discretize the continuity and momentum equations. The reference models have been built on detailed topographic information and ground data (i.e. LiDAR integrated with bathymetry measurements for Po River; in-situ information for Limpopo River; see Section 2.3.1). Also, the boundary conditions (see Table 2.1) derive from in-situ data, in order to avoid additional data uncertainties affecting hydraulic models outcomes and to highlight the effect of not detailed geometry on flood modelling. Historical flow hydrographs (reaching peaks of 11250 m^3/s for Po River and 1060 m^3/s for Limpopo River) are considered as upstream conditions, while normal depth conditions are assumed as downstream conditions (2‰and 1.6‰for Po and Limpopo River, respectively).

The model calibration is based on the identification of the Manning's roughness coefficient, n ($m^{-1/3}s$) for the main channel and floodplains. The aim is the optimal n identification maximizing the average Nash-Sutcliffe Efficiency (NSE) and minimizing the average Root Mean Square Error (RMSE), evaluated respect with the reference data (see Table 2.1). For the Po River a series of maximum observed water levels are available; on the contrary, since the lack of in-situ observation for the Limpopo River, the maximum CS water levels have been simulated adopting the reference hydraulic model.

$$NSE = 1 - \frac{\sum_{i=1}^{N} [x_{sim} - x_{ref}]^2}{\sum_{i=1}^{N} [x_{sim} - \bar{x}]^2} \tag{2.1}$$

where x_{sim} and x_{ref} are the simulated and reference (see Table 2.1) water levels respectively, $\bar{x}$ indicates the average maximum reference water level at each river CS and N the number of observations. NSE ranges between - ∞ and 1, when the simulated values fit perfectly the reference ones. Thus NSE must be maximised in the calibration phase.

$$RMSE = \sqrt{\sum_{i=1}^{N} \frac{(x_{sim} - x_{ref})^2}{N}} \tag{2.2}$$

RMSE is always non-negative, and a value of 0 (almost never achieved in practice) would indicate a perfect fit to the data. Thus RMSE must be minimized in the calibration phase.

The Limpopo River hydraulic model is implemented considering only the reach from Ponte da Barragem de Macarretene, a barrage with a capacity of 4 Mm^3 used to elevate the water level to feed the intake of an irrigation channel positioned 1 km upstream (Figure 2.6) with a length of about 88 km and with 85 CSs.

Referring to Domeneghetti (2016), the Po study area can be divided into three subreaches with different roughness coefficients: the upper stretch goes from Borgoforte to Sermide (blue stretch, Figure 2.7), the middle one is delimited by the confluence of Panaro River (yellow stretch, Figure 2.7), while the lower part ends at the beginning of river delta (orange stretch, Figure 2.7). The optimal set of Manning's coefficients obtained in the calibration phases for Po and Limpopo River are shown in Section 2.4.2.

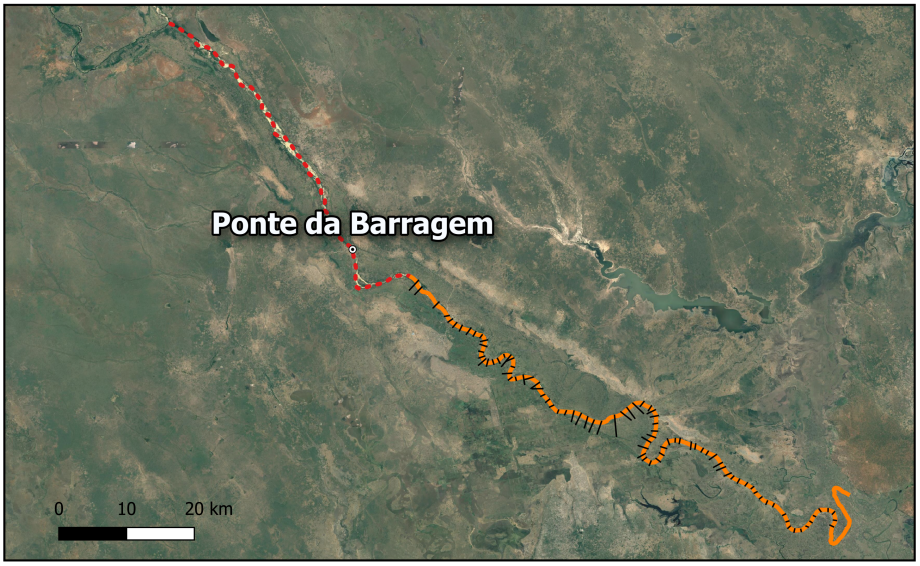

Figure 2.6: The 88-km stretch (orange line) of Limpopo River and CSs (black lines) exploited for hydraulic modelling. The red dashed line depicts the river reach not considered in this phase.

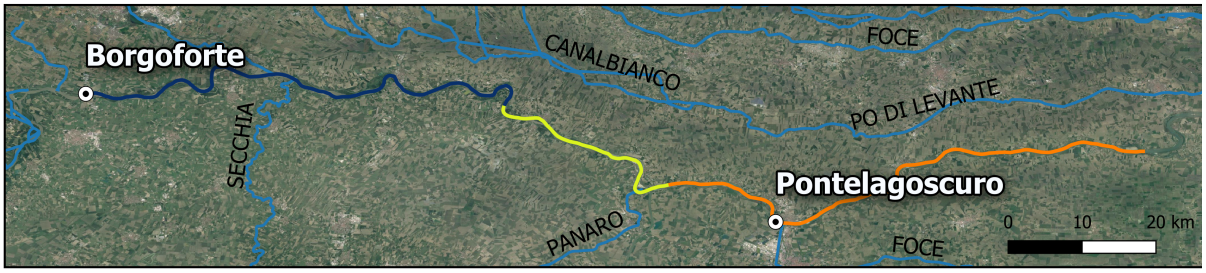

Figure 2.7: Upper (in blue), middle (in yellow) and lower (in orange) subreaches of Po River for the calibration phase (Domeneghetti, 2016).

2-D hydraulic model

The 2-D hydraulic model is based on LISFLOOD-FP (Bates et al., 2010) and it solves the inertial approximation of the shallow water equations using a finite difference method which is explicit in time and first order in space. In the model set-up used for this study, river geometry is discretised using a number of grid cells. Measured bathymetric data are used for the implementation of the reference model; more specifically, irregularly spaced CSs and additional soundings where available are converted into a submeter irregular mesh topography using a customised along-thalweg curvilinear interpolation algorithm and a second order inverse distance algorithm. The nearest neighbour method is finally used to sample this submeter irregular mesh topography to a regular 30 m grid, which is integrated with the reference DEM into one seamless data structure. Measured time series of discharge at Lilydale and water level at Yamba are used as input and downstream boundary conditions, respectively. Floodplain roughness values are evaluated using land cover data and previous analysis (Huxley and Farr, 2013); spatially distributed river roughness values are exploited as calibration parameters. More specifically, the model is calibrated using remote sensing-derived flood extent and wet/dry boundary points retrieved from the analysis of two SAR (CosmoSkyMed) images acquired during the January 2011 flood event. The calibrated Manning's roughness values range between 0.016 and 0.025 $m^{-1/3}s$; the Critical Success Index (CSI) is used to quantify the agreement between modelled and observed flood extent and the average value for the two satellite images is 0.71. Water level gauged data at 10 locations from January 10^{th} to January 17^{th} are used as independent validation dataset and the average NSE is 0.88 (the minimum value is 0.44 at Lake Wooloweyah), the average RMSE is 0.27 m (the maximum value is 0.47 m at Rogans Bridge). The calibrated model with measured bathymetry and levee system is then used as a benchmark (hereafter called "REF") to evaluate the impact of different representations of river bathymetry on the modelling of flow dynamics in both low and high flow conditions. The tested morphological datasets are the SRTM and the SRTM-mod.

The RiBEST algorithm is applied from 36 km downstream of Lilydale (4 km upstream

of Rogans Bridge) to the river mouth at Yamba (Figure 2.5); that is, the algorithm is applied to a total river length of 165 km (including both the main stem and the lateral branches). Available measured river cross sections between Copmanhurst and the river stretch beginning are on average 149 m wide (median 139, minimum 96, maximum 225), estimated river width between Lilydale and Copmanhurst is 186 m. The algorithm could not be applied to the narrow river reach between Lilydale and Copmanhurst; in fact, a data parsimonious assessment based on hydraulic analysis and information derived from Remote Sensing (RS), and a few (at least three) measurements is proposed by Grimaldi et al. (2018). The results of the application of the RiBEST algorithm to a total of 154 CSs are detailed in Section 2.4. Measured discharge data are not available downstream of Lilydale, consequently, the reference model is used to generate the discharge time series at river stretch beginning. The modelled discharge time series, the measured water level at Yamba, and the calibrated roughness parameter set are used as input, downstream boundary, and parameters for the implementation of the SRTM and SRTM-mod models. In other words, the only difference between the three model implementations is the morphological dataset, with the latter two model implementations differing only for the bathymetric data. The models are used to predict river and floodplain dynamics during a mid-flow period (from December 28th 2010 to January 6th 2011), a high flow period (from January 10th to January 17th), a low flow period (from February 4th to February 28th 2011). It is here underlined that the high flow period is defined to focus on a flood event, the low flow period started only after the exhaustion of the decreasing limb for all the models. Specific purpose of this study is not the assessment of the absolute accuracy of three model set-ups but rather the quantitative analysis of the impacts of different representations of river geometry. For this reason, it is decided not to repeat the calibration for the SRTM and SRTM-mod models; moreover, it is here underlined that the reference model is calibrated to achieve an accurate representation of floodplain inundation extent during a high flow period, while low flow periods were not considered for model calibration.

2.4 Results and discussion

2.4.1 Geometric SRTM cross-sections modification by RiBEST

Table 2.2 summarises RiBEST results and performances for the river bathymetry evaluation. In particular, it reports the results relative to the use of the IM (Interactive Method) approach for channel selection and CSs locations were identified by means of shape files referring to previous field surveys. The number of optimal CSs is expressed in

percentage on the total amount of CSs for each reach.

Table 2.2: Results of RiBEST application for river bathymetry estimation: optimal CSs ratio [%], average lowering [m], Mean Error (ME) and Root Mean Square Error (RMSE) before (SRTM) and after (SRTM-mod) RiBEST application.

	Optimal CSs [%]	**Average lowering [m]**	**ME SRTM mod [m]**	**ME SRTM [m]**	**RMSE SRTM mod [m]**	**RMSE SRTM [m]**
Po	70	7.4	0.1	7.4	2.6	7.9
Limpopo	33	5.3	0.4	5.8	1.4	5.9
Clarence	48	7.7	4.6	12.3	4.6	13.0

In order to grasp the complexity of Clarence study area for a realistic 2-D hydraulic model implementation, the two minor branches (branch 1: from Brushgrove to Maclean; branch 2: from Maclean to the delta, Figure 2.5) are also considered for the bathymetry estimation. RiBEST suggests an average lowering of 5.1 and 6.1 meters for branch 1 and branch 2, respectively.

The value and accuracy of the estimation process is assessed based on different error metrics, calculated before and after RiBEST application:

- Mean Error (ME):

$$ME = h_{min} - h_{ref} \tag{2.3}$$

- Root Mean Square Error (RMSE):

$$RMSE = \sqrt{(h_{min} - h_{ref})^2} \tag{2.4}$$

where h_{min} represents SRTM river bottom and h_{ref} the minimum reference channel elevation. For all the study cases, RiBEST tool provides significant improvement in terms of bathymetry estimation, showing lower ME and RMSE values, in particular for Po and Limpopo Rivers (Table 2.2). The high values of ME and RMSE for Clarence River (i.e. 4.6 and 4.6 meters respectively) are probably consequence of the presence of several irregularities at the bottom of the reference CSs (i.e. very deep small grooves), which occasionally provide consistent h_{ref} discontinuities. The bathymetry evaluation analysis simply investigates the punctual overlap between SRTM-mod and the reference river bottom, providing a first idea of main channel representation. A more complete evaluation of river morphology should take into consideration also CS shape, perhaps estimating other

hydraulic parameters, such as flow area and hydraulic radius. RiBEST performs such estimations assuming a rectangular shape for the modified CSs: this choice relies on the fact that assuming a rectangular shape provides better performance than the triangular one, since it appears to be more representative of real sections dimension in case of wide rivers. Table 2.3 shows the hydraulic parameters estimated (i.e. flow area (A), hydraulic radius (R)) considering SRTM-mod CSs. Reference values are obtained averaging hydraulic parameter values for reference CSs on the overall river stretch. RMSE is reported as ratio between the average parameter value using SRTM-mod Css and the reference value (first column, Table 2.3).

Scatter plot of Figure 2.8 and graphs of 2.9 highlight a good correlation among estimated and observed hydraulic parameters. In particular, the coefficient of determination R^2 is equal to 0.70, 0.77 and 0.99 for R and 0.72, 0.83 and 0.96 for A for Po, Limpopo and Clarence Rivers, respectively. In general estimated hydraulic parameters are representative of the real ones, especially for the Clarence River. An overestimation of both parameters is evident for Limpopo River.

Table 2.3: RiBEST outcomes for hydraulic parameters assessment: reference parameter, coefficient of determination (R^2) and Root Mean Square Error (RMSE) for flow area (A) and hydraulic radius (R), respectively.

	Reference A **[m²]**	**R²** A [/]	**RMSE** A [/]	**Reference** R **[m]**	**R²** R [/]	**RMSE** R [/]
Po	9675	0.72	0.71	9.0	0.70	0.26
Limpopo	3509	0.83	1.13	6.75	0.77	0.33
Clarence	26852	0.96	0.25	18.13	0.99	0.17

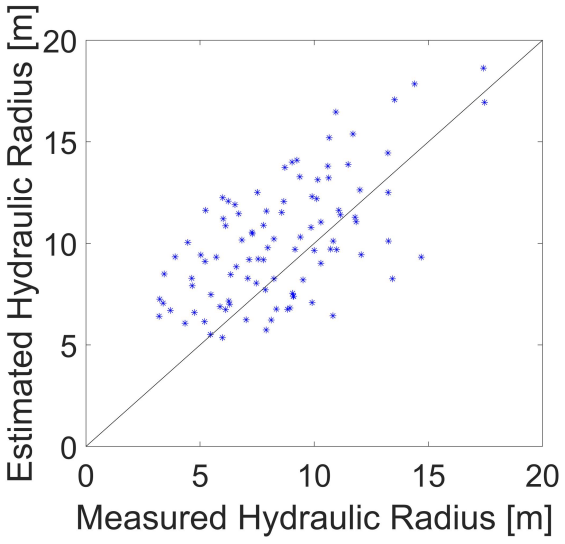

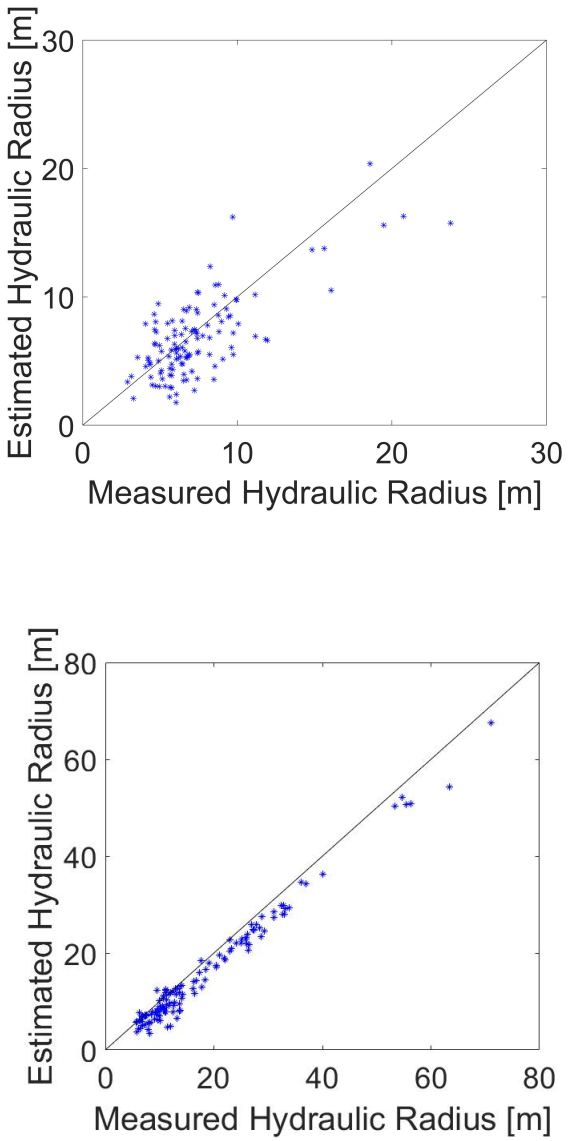

Figure 2.8: Hydraulic radius (R) estimated from SRTM-mod respect with the reference one for Po, Limpopo and Clarence River respectively.

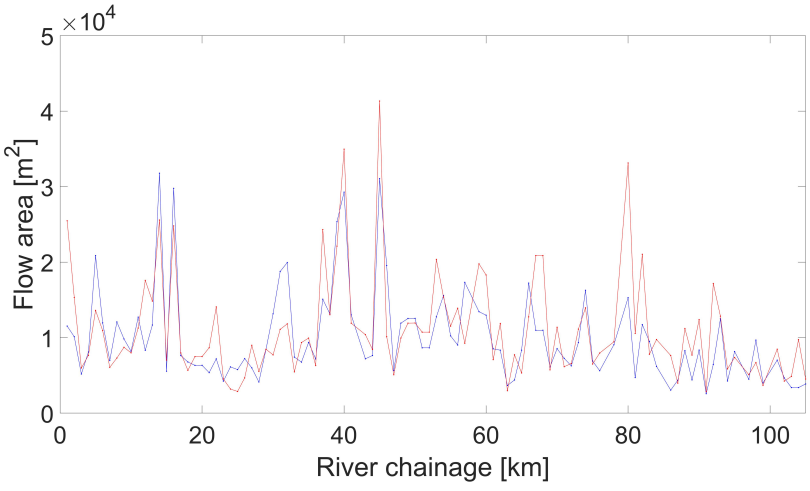

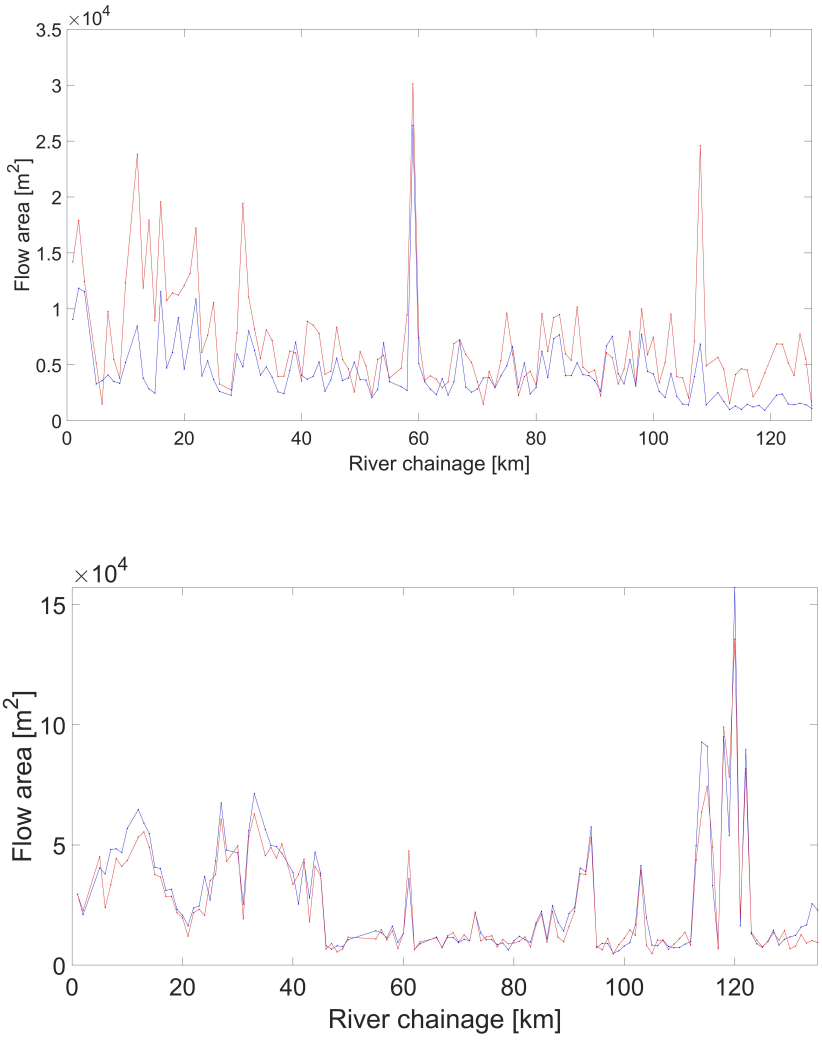

Figure 2.9: Flow area (A) estimated with SRTM-mod (red line) and surveyed (blue line) CSs along Po, Limpopo and Clarence Rivers, respectively.

2.4.2 Impact of river bathymetric information on hydraulic modelling

1-D hydraulic model

The best Manning's coefficient sets obtained from the calibration phases carried out for Po and Limpopo River are shown in Table 2.4. The reference roughness values are calibrated with 1-D reference hydraulic models (see Table 2.1), represented in brackets. It should be noticed that Po River is discretized into three portions (Figure 2.7), thus calibration results are shown as combination of Manning's coefficients for the river channel.

Limpopo River calibration required channel roughness coefficients higher than reference ones along the overall reach (i.e. NSE and RMSE equal to 0.96 and 0.97 respectively), while calibrated Manning's coefficients are in good accordance with reference ones for the Po River (i.e. NSE and RMSE equal to 0.99 and 0.39, respectively).

Table 2.4: 1-D hydraulic models calibration results: Manning's coefficients for channel and floodplains (reference values in brackets), Nash-Sutcliffe efficiency value (NSE), Root Mean Square Error (RMSE).

	Manning's [$m^{-1/3}s$]		**NSE [/]**	**RMSE [m]**
	channel	floodplains		
Po	0.040-0.038-0.027	0.08	0.99	0.39
	(0.044-0.042-0.025)	(0.10)		
Limpopo	0.050	0.07	0.96	0.97
	(0.030)	(0.07)		

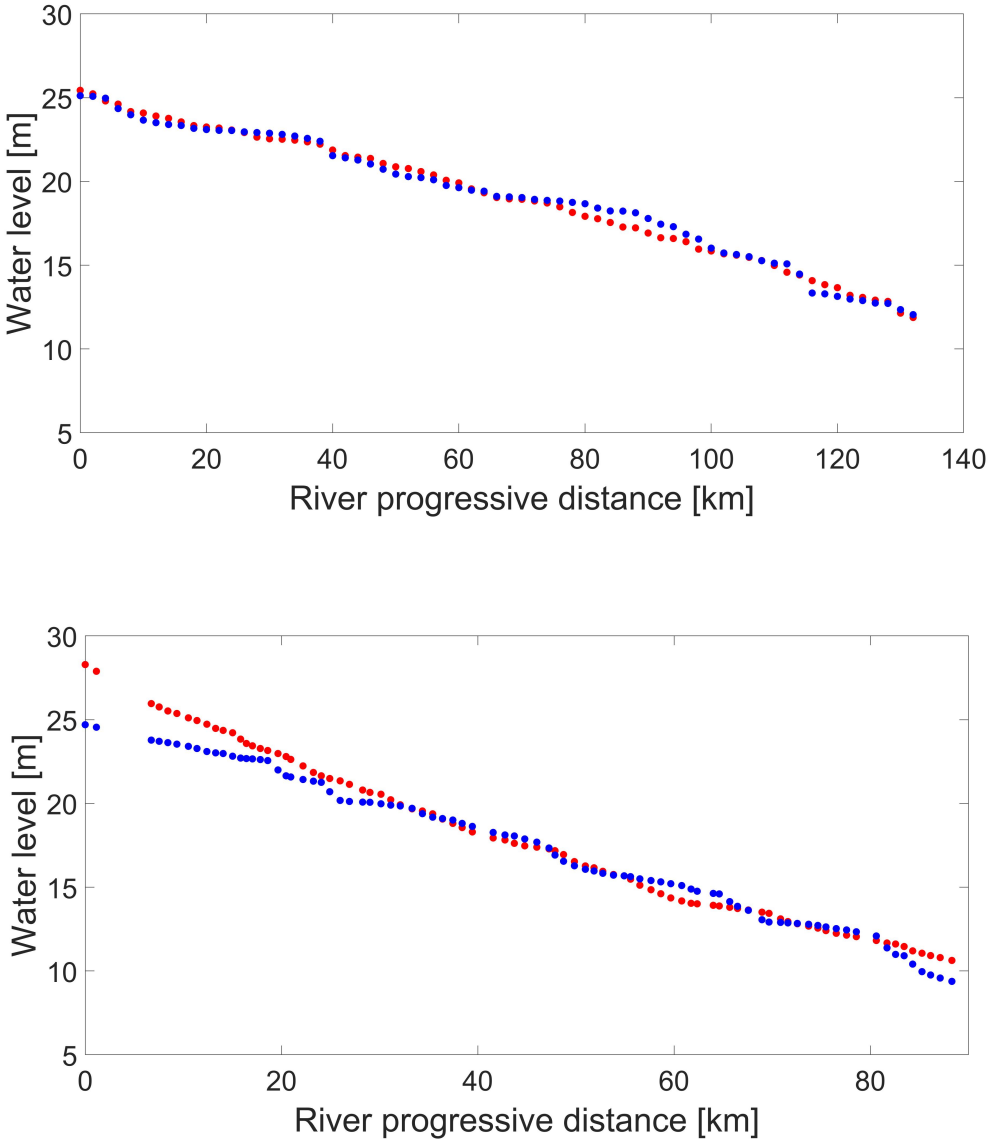

Figure 2.10: Comparison among maximum simulated CS water levels (blue points) using the best Manning's coefficients combination of the calibration phase (see Table 2.4) and the reference ones (red points) for Po River (upper panel) and Limpopo River (bottom panel).

Figure 2.10 compares maximum simulated and reference water levels at each CS for Po (upper panel) and Limpopo River (bottom panel). Nearly a perfect overlapping among simulated and reference levels is evident for Po River. The same occurs along most part of the Limpopo River, although water levels are underestimated in the upper and lower portions of the river. SRTM appears unable to properly describe CS geometry in these transects characterized by limited widths (i.e. about 130 meters), thus overestimating the flow area and obtaining minor water levels (Figure 2.10).
To test SRTM-mod hydraulic models reliability, Manning's coefficients calibrated with reference models (i.e. 0.044, 0.042, 0.025 for Po River; 0.03 for Limpopo River, see Table 2.4) are exploited for SRTM (thus based only SRTM river CS without RiBEST application) and SRTM-mod models simulations. SRTM-mod models for both study cases provide quite good results (i.e. NSE equal to 0.97 and 0.84; RMSE equal to 0.69 and 1.93 for Po and Limpopo Rivers, respectively), while SRTM models are unsuitable to represent rivers dynamics (i.e. NSE equal to -0.98 and 0.41; RMSE equal to 5.28 and 3.70 for Po and Limpopo Rivers, respectively).

2-D hydraulic model

The three morphological set-ups, namely, REF (reference model), SRTM and SRTM-mod are used to investigate the impacts of different representations of river bathymetry on the modelling of both low flow and high flow periods for Clarence River study case. As explained in Section 2.3.3, the calibrated roughness values of the reference model are exploited for the implementation of the models based on SRTM and SRTM-mod data. Figure 2.11a-d shows the modelled and observed water level adopting all configurations at Rogans Bridge, Grafton, Brushgrove and Maclean, respectively. Each gauge station is selected to represent the models behaviour in the upstream, narrow river reach (Figure 2.11a), a river reach with complex river path (Figure 2.11b); in the mid-river reach, including 4 gauge stations (Figure 2.11c); the most downstream river reach, up to the river mouth, including 3 gauge stations (Figure 2.11d).
The NSE and RMSE are used to quantify the discrepancy between modelled and measured data during a mid-flow period (from December 28^{th} 2010 to January 6^{th} 2011), a flood event (from January 10^{th} to January 17^{th}), and during a low flow period (from February 4^{th} to February 28^{th}). The ratio between modelled and observed water level flood peak is exploited to complement the previous analysis as in channelised rivers, small inaccuracies in the prediction of water level can lead to large inaccuracies in the prediction of floodplain inundation extent. Table 2.5 shows the values of the performance metrics for each flow period and for different river traits. In the SRTM model, the inaccurate representation of

river flow capacity led to large discrepancies between modelled and measured water levels with negative NSE values for all the time series, with RMSE larger than 3 meters during the flood event.

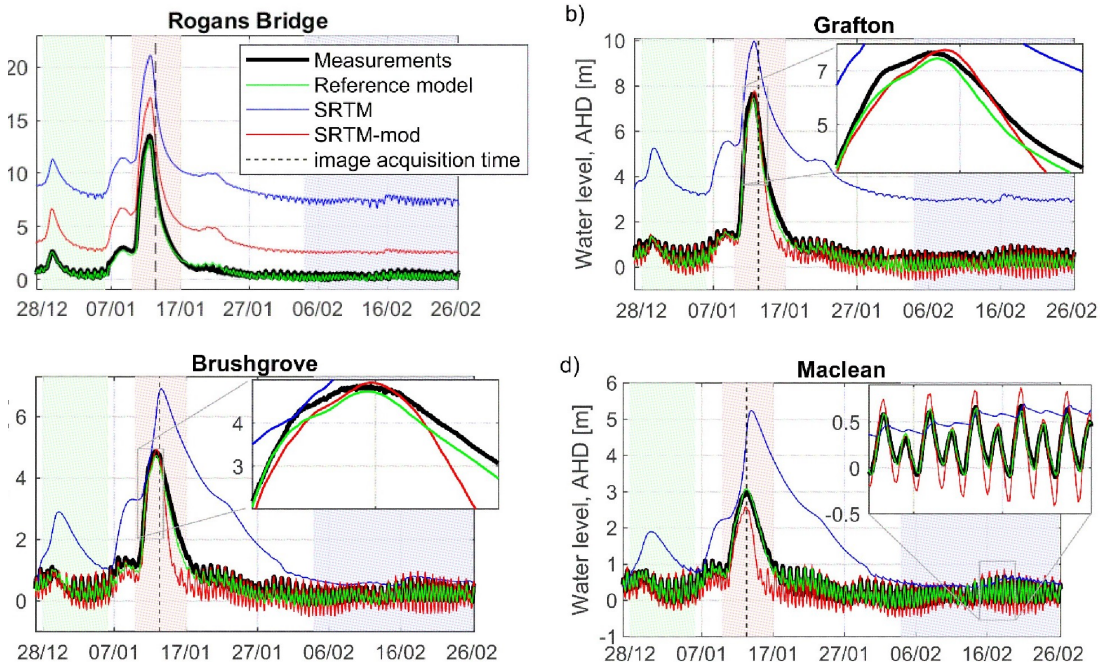

Figure 2.11: Modelled and measured time series of water level at four gauge stations: Rogans Bridge (a), Grafton (b), Brushgrove (c), Maclean (d); in each figure, the shaded areas indicate the mid-flow period (green), the high-flow period (red), the low-flow period (blue).

Nevertheless, the impacts on the modelled flow dynamics are a function of valley morphology. In the upstream, narrow valley, the large overestimation of the thalweg elevation (Table 2.2) leads to a sensible, yet almost constant positive bias of approximately 8 m between modelled and measured water levels during both low and high flows, with negligible impacts on flood wave routing (Figure 2.11a). In the downstream, nearly flat, area, the reduced river capacity of the SRTM dampens the tidal oscillations in low flow periods and leads to large impacts on flood waves routing with large overestimations of water levels even for mid-flow periods, sensible delays of the flood peak, and increases (up to 20 days) duration of the decreasing limb. The results of the model SRTM highlights the benefits of using RiBEST when field data are not available.

In the narrow upstream area RiBEST sensibly reduces the SRTM overestimation of the thalweg, nevertheless modelled water levels are affected by a positive bias of 3 m for any flow period (Figure 2.11a). In the downstream, flat area, the application of RiBEST allows an accurate representation of river flow capacity leading to positive NSE values and RMSE values reduced when compared to model SRTM. In fact, SRTM-mod results

in RMSE values having the same order of magnitude as the reference model for all the gauge stations and for all the flow conditions.

In the low-flow period, water levels are strongly affected by the downstream tidal levels and the accuracy of both the SRTM-mod and of the reference model increased from upstream to downstream. Model SRTM-mod underestimates the damping of the tidal oscillations and results in larger RMSE and lower NSE values than the reference model. Specifically, RMSE values of the SRTM-mod and reference models are 0.34 m and 0.18 m at Grafton and 0.11 m and 0.07 m at Maclean, respectively. These discrepancies are negligible for most of the pragmatic applications, nevertheless, these results offer an insight on the relevance of river shape for accurate flow modelling. The reduced damping effect of the SRTM-mod can be explained by the decreased morphological complexity of rectangular CSs: the highly irregular, asymmetric real river bathymetry acts as macro-roughness and reduces the tidal oscillations. The impacts of a simplified river shape increases in the direction of the flow and the SRTM-mod results in negative NSE values in the upstream gauge stations.

In the high-flow period, river water levels are driven by the input flow hydrograph and by the interactions with the floodplain areas; consequently, discrepancies increased from upstream to downstream with the SRTM-mod and the reference model resulting in RMSE values of 0.85 m and 0.41 m at Grafton, and 0.75 m and 0.09 m at Maclean, respectively. SRTM-mod adequately reproduces the measurements during the rising limb with values of flood peak ratio within the range 92.50 % (Lawrence) and 104.27 % (Tyndale) in the mid-trait of the river reach; a slight underestimation with an average flood peak ratio of 88% is observed in the most downstream area. However, the decreasing limb is underestimated, discrepancies between SRTM-mod and measurements are larger from upstream to downstream and NSE values decrease from Grafton (0.85), to Lawrence (0.43), to Maclean (-0.02), to Oyster Channel (-0.92).

A similar effect is not observed in the reference model and the understanding of these results required the analysis of the modelled floodplain inundation extents. Figure 2.12e-g shows the comparison between simulated and observed flood extent for REF, SRTM, and SRTM-mod models, respectively; the acquisition time of the observed (remote sensing, RS) flood extent is shown in Figure 2.11a-d. As explained in Section 2.3.3, the reference model is calibrated using this image. Moreover, the Grafton levee system with crest elevation 8.25 m (Huxley and Farr, 2013) is accurately represented by the terrain data used for the implementation of the reference model; conversely, the SRTM DEM is not edited in the floodplain. The model SRTM has a peak value at Grafton of 10 m (Peak Ratio 130%) leading to large overestimation of the inundation extent in the urban area.

Overestimation of flood peak ratio between Ulmarra and Brushgrove (Peak Ratio 142%) similarly leads to overestimation of the RS-derived flood extent in the large floodplain. This large overestimation of the inundation extent affects the flood wave propagation downstream leading to a large delay of the flood peak in gauge stations in the downstream area (Figure 2.11d). The SRTM-mod slightly overestimates the peak value at Grafton (Peak Ratio 101.5%), this small discrepancy and the lack of adequate representation of the levee system leads to the overestimation of the flood extent at Grafton. Albeit having a good accuracy at the point scale (Table 2.5), the SRTM-mod underestimates the observed flood extent in the large floodplain between Ulmarra and Brushgrove. An in-depth analysis of the floodplain inundation dynamics allows to explain these discrepancies.

In the upstream area of the catchment (up to Brushgrove), the SRTM model fills the valley and large changes in water level leads to negligible changes of inundation extent (Figure 2.12e,f), meaning that a simple comparison between modelled and inundation flood extent (after the flood peak) partially hinders the detrimental impact of the lack of representation of river bathymetry on the prediction of flood risk. Figure 2.12h shows the flood extent predicted by SRTM-mod 28 hours after the RS acquisition time and demonstrates that, despite the sensible discrepancy between the modelled and observed flood extent at the acquisition time of the RS image, the SRTM-mod could almost reproduce the full flood extent. This result is explained by inaccuracies in the representation of the connectivity between the river and the floodplain in the SRTM-mod with the modelled flood wave propagating southwards from Brushgrove rather than eastwards from Grafton. The Clarence catchment is a morphologically complex area, with multiple small creeks receiving water from the Clarence river during major flood events (Huxley and Farr, 2013) and a lack of accuracy of the SRTM is expected. The inaccuracies in the representation of the connectivity between the river and the floodplain leads to larger water volumes persisting in the floodplain at the end of the flood event in the SRTM-mod than in the reference model. These results explain the underestimation of the decreasing limb of the measured water level time series (Figure 2.11a,b,c,d).
Figure 2.12i then compares the discharge values computed at Maclean by the reference model, the SRTM, and the SRTM-mod, respectively (measured values are not available). In the model SRTM, the overestimation of the inundation extent and volume in the upstream area leads to a sensible decrease and delay of the modelled flood peak at Maclean when compared to the reference model. Conversely, the SRTM-mod results in larger discharge values at an earlier time than the reference model. RiBEST could adequately reproduce the flow capacity of the Clarence River, nevertheless, at Maclean, water levels are lower than the measurements (and of the reference model, Figure 2.11d), and dis-

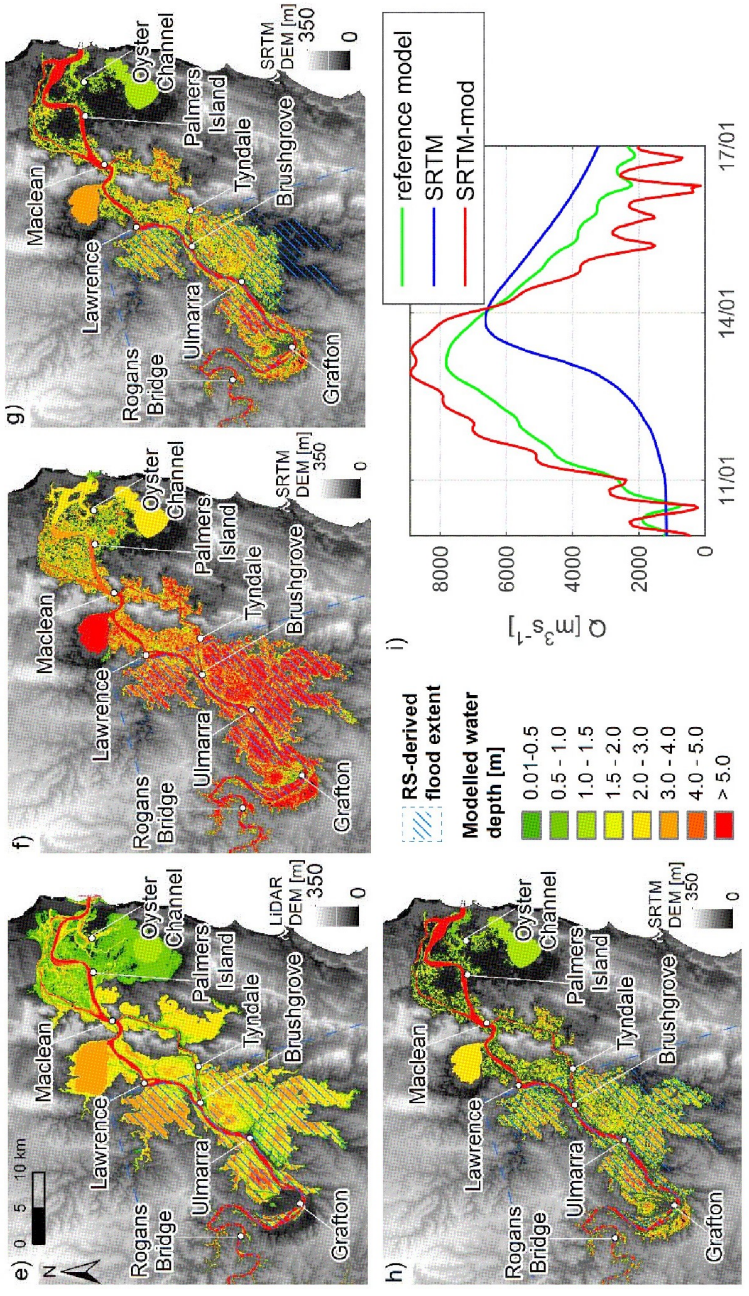

Figure 2.12: Modelled and observed inundation extents at the time of the remote sensing (SAR) overpass for the three model set-ups: reference model (e), SRTM (f), SRTM-mod (g). Inundation extent predicted by the model SRTM-mod 28 hours after the remote sensing overpass (h). Modelled discharge time series at Maclean (i).

charge values are larger than the reference model (Figure 2.12i). Consequently, it is here hypothesized that, in the SRTM-mod, the use of rectangular CSs leads to a lower macro-roughness than in the reference model. These results highlighted (i) the importance of using spatially distributed data to adequately evaluate model performances (REF), (ii) the need for a global database of flood defences, and (iii) the impact of the representation of river shape on the modelling of flow dynamics. Moreover, when using RiBEST and SRTM to implement 2-D models, care must be taken to achieve an accurate representation of flow connectivity between the main river stem and the floodplain.

Table 2.5: Summary of the more relevant indexes (NSE, RMSE, Peak Ratio) relative to three zones (Grafton, river reach from Ulmarra to Brushgrove - Middle Reach, river reach from Maclean to Yamba - Lower Reach) and several flow conditions.

		Grafton			**Middle reach**			**Lower reach**		
		REF	SRTM	SRTM-mod	REF	SRTM	SRTM-mod	REF	SRTM	SRTM-mod
NSE [-]	28/12 - 06/01	0.79	-109.8	0.21	0.94	-30.52	0.48	0.92	-9.80	0.76
	10/01 - 17/01	0.96	-1.36	0.84	0.94	-2.88	0.50	0.90	-17.68	-0.31
	04/02 - 28/02	0.45	-143.9	-1.40	0.82	-8.51	-0.55	0.89	-1.08	0.69
RMSE [m]	28/12 - 06/01	0.14	3.28	0.28	0.06	1.48	0.19	0.06	0.72	0.11
	10/01 - 17/01	0.41	3.25	0.85	0.31	2.44	0.87	0.10	1.69	0.54
	04/02 - 28/02	0.18	2.64	0.34	0.08	0.54	0.22	0.07	0.29	0.11
Peak Ratio [%]	10/01 - 17/01	97.3	130.1	101.53	94.63	142.02	99.57	104.70	203.70	87.94

2.5 Concluding remarks

This study proposes an innovative method to exploit satellite information (i.e. satellite DEM) for river bathymetry assessment. In particular, the Slope-Break (SB) method is exclusively based on topographic information (i.e. river channel width and elevation). Starting from the analysis presented in Domeneghetti (2016), the study aim is to verify SB reliability on several contexts: Po River (Italy), an example of heavily human impacted river, Limpopo River (Mozambique) located in a remote areas and Clarence River (New South Wales, Australia) featured by the presence of vast floodplains. Moreover, to seek the benefits induced by river bathymetry knowledge derived from SB on hydraulic modelling, i) two 1-D hydraulic models for Po and Limpopo River and ii) a 2-D hydraulic model for Clarence River are implemented.

A Matlab-tool (RiBEST, see Section 2.2) is developed for an automatic evaluation of river bathymetry exploiting only a DEM (i.e. SRTM) and river channel shapefile. SRTM has been selected in particular for its high spatial resolution (i.e. 30 m) suitable for a quite realistic representation of CSs profile. Moreover, it is freely-available, having a global coverage and several studies have widely investigated its potentials and limitations.

In general, the application of RiBEST tool provides evident improvements to original SRTM information, allowing a better description of CSs shape (see Table 2.2). Also hydraulic parameters (i.e. flow area (A), hydraulic radius (R)) are taken into consideration. In general, estimated hydraulic parameters are representative of the real ones (i.e. R^2 equal to 0.70, 0.77, 0.99 for R and 0.72, 0.83, 0.96 for A for Po, Limpopo and Clarence River, respectively), in particular for Clarence River (Figures 2.8, 2.9).

Regarding the hydraulic modelling, for 1-D models Manning's coefficients for channel and floodplains are calibrated. Simulated and measured water levels are in agreement for both study cases, in particular for Po River (i.e. NSE equal to 0.99 and 0.96, RMSE of 0.39 and 0.97 for Po and Limpopo respectively). The 2-D hydraulic model for Clarence River is tested to predict river and floodplain dynamics considering different flow conditions (i.e. mid-flow period, high flow period, low flow period). SRTM model seems to be unable to represent realistic water levels, showing an high discrepancy with the reference ones in all the gauged sections and for all the different flow conditions (i.e. negative NSE, RMSE also higher that 3 m). On the contrary, SRTM-mod allows an accurate representation of water levels, in particular for middle-low river portion. In the low-flow condition, SRTM-mod underestimates the damping of the tidal oscillations, fact due to the lack of morphological complexity in the use of rectangular CS profile. Regarding the floodplains inundation extent, SRTM model presents an overestimation extent in the urban area of

Grafton, while SRTM-mod in general underestimates the flooded areas near Ulmarra and the river mouth (Figure 2.12e-g). In general, SRTM model provides too high water levels in all the survey area, while SRTM-mod ensures a higher agreement with the reference model. The discrepancies among reference and SRTM-mod models are probably due to the inaccuracies in the representation of complexity and connectivity of the study area by means SRTM and to the semplifications introduced in modifying CSs geometry (i.e. rectangular profile).

This research shows how river bathymetric information are pivotal for a realistic reproduction of water course behaviour by means of hydraulic modelling. The proposed geometric approach (i.e. Slope-Break) is suitable for single-channel and unbraided wide rivers, restricting in part the application field. To facilitate the application of the Slope-Break approach the RiBEST tool has been conceived to be adaptable to several topographic products (i.e. DEMs) and requiring few inputs (i.e. river centerline).

CHAPTER 3

River data assimilation using a full Saint-Venant hydraulic model

Never make assumptions,
always look for evidence.

Leroy Gethro Gibbs, *NCIS*

This Chapter contains:

3.1 Data Assimilation method for river discharge assessment

"*The problem we intend to solve is the estimation of the state of a system, at any arbitrary past, present and future time. We possess two complementary, but both incomplete and inaccurate, sources of information: the observations and the model. Data assimilation provides the conceptual and methodological tools to tackle the problem by extracting synergies between model and observations and by exploiting their respective informational content*" (Carrassi et al., 2018).

This statement briefly highlights the two main elements at the base of DA: the numerical model for the description of the state of a system, and the observations to whom the estimated state has to strive. As introduced in Section 1.3, the main aim of DA methods is the prediction of the state of a system, intended as combination of several variables. In this case, the goal consists in the forecast of river dynamics, in particular of discharge and roughness coefficient. DA methods work on a predicted state, such as an hydraulic model output, making it closer as possible to the available observations (i.e., SWOT) by means an optimization process. Thus, the present Chapter is built as follows: Section 3.1 recalls the theoretic concepts underling the analysis, presenting the hydraulic model exploited in this work (Section 3.1.1), focusing on the numerical and observation models (Section 3.1.2) and the optimization process (Section 3.1.3). Secondly, the available satellite observations and the survey area are described in details (Section 3.2). The Section 3.3 illustrates the experimental design, thus clarifying the used DA method, all the variables involved and the validation procedure. Finally, Section 3.4 presents work outcomes.
This research was developed in collaboration with the research group at IRSTEA of Montpellier, France, under the supervision of Hind Oubanas and Pierre-Olivier Malaterre.

3.1.1 Hydraulic model SIC^2

The hydraulic model exploited in this work is the SIC^2, a 1.5D model based on the full Saint-Venant equations and developed by IRSTEA for about 30 years, succeeding the former CEMAGREF hydraulic model (Talweg-Fluvia-Sirene) (`http://sic.g-eau.net/`).
Figure 3.1 depicts a conceptual representation of SIC^2 model. The river is represented by segments (or reaches) connected each other by means of nodes (N). The boundary conditions are specified at upstream and downstream nodes. The description of river

channel is done by means a series of cross sections along the river channel centerline: for each of them, the hydraulic variables of interest (i.e., flow area (A), top width (L), wetted perimeter (P)) are estimated at a given water level, z. These variables depend also from a series of parameters (defined p_g) describing the cross section geometry, such as bed elevation (Z_b), bottom width (l), bank slope (b). SIC^2 can handle also irregular cross sections (Oubanas et al., 2018a,b).

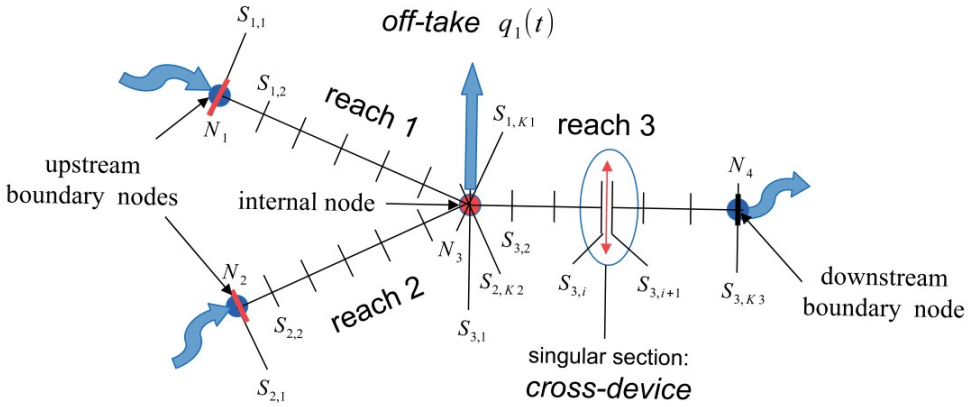

Figure 3.1: Conceptual scheme of SIC^2 model. (Gejadze et al., 2017).

The Saint-Venant Equations 3.1 and 3.2 describe the flow dynamics:

$$\frac{\partial A}{\partial t} + \frac{\partial Q}{\partial x} = Q_{\mathrm{L}} \tag{3.1}$$

$$\frac{\partial q}{\partial t} + \frac{\partial q^2/A}{\partial x} + gA\frac{\partial z}{\partial x} = -gAS_f + C_L Q_L v \tag{3.2}$$

where:

q(x,t): local discharge

z(x,t): water surface elevation (WSE)

Q_L: lateral discharge

C_L: lateral discharge coefficient varying in [0,1]

v(x,t): mean velocity ($\frac{q}{A}$)

S_f: friction slope, function of K_s(x), the Stricker coefficient, defined as:

$$S_f = \frac{q^2}{K_s^2 A^2 R^{4/3}} \tag{3.3}$$

The initial (z_0, q_0) and the boundary conditions (i.e., the inflow discharge Q(t) at the upstream node and a rating curve, defined by the rating curve parameters p_{rc}, at the downstream node) are needed to solve the equations 3.1, 3.2, 3.3. The problem 3.1 - 3.3 is discretized by means the Preissmann scheme (Cunge et al., 1980) while the fixed-point

iterations are used to resolve nonlinearity (see Malaterre et al., 2014).
Some inputs (i.e., cross-sectional geometrical parameters, roughness coefficients, boundary conditions) are needed to the exploitation of SIC^2 model for a chosen study case. For ungauged basins, these information could be hard to collect. For this reason, the research community is looking at space-born observations (i.e., satellite altimetry, river width or observation from the upcoming mission SWOT; see Durand et al., 2008; Honnorat et al., 2009; Oubanas et al., 2018b; Li et al., 2020) to generate needed initial input (i.e. WSE, width and slope). Thus, SIC^2 model can simulate water levels and local discharge and in the following step the resolution of corresponding inverse problem provides variables of interest (i.e. discharge).

3.1.2 State estimation: formulation of the problem

The two elements at the base of the estimation problem are the dynamic model and the observation model.

The dynamic model - In order to describe a system varying in time, a numerical model ($M : A \rightarrow B$) can be exploited. It maps the model inputs $U \in A$, from the inputs space U to the state space B:

$$M(U) = X \tag{3.4}$$

X represents the model state that is defined *controllable* if there exist a "control vector" V defined over a finite interval in space and time which minimizes a chosen performance index (Oubanas, 2018). Thus V collects all the unknown model parameters to be assessed via DA approaches that strongly affect the model response.
The remaining model inputs components $U^0 = U \setminus V$ are usually fixed at their best available guess ${U^0}_\mathrm{b} = U_\mathrm{b} \setminus V_\mathrm{b}$, where the subscript "b" means "background" values of U, U^0 and V respectively. The background information is used to initialize the control variables and it can derive from a previous forecast, if available.
The background U_b embodies uncertainties ξ_b that arise from various sources and are defined as:

$$U_b = U^t + \xi_b \tag{3.5}$$

where $\mathrm{U^t}$ is the true model input vector.
The numerical model M can be affected by errors in its representation of the reality. The model equations do not describe the system behaviour exactly; moreover, several errors are provided from the lack of resolution in the discretization phase as well as from inac-

curacies in parametrization. These limitations are not considered in this analysis.

The observation model - Noisy observations of the model state X, collected from i.e. in-situ measurements, space-born sensors, are available at several times. These information form the observation vector Y. The relationship among the model state X and observations (Y) is expressed by means of an observation operator, mapping X from the state space B to the observations space C, as follow:

$$Y = H(X) \in C \tag{3.6}$$

H often involves linear interpolations, convolutions or spectral-to-physical space transformation in spectral models, varying its complexity (Carrassi et al., 2018).

For practical considerations, let us introduce the inputs-to-observations nonlinear mapping $G : A \to C$, defined as follow (Oubanas, 2018):

$$H(X) = H(M(U)) \coloneqq G(U) = Y \tag{3.7}$$

Observation Y^* is also affected by errors ξ_0. Similarly to model error ξ_b, ξ_0 is also represented as an additive term that summarizes instrumental and representativeness errors (Lorenc, 1986). It can be expressed as follows:

$$Y^* = G(U^t) + \xi_0 \tag{3.8}$$

3.1.3 Variational approach

Variational DA method aims at estimating the model that best approximates all the observations within an observation window $[t_0, t_\mathrm{K}]$ simultaneously. Thus, the state estimate at a given time t_k depends on all observations available within the time window. Under the hypothesis of Bayesian estimation (see Asch et al., 2016, for more details), in variational DA the estimation problem is a type of minimization problem for a functional J, called "cost function" with the following quadratic form:

$$J(V) = \frac{1}{2}||R^{-1/2}(G(V, U_b) - Y^*)||^2 + \frac{1}{2}||B^{-\frac{1}{2}}(V - V_b)||^2 \tag{3.9}$$

where R and B are the covariance matrices corresponding to ξ_b and ξ_0, respectively. The first addend of the cost function J, the residual term, aims at minimizing the distance between the control vector V and the observations Y in the observation space (G). The second contribution is given by the regularization term, in order to minimize the distance among V and the background vector V_b in the model space.

The minimization problem applied to the cost function (eq. 3.9) is solved by looking for the point of zero-gradient $\Delta_V J(V)$, whose form is given by:

$$\Delta_V J(V) = (G'(V))^* R^{-1}(G(V, U_b^0) - Y) + B^{-1}(V - V_b) = 0 \tag{3.10}$$

where $(G'(V))$ and $(G'(V))^*$ are respectively the tangent linear and adjoint counterparts of the nonlinear operator $(G(V, U_b{}^0))$.

Three-dimensional variational data assimilation (3D-Var)

In the 3D-Var (Figure 3.2) the corrections are computed and utilized at each observation (blue diamonds) times t_k sequentially: the analysis (red squares) at t_k becomes the initial condition for the forecast (green line) at the next observation time, t_{k+1}, and so on (Carrassi et al., 2018; Oubanas, 2018).
In this case, the inputs-to-observations mapping operator G coincides with the observation operator H. Thus the cost function J and its gradient $\Delta_V J(V)$ are expressed as follows:

$$J(V) = \frac{1}{2}||R^{-1/2}(H(V, U_b) - Y^*)||^2 + \frac{1}{2}||B^{-\frac{1}{2}}(V - V_b)||^2 \tag{3.11}$$

$$\Delta_V J(V) = (H'(V))^* R^{-1}(H(V, U_b^0) - Y) + B^{-1}(V - V_b) = 0 \tag{3.12}$$

The main limit of 3D-Var approach is the assumption that all the observations within an observation window are valid only at the estimation time t_k.

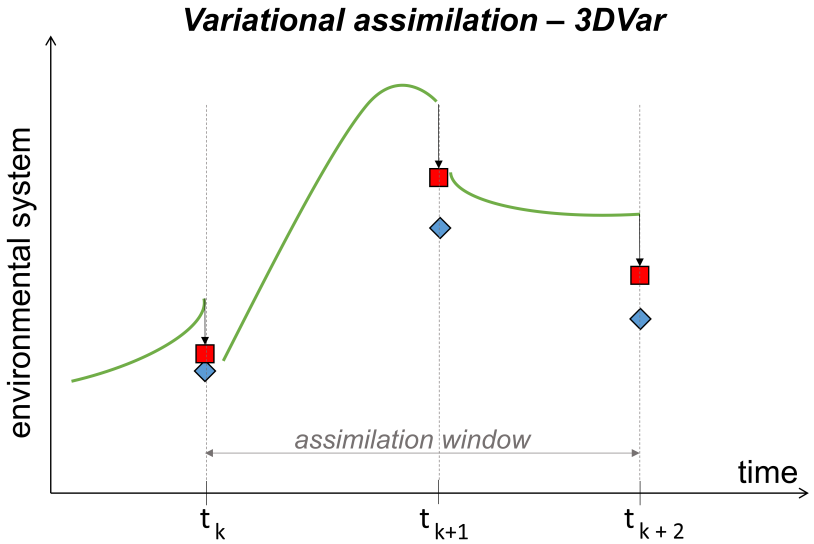

Figure 3.2: Illustration of 3D-Var variational problems. (Carrassi et al., 2018).

Four-dimensional variational data assimilation (4D-Var)

In the 4D-Var approach the control variable is the entire trajectory within the assimilation window ($[t_k, t_{k+2}]$ in Figure 3.3), and the corrections (black arrows) are computed and utilized at the observation times. The analysis trajectory (red line) is moved toward the observations (blue diamonds) respect with the forecast, depicted by the green line. For a generic observation time t_k, the control vector V and the observations Y are related by:

$$Y_{t_k} = G_{t_0 \to t_i}(V) \tag{3.13}$$

In this case the cost function and its gradient are given by equations 3.9 and 3.10.

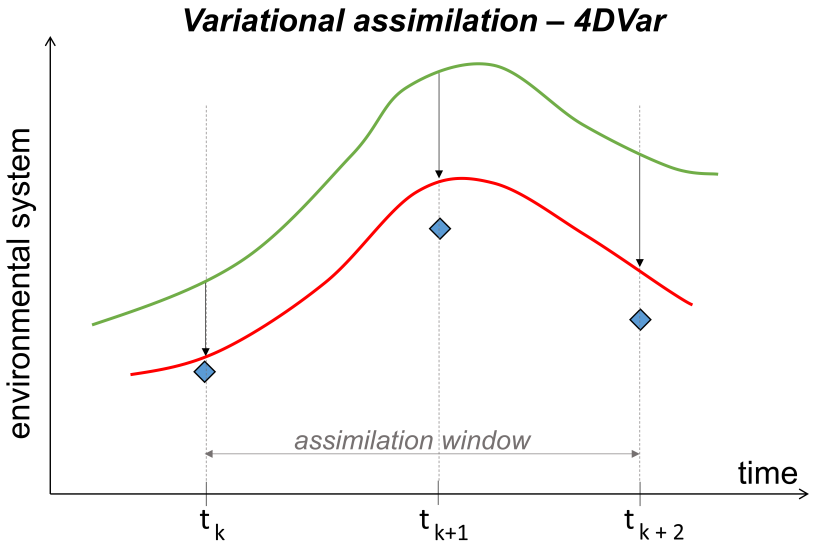

Figure 3.3: Illustration of 4D-Var variational problems. (Carrassi et al., 2018).

3.2 Satellite data and area of study

3.2.1 SWOT: Surface Water and Ocean Topography

The oceanography and surface freshwater hydrology communities proposed a new mission named SWOT for a better understanding of the world's oceans and its terrestrial surface waters. SWOT aims at observing how water bodies change over time, recognizing the potential of high-resolution, space borne measurements of water surface elevations. SWOT is jointly developed by NASA and Centre National D'Etudes Spatiales (CNSE) with contributions from the Canadian Space Agency (CSA) and UK Space Agency.

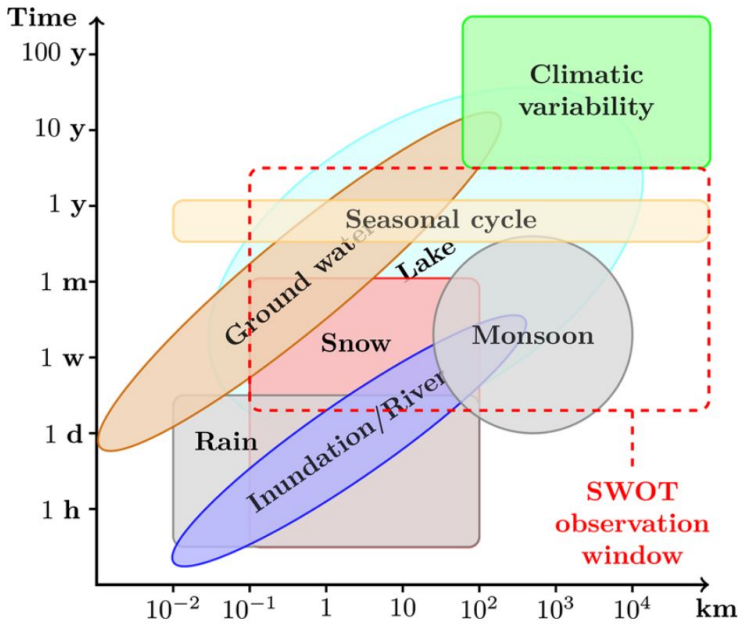

Figure 3.4: Time–space diagram of continental water surface processes and SWOT observation window. (Biancamaria et al., 2016).

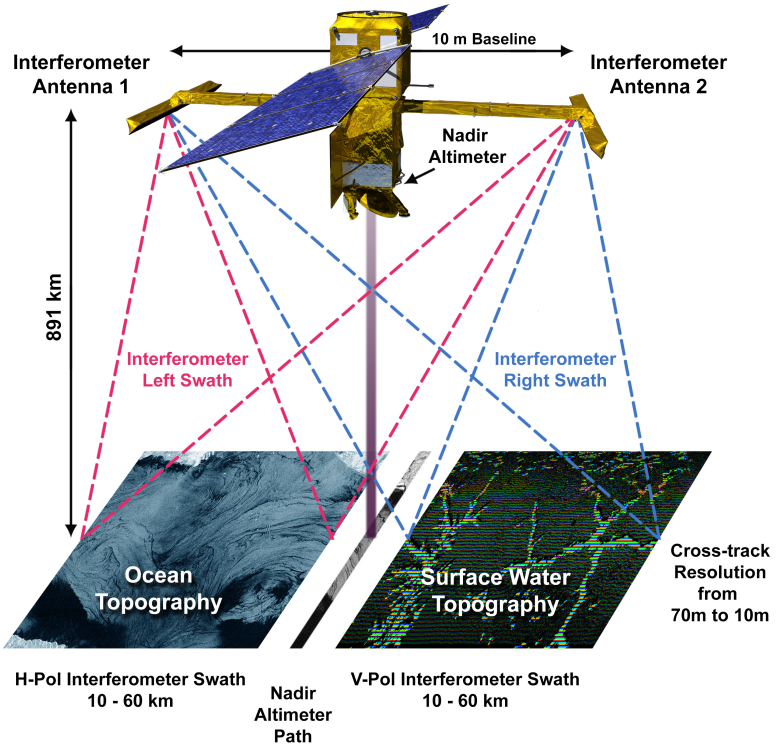

Figure 3.5: A diagram illustrating the swaths of data that SWOT will collect. The interferometer will produce two parallel tracks, with a Nadir track from a traditional altimeter in the gap between the swaths. The overall width of the swaths will be approximately 120 km, ©JPL.

Regarding the rivers monitoring, SWOT will provide detailed information about river storage, discharge, water surface elevation variations at global scale. The assessment of spatial and temporal dynamics of water bodies, even if pivotal, is nowadays challenging: hydraulic river variables (i.e. stage, velocity and discharge) are function of several aspects, such as vegetation, soil and bedrock characteristics, precipitation (Biancamaria et al., 2016). Figure 3.4 represents the space-time scale of several hydrological processes (i.e. snow, rainfall, groundwater) and the SWOT observation window. Note that the climatic variability is out of the scope of SWOT mission, unless combined with complementary observations (Oubanas, 2018).

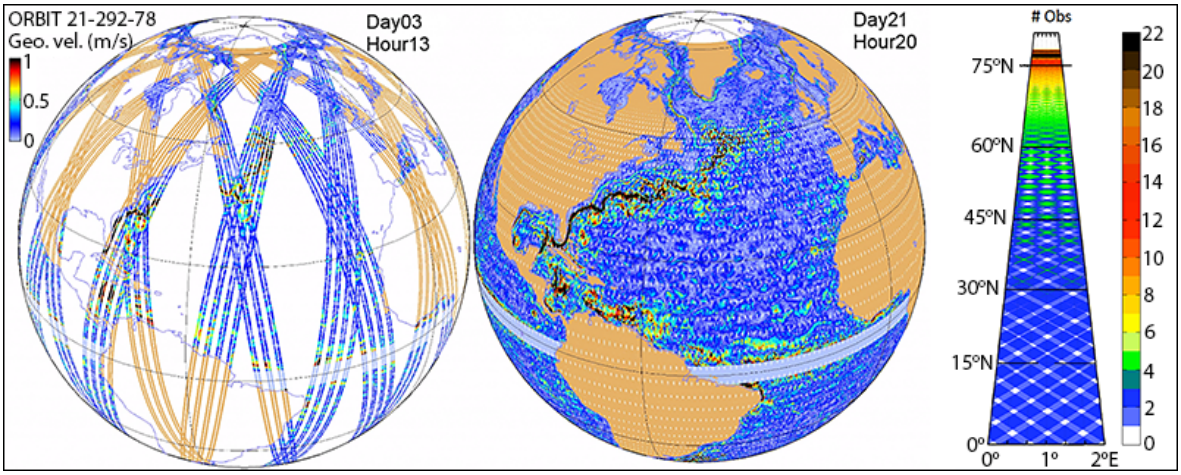

Figure 3.6: SWOT's nominal coverage during its 3-year science orbit will include measurements between 78°N and 78°S collected over a period of 21 days. Maps show the coverage after 3 days (left) and the full 21 days (center) of a complete cycle. The graphic at the far right illustrates the number of observations at a given latitude during the 21-day repeat period, ©JPL.

The core technology on-board the satellite is the Ka-Band Radar Interferometer (KaRIn) instrument, originally developed from the efforts of the Wide Swath Ocean Altimeter (WSOA). Figure 3.5 shows a conceptual view of the KaRIn instrument. KaRIn is a SAR interferometer observing the KA-band (35.75 GHz frequency), relying on the measurement of the relative delay between the signals measured by two antennas separated by a known distance (10 m) named "baseline", together with the system ranging information, to derive the height for every imaged pixel in the scene. In this way for each ground point a triangle is formed by the baseline and the distances of the two antennas, used for geolocation. Two consecutive radar (red and blue dashed lines Figure 3.5) pulses are exploited to find the relative phase difference between the two signals.
The main advantages in the choice of Ka band is the use of small wavelengths that limit specular reflection and penetration of the electromagnetic wave into soil and vegetation and reduce costs given the shorter baseline. The KaRIn instrument would be

complemented with a Jason-type (C- and Ku-band) nadir-looking conventional altimeter, a three-frequency microwave radiometer, similar to the Advanced Microwave Radiometer (AMR) flown on the Ocean Surface Topography Mission (OSTM), as well as GPS receivers and a DORIS transponder for precise orbit determination (POD).
SWOT mission can investigate rivers wider than 100 m, providing information about WSE, slope and width. Unfortunately, KaRIn measurements are affected by random noise, due to thermal noise and speckle effect (Biancamaria et al., 2016).

The latter is a result of the interference of many waves of the same frequency, having different phases and amplitudes, which add together to give a resultant wave whose amplitude, and therefore intensity, varies randomly. These errors provide a height bias of several meters: in order to obtain a centimetric height precision, spatial averaging over water pixels is performed (Oubanas, 2018).
Figure 3.6 illustrates the SWOT lifetime phases: the calibration/validation phase and the nominal phase. During the first one the satellite follows the fast-sampling orbit with 1-day observation frequency. The collected data have to be validated by independent observations (i.e. in-situ data). In the second phase, the orbit is modified resulting in a repeat period of about 21 days and a global coverage of a 90% of all water bodies.

3.2.2 Study area and available data

This investigation refers to the same 132-km Po river stretch analysed in Section 2.3.1. The study covers a period of about one year, that goes from May 2008 to April 2009. Thus, referring to this period of time and to foreseen SWOT orbits, the survey area is observed by the left and right swaths of the pass 0560, the left swath of the pass 0211, and the right swath of the pass 0489 (Figure 3.7).
The hydrodynamic model at the base of this analysis exploits the flow hydrograph and the observed water surface elevation as upstream and downstream boundary conditions, respectively. Figure 3.8 shows the hydrograph at Borgoforte gauging station, the reference data used in phase of validation. A strong discharge variability is evident, ranging from 565 to 6580 m^3/s during the observation period. The vertical dashed line in Figure 3.8 represent the SWOT overpasses times, indicating also the SWOT observations for the DA discharge estimation.

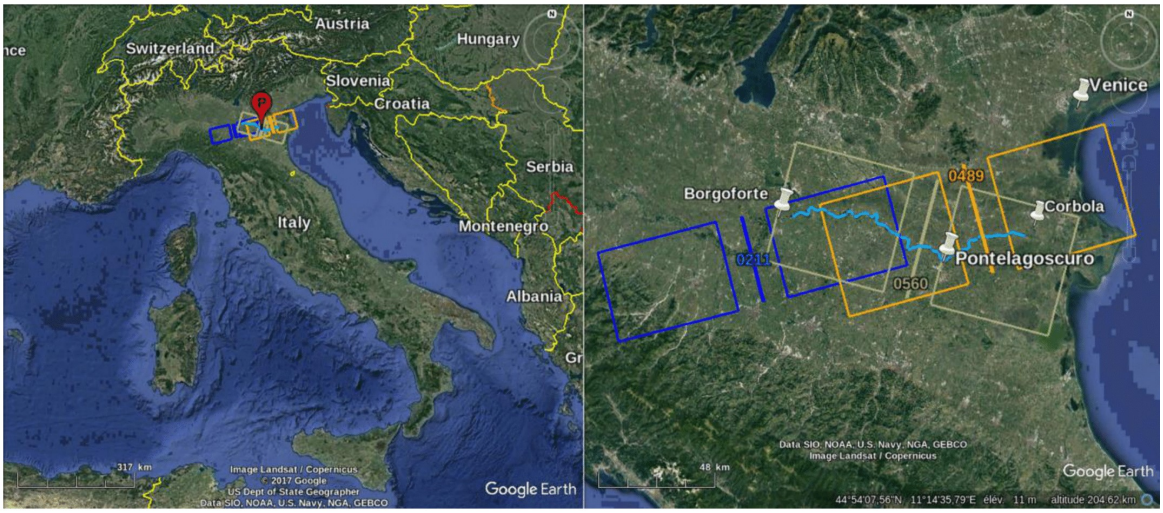

Figure 3.7: The Po River study area with the ground track of SWOT overpasses (Oubanas et al., 2018a).

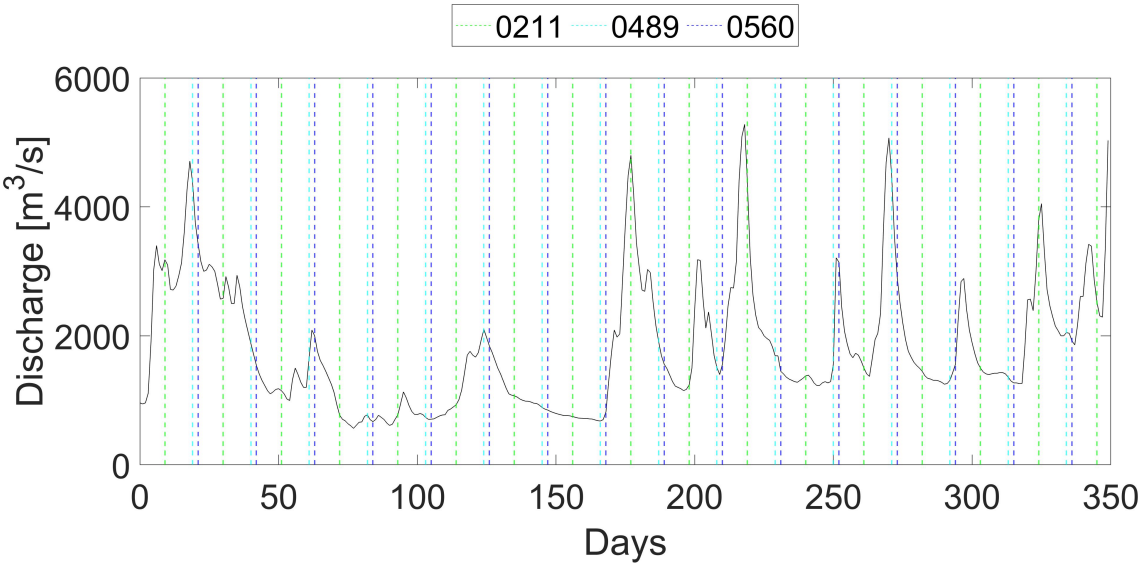

Figure 3.8: Hydrograph at Borgoforte gauging station (black) relative to the observation period (May 2008 - April 2009). The vertical dashed lines indicate the timing of the SWOT overpasses.

SWOT simulator

Since the SWOT satellite launch is planned for 2022, to accurately evaluate its performance, Jet Propulsion Laboratory (JPL) has developed several data product simulators at different levels of fidelity and complexity. Two separate simulators have been developed specifically for the hydrology data products. The SWOT Hydrology L1b Simulator produces synthetic radar interferograms of the scene exploiting as inputs the orbit, radar parameters (e.g. power, bandwidth, baseline) and the DEM of the study area. These

interferograms contains no noise that are added, modelled as correlated circular Gaussian noise, from the simulator subsequently. The SWOT Hydrology L2 Simulator uses the output of the L1b simulator to produce the final height and classification products (i.e., a pixel cloud with target class, elevation and area for each pixel, for more details see Gaultier et al., 2017; Frasson et al., 2017; Oubanas, 2018). The pixel clouds are processed by means of the RiverObs package developed at JPL (Frasson et al., 2017). This tool can aggregate the 2D pixel clouds into nodes with regular spatiality on the river centerline, estimating averaged height, width and uncertainties at each node. The user has to impose a search window in which the pixel located are assigned to the considered pixel. For this survey area, a 1600 m wide search window is used for all but the three highest flow overpasses, for which the values is increased to 5000 m (Oubanas et al., 2018a).
The observations from the SWOT simulator are affected by bias. In particular, the orientation of the river centerline respect to the satellite swath is the main factor to be considered: it is important when the river is parallel to the swath, it is negligible when the river is perpendicular to the swath, like in the current study (Oubanas et al., 2018a). For more information about SWOT data characteristics, see Frasson et al. (2017).

3.3 Experimental design

The present work consists in the application of a variant of 4D-Var method presented in Gejadze and Malaterre (2016, 2017) on the 132-km stretch of Po River, basing on space-borne observations (i.e. SWOT). In particular, the proposed analysis follows the framework proposed by Oubanas et al. (2018a).
The dynamic model (M) is SIC^2, built on the cross-sections derived from SRTM and modified with RiBEST tool (Section 2.2). The model input vector U is formed by several variables:

$$U = (z_0, q_0, Q, p_{rc}, Q_L, C_L, K_s, Z_b, p_g, p_{nm})^T \tag{3.14}$$

The variables of interest (vector V) to be estimated simultaneously are:

$$V = (Q(t), K_s(t)) \tag{3.15}$$

while the observations consist in the water surface elevation data provided by SWOT simulator at RiverObs nodes and for SWOT overpasses (Parapragh 3.2.1).
Regarding the computation of first guess model inputs (i.e., background information), Q_b derives from the global Water Balance Model (WBM) (Wisser et al., 2010), while the prior information of K_s is imposed referring to a realistic value for the study case.

The length of the subwindow is arbitrary, taking into consideration that the longer the subwindow size, the more the computational memory required. In this case, being the entire observations period of 350 days, each subwindow is of 42 days, excepting the last one of 56 days. The background values of discharge (i.e. 841 m^3/s) is imposed for the first subwindow, while for the subsequent ones the prior discharge information corresponds to the estimated discharge value relative to the last instant of the previous subwindow.

About the DA approach, a variant of eq. 3.9 is used (see Gejadze and Malaterre, 2017, for more details):

$$J(V,\alpha) = \frac{1}{2}||R^{-1/2}(G(V,U_b) - Y^*)||^2 + \frac{\alpha}{2}||B^{-\frac{1}{2}}(V - V_b)||^2 \tag{3.16}$$

where α is a regularization parameter to reduce the impact of possible error in assigning B.

The DA estimation performances are measured by means of the following error metrics:

- Mean Absolute Error (MAE):

$$MAE = \|Q_e(t) - Q_t(t)\| \tag{3.17}$$

- Root Mean Square Error (RMSE):

$$RMSE = \sqrt{\frac{1}{T}\sum_t (Q_e(t) - Q_t(t))^2} \tag{3.18}$$

- relative Root Mean Square Error (rRMSE):

$$rRMSE = \sqrt{\frac{1}{T}\sum_t \left(\frac{Q_e(t) - Q_t(t)}{Q_t(t)}\right)^2} \tag{3.19}$$

- Normalized Root Mean Square Error (NRMSE):

$$NRMSE = \frac{1}{\bar{Q}_t}\sqrt{\frac{1}{T}\sum_t (Q_e(t) - Q_t(t))^2} \tag{3.20}$$

- Nash-Sutcliffe Efficiency (NSE):

$$NSE = 1 - \frac{\sum_t (Q_e(t) - Q_t(t))^2}{\sum_t (\bar{Q}_e(t) - Q_t(t))^2} \tag{3.21}$$

- Volumetric Efficiency (VE):

$$VE = 1 - \frac{\sum_t \|Q_e(t) - Q_t(t)\|}{\sum_t Q_t(t)} \tag{3.22}$$

where $Q_{\mathrm{e}}(t)$ and $Q_{\mathrm{t}}(t)$ are the estimated and reference discharge respectively, $\bar{Q}_t(t)$ the mean reference dischage, t the number of observations (i.e. 52 considering SWOT overpasses time, 350 a daily computational Δt) and T the length of observation periods (i.e. 350 days).

3.4 Results and discussion

Table 3.1 reports DA discharge estimation performances for irregular (i.e. SWOT overpasses time, called "SWOT-ΔT") and daily computational ΔT. The Figure 3.9 shows the comparison among reference (i.e. Borgoforte hydrograph, black line) and the estimated discharge (purple line). As shown in Table 3.1, using the SWOT-ΔT the error metrics improve with respect to the daily computational ΔT (i.e. RMSE of 191.4 and 616.0, NSE of 0.78 and 0.61, respectively).

Table 3.1: Performances on discharge estimation with DA approach for the different temporal discretization.

Computational ΔT	**MAE** [$\mathbf{m^3/s}$]	**RMSE** [$\mathbf{m^3/s}$]	**rRMSE** [%]	**NRMSE** [%]	**NSE** [-]	**VE** [-]
SWOT-ΔT	335.1	191.4	10.2	10.5	0.78	0.82
Daily	431.5	616.0	32.2	33.9	0.61	0.76

This is partly due to the fact that the proposed discharge trend (purple line in Figure 3.9) represents an hypothesis of the river flows values during the period that goes from two consecutive SWOT overpasses (black points, Figure 3.9), when DA analysis is applied. In some cases, this introduces significant discrepancy with respect to the reference hydrograph (i.e. yellow dashed boxes in Figure 3.9). For this reason, the error metrics for irregular computational ΔT are more representative. The mean ΔT on the entire observation period is about 7 days. A possible solution to overcome this limit is the consideration of multimission data, perhaps including JASON, ENVISAT and Sentinel data to reduce the average temporal discretization of observations.

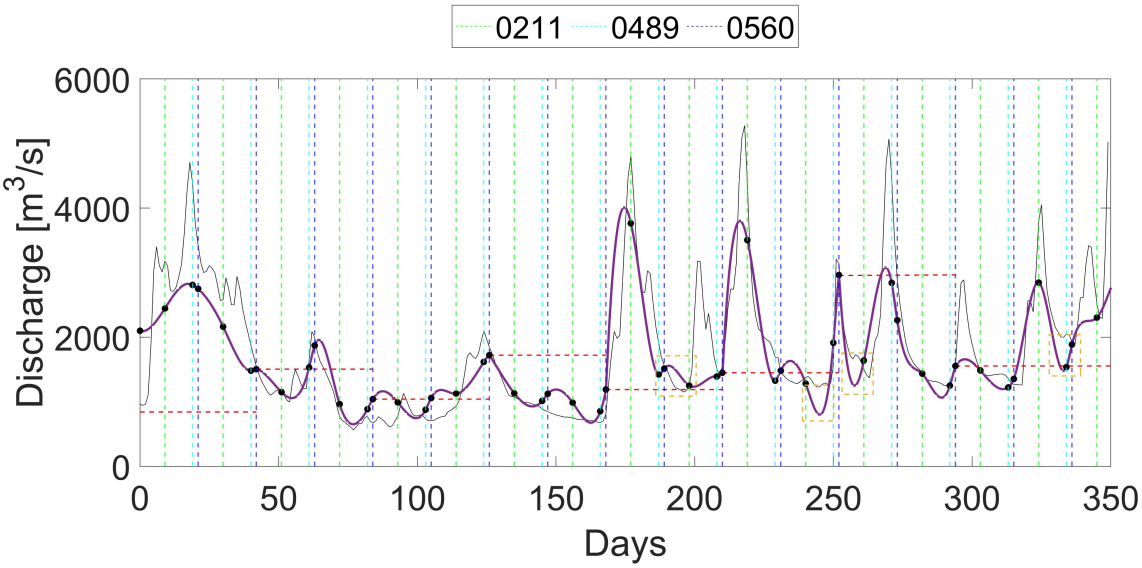

Figure 3.9: The black points represent the discharge values estimated at SWOT overpasses (dashed vertical lines) estimated with DA approach. An hypothetical trend among two satellite overpasses is depicted by the purple line. The red dashed line shows the discharge background value for each subwindow.

In general a peak discharge underestimation can be noticed. Starting from this consideration, Table 3.2 shows discharge estimation with DA performances considering separately low flows (i.e. $Q(t) \leq 2000$ m^3/s; 39 observations) and middle-high flows (i.e. $Q(t) > 2000$ m^3/s; 13 observations). In accordance with Figure 3.9, low flows are better represented by DA estimation (i.e. RMSE of 75.8 and NSE of 0.72).

Table 3.2: Discharge estimation with DA approach performances for SWOT overpasses time discretization for low (< 2000 m^3/s) and medium-high (> 2000 m^3/s) flow values.

Discharge range [**m^3/s**]	**MAE** [**m^3/s**]	**RMSE** [**m^3/s**]	**rRMSE** [%]	**NRMSE** [%]	**NSE** [-]	**VE** [-]
0 - 2000	176.5	75.8	6.9	5.7	0.72	0.87
> 2000	837.2	175.7	7.5	5.2	0.16	0.75

Figure 3.10 depicts the Strickler coefficient K_s along the study area (i.e. 132 km). The reference Strickler trend (black line Figure 3.10) reports the best Manning's coefficient combination of the reference model, considering the Po River stretch subdivision (see Figure 2.7). Notwithstanding K_s provides representative values locally, Strickler estimation trend is fluctuating, in particular for the upper-middle reach. This behaviour is typical of ill-posed estimation problems, the so-called "equifinality issue". Thus, K_s may not provide a reliable global information of bed roughness.

The approach limits in Q and K_s estimation partly might be due to the inaccuracy introduced by the cross-section representation (i.e., SRTM integrated with RiBEST-derived bathymetry). Further work will test the use of SWOT data, which is expected to be able to reproduce the actual spatial sampling patterns.

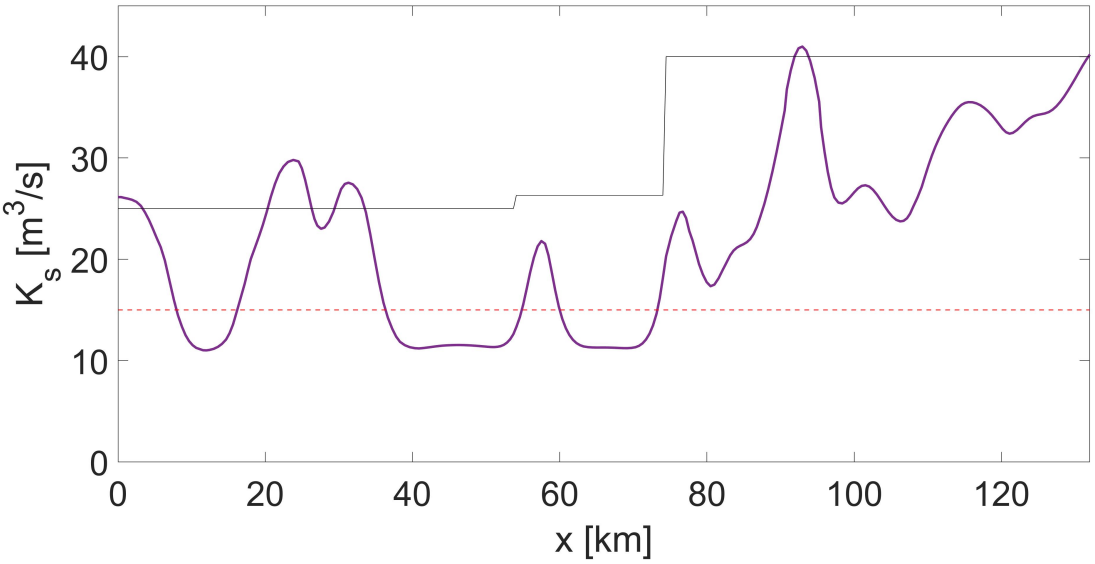

Figure 3.10: Strickler coefficient estimation (purple line) and reference one (black line) along the study area. The background values is depicted by dashed red lines.

3.5 Concluding remarks

This work proposes a discharge estimation method based on DA approaches and solely space-borne information (i.e. SWOT) and global available data (i.e. WBM). In particular, a 4D-Var method is exploited, making several modifications to the classic approach applied to the full Saint-Venant-based hydraulic model SIC^2. This implemented version overcomes computer resources limitations (i.e. memory limits), allowing the applicability of the classical data assimilation methods to long-time periods.

In order to propose a method for ungauged basins detection, in-situ information are not used. The main information (i.e. water surface elevation) derives from synthetic SWOT overpasses generated with the SWOT simulator developed at the JPL. The survey area refers to the 132-km Po River stretch (from Borgoforte gauging station to the beginning of river delta) for an observation period of 350 days (May 2008 - April 2009). The hydraulic model SIC^2 is built on the cross-sections profiles derived from SRTM and modified with RiBEST tool (see Section 2.2), in order to assess how the bathymetry knowledge affects the DA discharge estimation. Considering an irregular computational ΔT (i.e., the SWOT overpasses times), the DA estimation provides better results with respect to the use of

daily ΔT (see Table 3.1). In general, even if a good dynamism is represented (Figure 3.9), a underestimation of discharge peaks can be noticed. Analysing DA performances considering low flow values (i.e., 0 - 2000 m^3/s) and middle-high flow ($>$ 2000 m^3/s), an improvement of error metrics for low discharges is evident (i.e., RMSE of 75.8 m^3/s, rRMSE of 6.9 %). In this analysis, $Q(t)$ is simultaneously estimated with the Strickler coefficient K_s. It presents a fluctuating trend along the study area, not providing a reliable global information of bed roughness.
Future researches will investigate on approach limitations, such as the reduction of computational ΔT exploiting multimission data (i.e., ENVISAT, Jason-2, etc). Moreover, the geometric representation of cross-sections profiles (i.e., SRTM integrated with rectangular channel shape) should be provided by other satellite information (i.e., SWOT).

CHAPTER 4

Satellite altimetry for calibration of hydraulic models

I saw for the first time the earth's shape. [..] The horizon is dark blue, smoothly turning to black... the feelings which filled me I can express with one word — joy.

Yuri A. Gagarin
Life Magazine, 21th April 1961

This Chapter contains:

4.1 Altimetry data series: investigated satellite products and Multi-Mission series (MM)

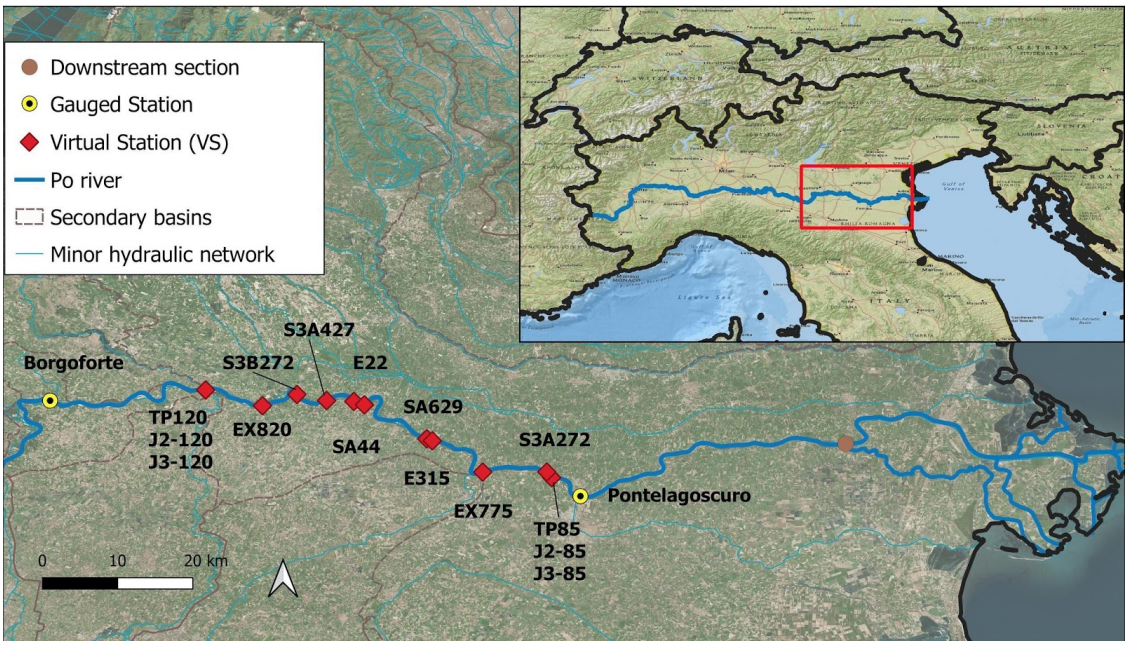

Figure 4.1: Po river stretch considered in the study (140 km, from Borgoforte to the beginning of the river delta) with the identification of gauged stations and the Virtual Stations (VSs) relative to the overall set of satellite missions.

As introduced in Section 1.4, the use of satellite altimetry information is strongly consolidated for hydraulic applications. The present work investigates the potential of several satellite altimetry missions data, covering about 27 years, for hydraulic modelling. In particular, the focus is on the investigation of the record length (i.e., number of available satellite measurements, in relation to different data products) effect on the calibration reliability. Finally, to overcome the space-time limitations of original missions, an approach that combines different single-mission time series (Multi-Mission series, MM) is presented.

Table 4.1 summarizes the different altimetry missions considered in the study (Figure 4.1): Envisat (E), Envisat Extended Mission (EX), TOPEX/Poseidon (TP), SARAL/AltiKa (SA), Jason-2 (J2), Jason-3 (J3), Sentinal-3A (S3A) and Sentinel-3B (S3B). These missions are characterized by different sensors, instrumentation, scopes, and orbits. Therefore, the respective altimetry time series are characterized by distinctive temporal and spatial resolution as well as different accuracy and reliability. Most of the considered missions have a low temporal resolution (i.e. 35 days for E and SA, 30 days for EX, and

27 days for S3A and S3B), while TP, J2 and J3 provide water surface elevation measurements every 10 days. E (mission period 05/2002–10/2010) and SA (03/2013–01/2016) are the successors of the former mission ERS-2 (04/1995–09/2007) using the same orbit configuration with inter-track distance of 80 km at equator and a repeat cycle of 35 days. E, EX, and SA data are processed adopting ICE-1 retracker, shown to provide robust and accurate results over rivers. J2, launched in June 2008, is the successor of the former missions TP (09/1992–08/2002), and J3 was launched in 2016 as the successor of J2 and placed in the same orbit with the inter-track distance of about 315 km at equator and a repeat cycle of 10 days.

For both J2 and J3, the water levels are derived using the ICE retracker, as it has proven to outperform other retrackers over continental waters Cretaux et al. (2018). The currently active S3A and S3B guarantee the continuity of E-type measurements in a fully operational manner. Sentinel-3 provides SAR altimetry data with a revisit time of 27 days. The two missions have orbits almost similar to that of E and ERS, with the ground-track separation of 104 km at equator. S3A and S3B data are processed using the OCOG retracker which is a heritage of ICE-1, and hence, reliable for inland applications.

All water level time series are processed using the high-rate altimetry datasets. The usual rate for all missions is 20 Hz which leads to the along-track distance of 294 m between successive measurements. SA dataset however is provided with the sampling rate of 40 Hz, and hence, the spatial spacing of 173 m along-track. For clarity, Figure 4.2 presents the temporal coverage of the altimetry products considered in the study, while Figure 4.3 reports a synoptic view of the water levels derived from the different missions.

Referring to the same study area, Tarpanelli et al. (2013a) and Domeneghetti et al. (2014, 2015b) investigated the potential of ERS-2 time series for similar purposes. The comparison of ERS-2 with water level values recorded at the nearest gauging station, or estimated at VSs, shows significant correlations, with the mean absolute error in the order of 0.7 m. In particular, Domeneghetti et al. (2015b) investigated the effect of ERS-2 uncertainty on model calibration, while Schneider et al. (2018) did the same considering CryoSat time series. For the sake of brevity, and to avoid the repetition of already performed investigations, calibrations with ERS-2 and CryoSat data are not carried out in this work. Actually, the drifting orbit of CryoSat implies a long-repeat ground track pattern that would impose the adoption of different calibration strategies (i.e., it is not straightforward to construct time series since its long repeat cycle – 369 day). Nevertheless, this does affect the completeness of this investigation: results previously obtained with both ERS-2 and CryoSat are summarized and compared with those of other altimetry time series to provide a complete overview of altimetry performance.

Table 4.1: Satellite sensors and altimetry time series considered in this study.

Mission (Abbreviation)	Version	Retracker	Observation period	Temporal [day]	Height [km]	Inclination	Data source
TOPEX/Poseidon (TP)	MGRD-B	onboard	1992-2002	9.91	1136	66	PODAAC
Envisat (E)	GRD-V3	ICE-1	2002-2010	35	800	98.5	ESA
Envisat XT (EX)	GRD-V3	ICE-1	2010-2012	35	800	98.5	ESA
SARAL/AltiKa (SA)	GRD-t	ICE-1	2013-2016	35	800	98.5	AVISO
JASON 2 (J2)	PISTACH	ICE-3	2008-2015	9.91	1336	66	AVISO
JASON 3 (J3)	GDR-d	ICE	2016-2019	10	1336	66	AVISO
Sentinel-3A (S3A)	O NT 003	OCOG	2016-2019	27	814.5	95.65	COPERNICUS
Sentinel-3B (S3B)	O NT 003	OCOG	2018-2019	27	814.5	95.65	COPERNICUS
Multi-mission (MM)			1995-2019	c.a. 3			

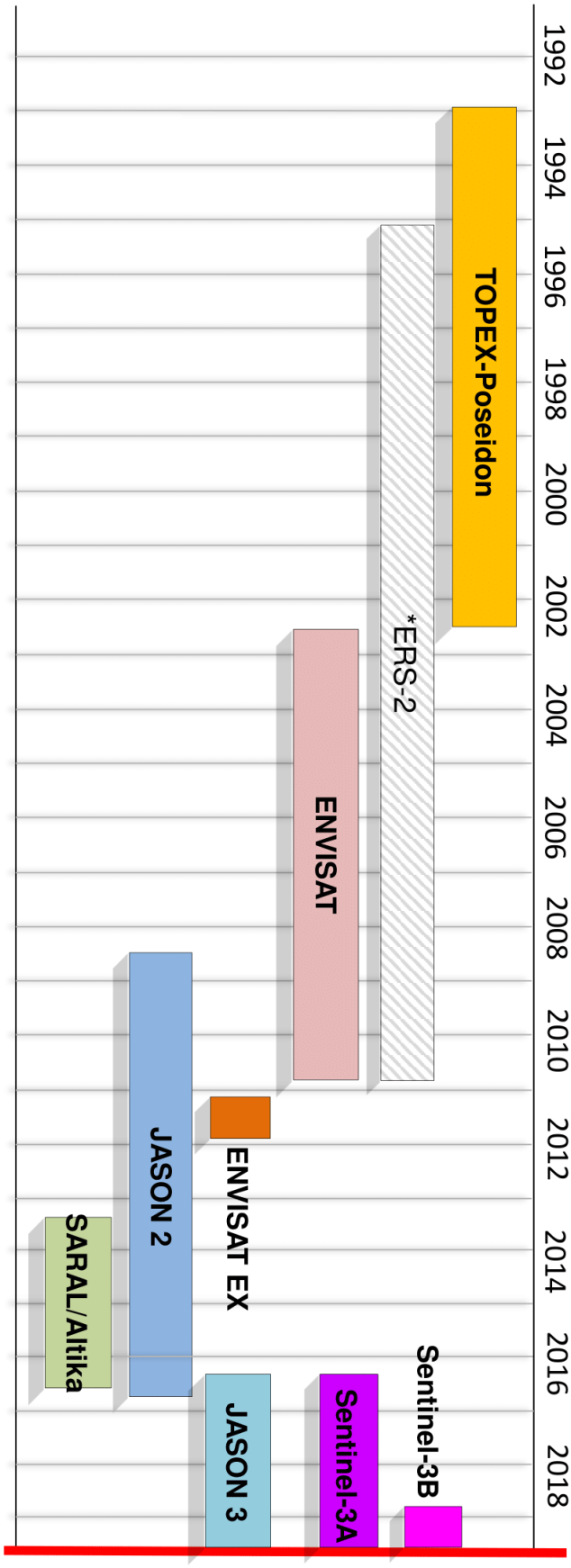

Figure 4.2: Temporal distribution of satellite altimetry missions used in this work: TOPEX/Poseidon, Envisat, Envisat EX, JASON-2, SARAL/AltiKa, JASON-3, Sentinel-3A, and Sentinel-3B (*ERS-2 is reported for comparison with other studies in literature).

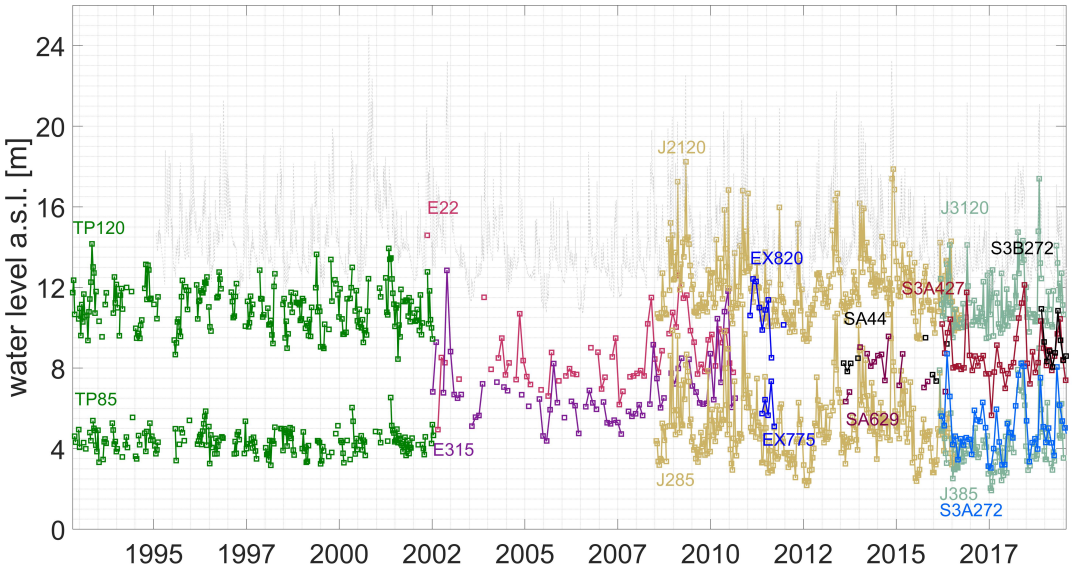

Figure 4.3: Synoptic view of altimetry time series at VSs identified along the river stretch of interest. The grey dashed line reports water levels observed at Borgoforte.

Multi-mission (MM): altimetry time series at high spatial and temporal coverage

Water level time series from individual altimetry missions over the river are merged using an approach developed by Tourian et al. (2016) to overcome spatial and temporal limitation of single altimetry missions. Adopting this solution all VSs of several satellite altimeters along the Po River are connected to each other hydraulically and statistically. To this end, first the bias between different missions is removed (see Tourian et al., 2016, for more details). Then, for any given location along the river, the time lag due to stream flow between the altimetric virtual stations and the selected location is estimated.

Since the MM approach has been developed for being applicable also on poorly surveyed areas, average river width using imagery together with the slope derived from satellite altimetry are used as inputs to a simple empirical hydraulic equation that estimates average flow velocity and thus the time lag between VSs (Bjerklie et al., 2005; Tourian et al., 2015). Figure 4.4 shows the estimated time lag between VS along the Po River highlighted with those selected for this study. From the most upstream selected VS in this study (TP120, J2-120 and J3-120; see Figure 4.1) till most downstream VS (TP85, J2-85 and J3-85), the time lag is about 0.85 day. Using the estimated time lag, the water level hydrographs of all measurements are shifted and stacked at the selected location. The stacked time series at the selected location is then normalized according to its statistical distribution and especially the water level value at 3rd and 85th percentiles as lower and upper bounds. As an example, Figure 4.5 shows normalized water level obtained at VS

J2-85, for which first the time lag between all VSs and the J2-85 is corrected and then individual time series are normalized according to their 3rd and 85th percentiles.

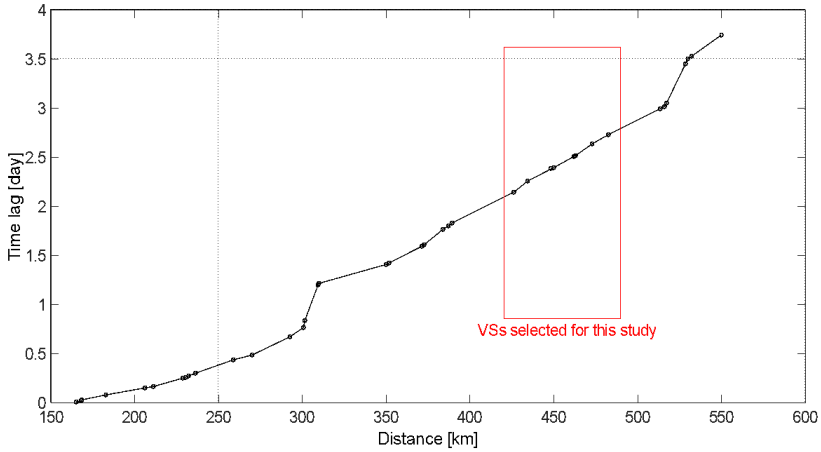

Figure 4.4: Estimated time lag between each VS along the Po River relative to the very first VS. The red box highlights VSs selected for this study (from Tourian et al., 2016).

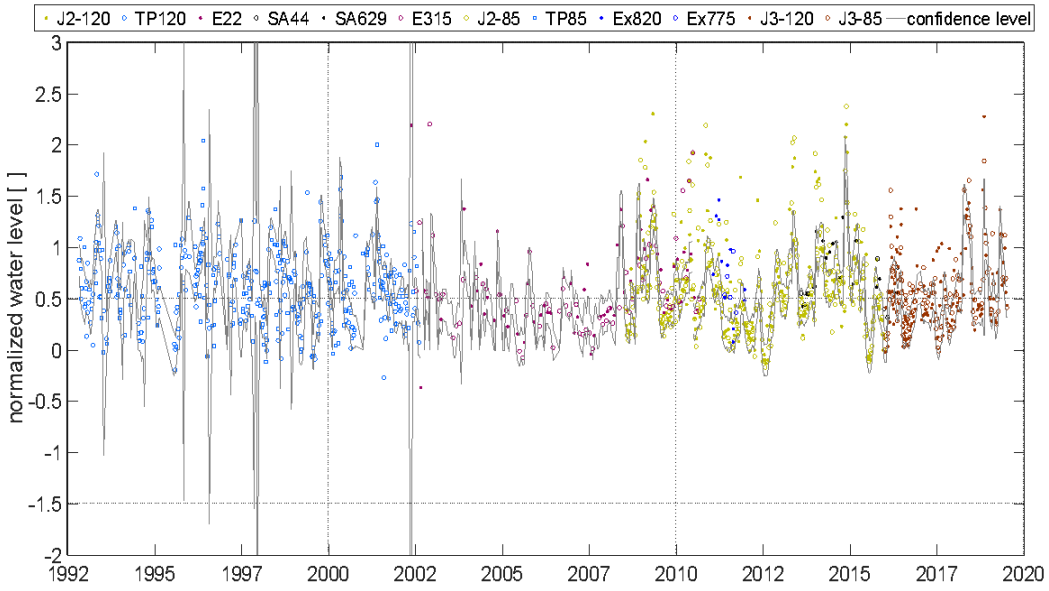

Figure 4.5: Normalized water level values at VS J2-85. The grey curves show the boundaries of confidence limit after rejecting all possible outliers.

Afterwards, outliers are identified and removed from the normalized time series by defining a confidence limit of 99% of a Student's t test for a one month sliding time window. The confidence limit is delineated in Figure 4.5 by an upper- and a lower bound confidence level. All measurements outside the confidence limit are identified as outlier and removed from measurements. The outlier-free normalized time series is then rescaled

back according to the water level distribution of the selected location (Figure 4.6). Using this methodology, we obtain a time series with 3 days effective temporal resolution from altimetry missions originally with temporal resolution ranging from 10 to 35 days. The MM water level time series are validated at the gauging stations of Borgoforte and Pontelagoscuro, for which individual water level time series are densified, obtaining correlation coefficient equal to 0.75 and 0.78, RMSE of the value of 0.94 m and 0.75 m, and bias of 0.05 and 0.37 m, respectively. The accuracy of MM series inevitably conveys the simplifications and assumptions of the approach used for their construction. Thought for applications in data scarce areas, those simplifications mainly regards the description of the river geometry and dynamics (i.e., river width and time lag). Investigating the impacts of such limitations on the use of MM series for the calibration was out of the scope of this work. Nevertheless, these analyses are suggested for future work.

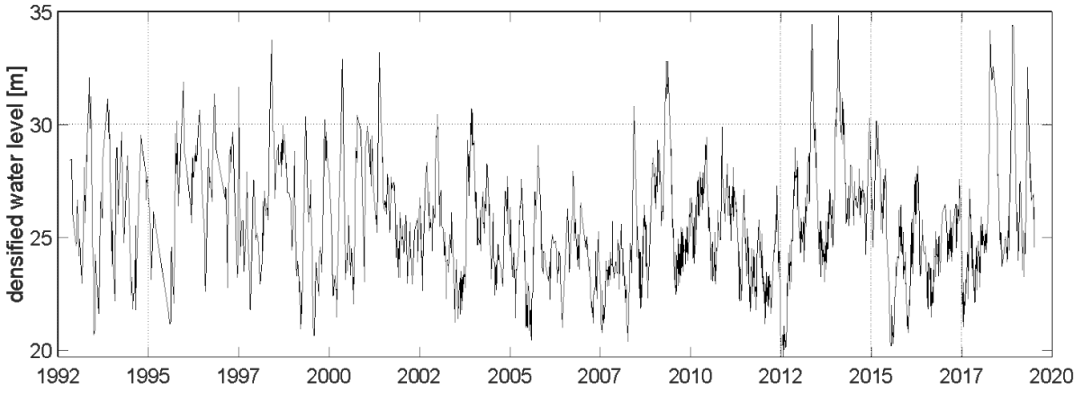

Figure 4.6: Densified water level time series at VS J2-85.

4.2 Numerical analysis and methodology

4.2.1 Model set up, calibration and validation

The numerical simulations of the river stretch of interest is carried out by means of a quasi-two-dimensional (quasi-2D) model implemented with the HEC-RAS code. The river geometry is properly reproduced by taking advantage of a 2-m DEM available along the overall Po river, which combines a LiDAR survey of the emerged river portion with traditional ground cross-sections and multi-beam sonar surveys (Camorani et al., 2006). The quasi-2D scheme ensures a proper representation of the flow dynamics by enabling mutual interactions between the main channel and a series of lateral floodplains (i.e. storage areas) delimited by a system of minor dikes, which are schematized within the code as lateral structures. Although the numerical scheme refers to 1D hydraulic equations, the

adoption of this schematization enables a proper simulation of the hydraulic interaction among the main channel and lateral floodplains. The appropriateness of this configuration has been proven by a number of previous studies that referred to the same river portion (Castellarin et al., 2011; Domeneghetti et al., 2015b). The numerical simulations for the overall period of interest (1992-2019) are carried out by imposing the mean daily discharge values recorded at the upstream gauged station (Borgoforte) as upstream boundary conditions, and the normal flow condition at the downstream cross-section located at the beginning of the river delta (see Figure 4.1). According to previous experiences on the study area (Domeneghetti et al., 2014, 2015a), lateral inflows of some minor tributaries are not taken into account during the simulation since their contributions are neglectable relative to the Po river discharge. The calibration procedure focuses on the identification of the Manning coefficient, n ($s \cdot m^{-1/3}$), of the main channel that maximizes NSE obtained in reproducing the observed water levels, by varying it within the range 0.01-0.06 $s \cdot m^{-1/3}$. Because the quasi-2-D model has limited sensitivity to the roughness coefficient adopted for the floodplains, its value is considered constant and equal to 0.1 $s \cdot m^{-1/3}$ for all the numerical simulations (see e.g. Castellarin et al., 2011; Domeneghetti et al., 2015a).
Referring to the simulation time frame considered in this study (1995-2019), calibration and validation schemes vary in relation to investigation setting, as indicated hereafter:

- a) analysis considering one VS at time, referring separately to the dataset retrieved from specific altimetry mission (Table 4.1, Figure 4.1) and the MM time series. In each calibration, the roughness coefficient is unique and assumed to be static through time. For each single mission the calibration is performed referring to the overall period of altimetry data availability (see Figure 4.3), once calibrated, the model validation is carried out comparing simulated water surface levels with the in-situ data available within considered time frame (1995-2019) and not used for the calibration. For a single MM series that covers the overall period of interest, the latter is split in two parts: 1995-2017 for calibration, 2017-2019 for validation.

- b) Analysis considering all MM time series together: the calibration adopts spatially distributed parameterization by splitting the river into a number of stretches corresponding to VSs locations and considering multiple roughness coefficients.

When referring to MM time series, the calibration refers to the period covering the presence of all altimetry missions. Its considerable extent (22 years, from 1995 to 2017) provide a data series length sufficient to ensure a consolidated calibration, guaranteeing at the same time a sufficient validation period (2 years, 2018-2019).

4.2.2 Accuracy of altimetry products

Typically, as spotted in Figure 4.1, VSs do not coincide with gauging stations and thus a direct comparison between traditional observation and remotely sensed data is not straightforward. To overcome this problem we compare the satellite-derived water surface elevation values, $h_{sat}(x,t)$, sensed at a given location, x, at the day of the satellite overpass, t, with the in situ water surface elevation, $h_{situ}(x,t)$, linearly interpolated at the track location referring to concurrent water levels measured at the gauging stations located upstream and downstream the satellite track. This appears reasonable in the absence of diversion structures or dams along the river portion of interest. Following this approach, the error, $\varepsilon(x,t)$, can be calculated with the equation 4.1:

$$\varepsilon(x,t) = h_{\mathrm{sat}}(x,t) - h_{\mathrm{situ}}(x,t) \tag{4.1}$$

which has been applied distinguishing all the altimetry products.
The same approach is used considering the MM time series, where t covers all days of observation sensed by at least one of the considered altimetry missions. Considering that different altimetry missions use different reference ellipsoids (TOPEX ellipsoid for TP, J2, J3, and SA, and the WGS84 for E, EX, S3A, and S3B), we calculate the geoid height with respect to the one adopted for MM creation (EGM2008). The same for in situ data, which refer to ITALGEO 2005 geoid (Barzaghi et al., 2007).

4.2.3 Impact of VS time series length on calibration

The length of an altimetry dataset, m (i.e., the number of satellite overpasses available at a given VS from a specific altimeter, which differs from the official mission duration), influences the reliability of the calibration (Domeneghetti et al., 2015b). To investigate its impact for different satellite products we repeat the calibration exercise by considering several altimetry subsets randomly sampled from each original altimetry time series (i.e., E, TP, J2, etc.) with a length m that varies from 3 to L_{tot}. In this case, L_{tot} indicates the total amount of altimetric observations available for a given mission at a specific VS. Indicating with x the location of a given VS along the study area, the subset sampled from the original altimetry time series and used for the calibration can be expressed as:

$$h_{\mathrm{sat,m}}(x) = [h_{\mathrm{sat}}(x,t_1), ..., h_{\mathrm{sat}}(x,t_m)] \quad \forall m = 3, ..., L_{tot} \tag{4.2}$$

For m lower than 3, the time series is considered too short and not suitable for calibration purposes. To overcome the uncertainty related to the selection of the m observations among those available for a given mission, and at a given VS, the sampling procedure

is embedded in a Monte Carlo framework that generates 1000 random $h_{sat,m}$ samples for each m value. Once sampled, the calibration is carried out considering each $h_{sat,m}$ sample at time. Finally, with the aim to infer the error introduced by the altimetry data, we repeat the same procedure by calibrating the numerical model with reference to different subsets randomly extracted from the water level values observed in-situ at the VS (h_{situ}). Equation 4.3 indicates the in-situ time series randomly extracted from the overall set:

$$h_{\mathrm{situ,m}}(x) = [h_{\mathrm{situ}}(x, t_1), ..., h_{\mathrm{situ}}(x, t_m)] \quad \forall m = 3, ..., L_{tot} \tag{4.3}$$

Calibration results obtained with these $h_{situ,m}(x)$ samples are used as a reference for evaluating the potential of altimetry for model calibration. For what regards the adoption of MM time series, in order to make the calibration performances of MM and traditional time series comparable, we refer to specific observation periods instead of considering a given number of observations (m). The observation period is expressed in terms of a number of months from the date of the first altimetry observation and varies in relation to the revisit time of each mission: 12 months for TP, J2, and J3 (i.e., high-frequency missions), 14 months for S3A and 20 months for other missions. Based on this temporal discretization, once identified a given observation period (e.g., 1, 2, ..., n observation periods), the number of altimetry observations adopted for the calibration for both MM and traditional time series is defined as the sum of all available water levels values observed since the beginning of the time series.

4.3 Results

4.3.1 Accuracy of altimetry products

Table 4.2 summarizes the results of the comparison between altimetry time series and in-situ water surface elevations estimated at VS locations. In particular, the table reports the number of observations that constitutes each time series, the correlation coefficient (R) between altimetry and in-situ data, the NSE value, MAE as well as the mean (μ) and standard deviation (σ) of the errors expressed following equation 4.1. Altimetry products are listed in a chronological order following Figure 4.2. In case of VSs observed from multiple sensors (e.g. VS 85 and VS 120) each time series is considered separately.

Table 4.2: Comparison of satellite altimetry and in-situ water surface levels: distance from upstream cross-section, n° of satellite data (L_{tot}), correlation coefficient (R), Nash-Sutcliffe (NSE), Mean Absolute Error (MAE), error mean (μ) and standard deviation (σ).

VS	**distance [km]**	**n°data L_{tot}**	**R**	**NSE**	**MAE [m]**	μ **[m]**	σ **[m]**
TP120	25.44	174	0.77	0.37	0.67	-0.42	0.75
J2-120	25.44	298	0.98	0.93	0.29	0.18	0.38
J3-120	25.44	107	0.87	0.69	0.38	0.20	0.76
EX820	34.23	12	0.91	0.68	0.52	0.50	0.57
S3B272	42.24	14	0.96	0.93	0.25	0.00	0.32
S3A427	48.73	51	0.94	0.84	0.43	0.30	0.47
E22	49.60	61	0.85	0.72	0.34	0.05	0.87
SA44	50.89	8	0.92	0.41	0.46	0.14	0.55
SA629	65.84	15	0.96	0.72	0.44	0.40	0.30
E315	66.87	65	0.97	0.89	0.37	0.30	0.43
EX775	78.72	5	-0.35	-3.97	1.17	1.17	1.4
S3A272	86.76	51	0.96	0.65	0.88	0.84	0.50
TP85	88.11	158	0.6	-0.35	0.54	0.08	0.70
J2-85	88.11	294	0.98	0.94	0.29	0.20	0.37
J3-85	88.11	99	0.95	0.86	0.40	0.24	0.45

Table 4.3 reports the same error statistics referring to MM time series, which is unique for each VS.

Table 4.3: Comparison of MM time series and in-situ water surface levels: correlation coefficient (R), Nash-Sutcliffe (NSE), Mean Absolute Error (MAE), error mean (μ) and standard deviation (σ).

VS	n° data L_{tot}	R	NSE	MAE [m]	μ [m]	σ [m]
MM120	1739	0.81	0.39	0.88	0.73	0.81
MM820	1739	0.82	0.60	0.49	0.01	0.72
MMB272	1739	0.82	0.61	0.55	0.22	0.73
MM427	1739	0.82	0.49	0.70	0.51	0.74
MM22	1738	0.81	0.67	0.59	0.17	0.79
MM44	1738	0.81	0.67	0.58	0.11	0.79
MM629	1733	0.79	0.59	0.66	0.30	0.83
MM315	1734	0.79	0.58	0.67	0.32	0.83
MM775	1731	0.76	0.20	1.11	0.94	0.95
MMA272	17.31	0.73	-0.11	1.42	1.29	1.05
MM85	1731	0.73	0.36	0.90	0.59	0.98

4.3.2 Performance of different altimetry time series on model calibration

Table 4.4 summarizes results of the model calibrations and validations carried out using each altimetry time series at a time. It reports NSE, RMSE, MAE obtained at each satellite track considering the overall available datasets, which means m=L_{tot}. These performance statistics are compared with the ones obtained by repeating calibration considering in-situ water level elevation interpolated at the same location, and time of the satellite overpasses (in brackets). Δ-RMSE and Δ-MAE quantify the additional calibration errors due to the use of altimetry data instead of in-situ ones, while the last three columns report the results of the validation performed using satellite time series. Figure 4.7 reports the results of the calibration exercise performed considering altimetry time series of different length and randomly sampled from the original datasets (see eq. 4.2). Considering each altimetry product and VS at time, panels of Figure 4.7 show the calibrated roughness coefficient in relation to the number of observations, m, used for the calibration. The solid line indicates the Manning's coefficient that ensures the optimal NSE value among the 1000 calibrations performed with a given m value, while the grey area represents the range of variability of the roughness coefficients calibrated within Monte Carlo framework. The wider this area, the more the results of a calibration process depend on the altimetry record used for the calibration, with the risk of being significantly influenced by the range of water levels sensed during a specific period (e.g.,

mainly high or low flows).

Figure 4.8 provides an overview of the maximum error that we can expect when we use altimetry data for the calibration of a hydrodynamic model. The black line indicates the maximum MAE as function of m, thus the maximum error obtained considering all possible calibrated configurations obtained in Monte Carlo framework with a given data length (i.e., grey areas, Figure 4.7). The comparison with the same maximum MAE obtained calibrating the model with in-situ data (red line) provides a quantitative estimation of the additional error induced by satellite altimetry uncertainty. Figure 4.9 summarizes the findings of Figure 4.8 showing the temporal evolution of the performance of satellite altimetry for model calibration. The length of each box represents the temporal coverage of the mission, while the box height identifies the range of variability of the MAE obtained during the calibration considering the overall amount of available observations (see Table 4.4). In order to give a complete overview, Figure 4.9 also includes the results from the previous investigation using ERS-2 (Domeneghetti et al., 2015b). A similar calibration exercise over the Po river was done by Schneider et al. (2018) using CryoSat-2 series observed during the period 2010-2016. Their findings report an average RMSE (ME) of nearly 0.4 m (-0.18 m) for the SAR mode, with values ranging from 0.06 m (-0.05 m) up to 0.63 m (-0.23 m) (not shown in Figure 4.9).

Table 4.4: Calibration and validation results: Nash-Sutcliffe efficiency value (NSE), root mean square error (RMSE) and mean absolute error (MAE) obtained adopting the overall dataset of satellite and in-situ (in brackets) time series (m=L_{tot}).

	Calib. satellite (in-situ) data			**Δ = Sat - Situ**		**Valid. satellite time series**		
VS	**NSE** [-]	**RMSE** [m]	**MAE** [m]	**Δ-MAE** [m]	**Δ-RMSE** [m]	**NSE** [-]	**RMSE** [m]	**MAE** [m]
TP120	0.52 (0.92)	0.75 (0.32)	0.55 (0.27)	0.43	0.28	0.94	0.43	0.37
J2-120	0.93 (0.99)	0.44 (0.14)	0.31 (0.11)	0.30	0.20	0.97	0.30	0.24
J3-120	0.61 (0.93)	0.87 (0.39)	0.53 (0.24)	0.48	0.29	0.98	0.28	0.22
EX820	0.79 (0.99)	0.61 (0.10)	0.52 (0.08)	0.51	0.44	0.95	0.44	0.34
S3B272	0.93 (0.99)	0.24 (0.08)	0.18 (0.07)	0.16	0.11	0.62	1.10	1.04
S3A427	0.86 (0.97)	0.47 (0.20)	0.33 (0.14)	0.27	0.19	0.95	0.37	0.26
E22	0.74 (0.96)	0.83 (0.25)	0.39 (0.20)	0.58	0.19	0.94	0.42	0.33
SA44	-0.08 (0.96)	0.72 (0.23)	0.56 (0.20)	0.49	0.36	0.96	0.34	0.26
SA629	0.90 (0.97)	0.29 (0.17)	0.25 (0.16)	0.12	0.09	0.87	0.58	0.48
E315	0.92 (0.99)	0.46 (0.20)	0.29 (0.15)	0.26	0.14	0.85	0.63	0.52
EX775	-2.95 (0.91)	1.53 (0.22)	1.29 (0.20)	1.31	1.09	0.54	1.28	1.11
S3A272	0.91 (0.97)	0.43 (0.22)	0.31 (0.18)	0.21	0.13	0.70	1.02	0.89
TP85	-0.73 (0.80)	0.79 (0.39)	0.64 (0.31)	0.40	0.33	0.82	0.66	0.42
J2-85	0.93 (0.98)	0.45 (0.24)	0.32 (0.17)	0.21	0.15	0.78	0.76	0.52
J3-85	0.82 (0.92)	0.58 (0.34)	0.44 (0.24)	0.24	0.20	0.80	0.75	0.52

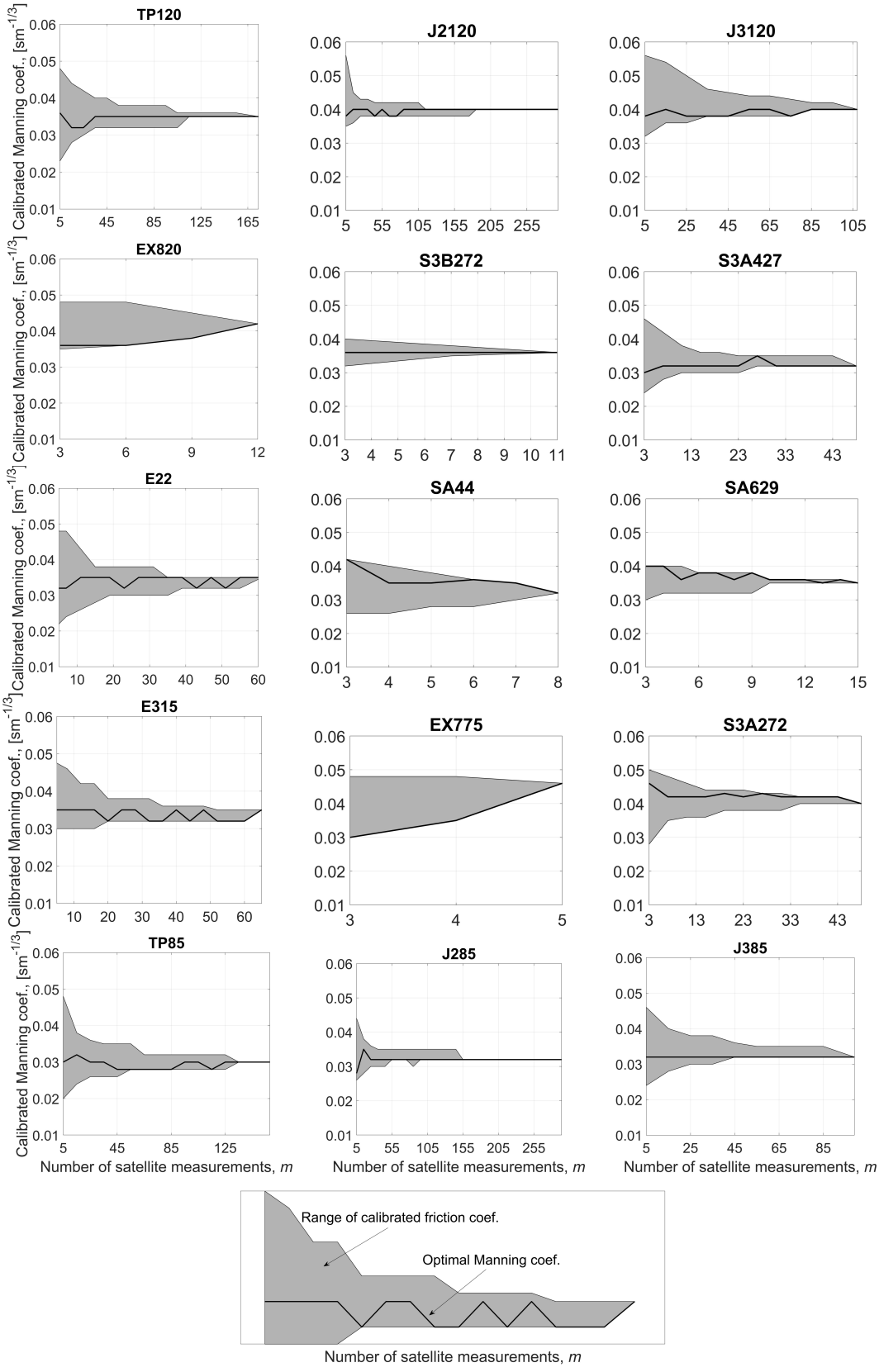

Figure 4.7: Calibration results for different altimetry series length: range of calibrated roughness coefficient (grey areas) and optimal Manning's value (black line) as a function of the number of satellite measurements, m.

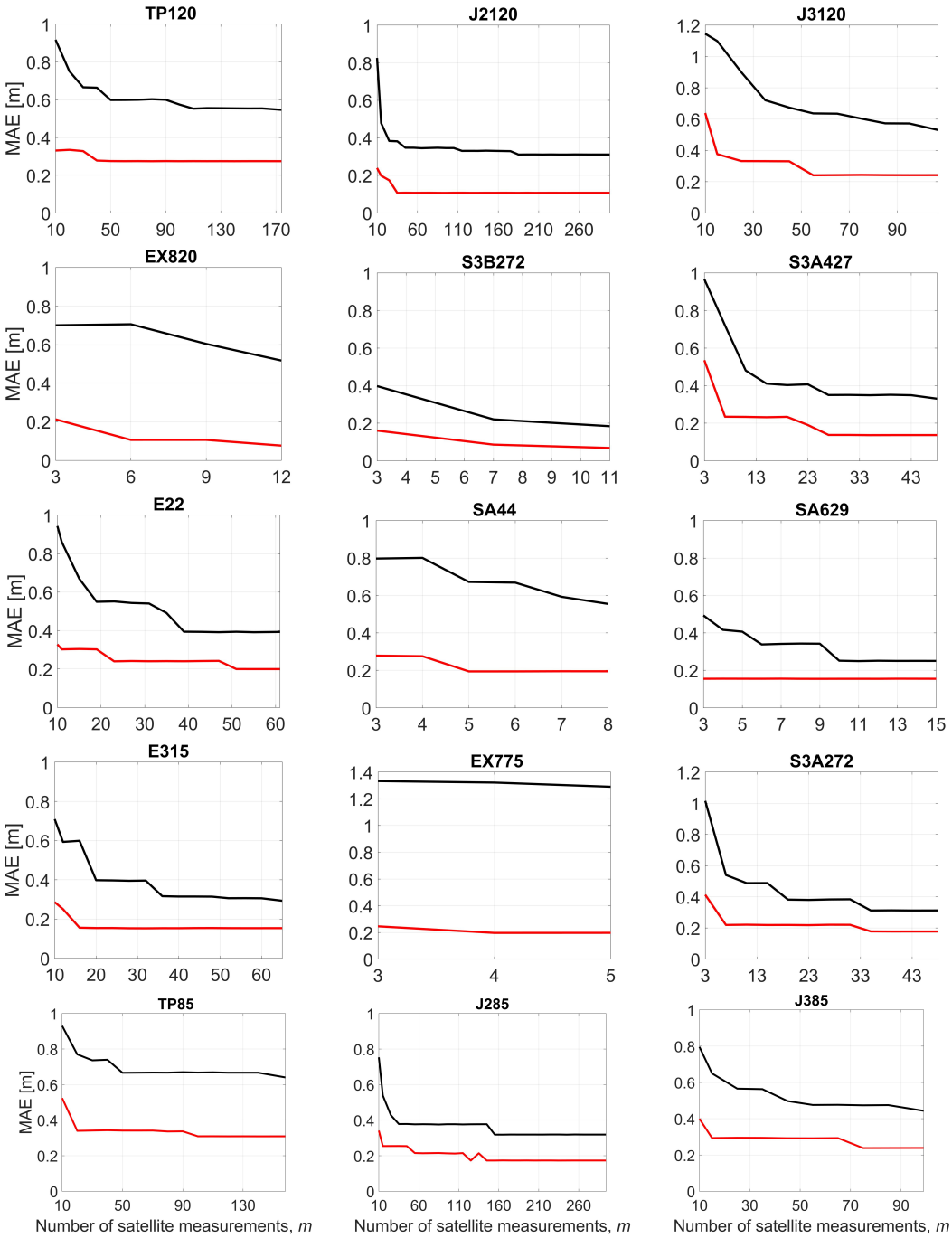

Figure 4.8: MAE obtained calibrating the numerical model with satellite altimetry data (black line) and in-situ water levels (red line) as a function of data length, m.

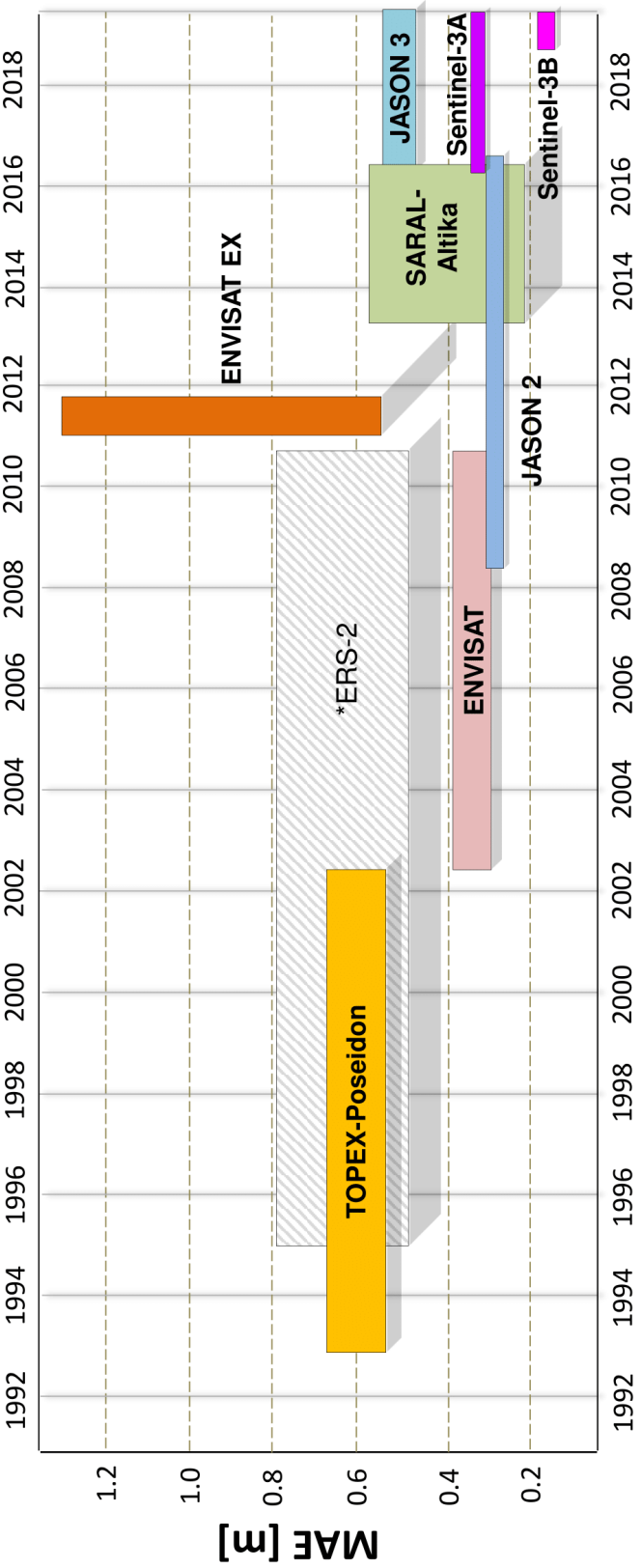

Figure 4.9: Synoptic view of the MAE of each satellite mission in time (*ERS-2 is a recall from a previous investigation): the vertical height of each box is defined as the range of the MAE obtained from the calibration at different VSs considering m=L_{tot}.

4.3.3 Performances of MM series on model calibration

Table 4.5 summarizes the results of the calibration (1995-2017) performed using MM series, as well as those obtained using in-situ water levels observed, in the same period, at the same day of the satellite overpasses. MM series are specified for each VS sensed along the study area, thus Table 4.5 has only 11 rows, according to the number of intersections between the Po river and the considered satellite orbits (VSs). As previously shown for the original satellite altimetry data, Figure 4.10 reports the results of the calibration carried out adopting MM altimetry series of different length and randomly sampled from the datasets used for calibration. Considering each VS at a time, panels in Figure 4.10 show the Manning coefficient calibrated in relation to the series length, m. The solid black line indicates the roughness coefficient that ensures the optimal NSE value among those tested for a given m value, while the grey area represents the range of variability of the calibrated coefficients. Even in this case, the width of the grey area is indicative of the sensibility of the calibration result to the length of the altimetry record used for the calibration. It is worth noting here that the temporal interval considered for calibration (1995-2017) is long enough to guarantee the achievement of a consolidated and stable calibration.

Figure 4.11 reports the maximum error obtained by calibrating the model with MM series: the black line indicates the maximum MAE as function of m, which is compared with the error obtained when calibrating the same model with an in-situ data record of the same length (red line).

Table 4.5: Calibration and validation results: Nash-Sutcliffe efficiency value (NSE), root mean square error (RMSE) and mean absolute error (MAE) obtained from the calibration process performed adopting MM and in-situ (in brackets) time series (m=L_{tot}).

	Calib. with MM (in-situ) series			**Δ = Sat - Situ**		**Valid. with MM series**		
VS	**NSE** [-]	**RMSE** [m]	**MAE** [m]	**Δ-MAE** [m]	**Δ-RMSE** [m]	**NS** [-]	**RMSE** [m]	**MAE** [m]
MM120	0.54 (0.95)	0.89 (0.28)	0.64 (0.21)	0.61	0.43	0.88	0.66	0.54
MM820	0.45 (0.95)	0.80 (0.29)	0.56 (0.22)	0.51	0.34	0.95	0.39	0.29
MMB272	0.51 (0.97)	0.80 (0.20)	0.56 (0.13)	0.60	0.43	0.97	0.28	0.15
MMA427	0.45 (0.97)	0.78 (0.18)	0.55 (0.13)	0.60	0.42	0.89	0.54	0.48
MM22	0.63 (0.92)	0.80 (0.33)	0.58 (0.24)	0.47	0.34	0.94	0.41	0.31
MM44	0.63 (0.93)	0.80 (0.33)	0.58 (0.24)	0.47	0.34	0.93	0.42	0.31
MM629	0.66 (0.89)	0.80 (0.41)	0.58 (0.26)	0.39	0.32	0.90	0.46	0.31
MM315	0.66 (0.95)	0.76 (0.28)	0.55 (0.19)	0.48	0.19	0.87	0.56	0.42
MM775	0.65 (0.79)	0.83 (0.58)	0.59 (0.37)	0.25	0.22	0.61	1.10	0.92
MMA272	0.65 (0.76)	0.89 (0.63)	0.64 (0.39)	0.26	0.25	0.53	1.18	1.12
MM85	0.66 (0.72)	0.79 (0.68)	0.57 (0.42)	0.11	0.15	0.70	0.91	0.67

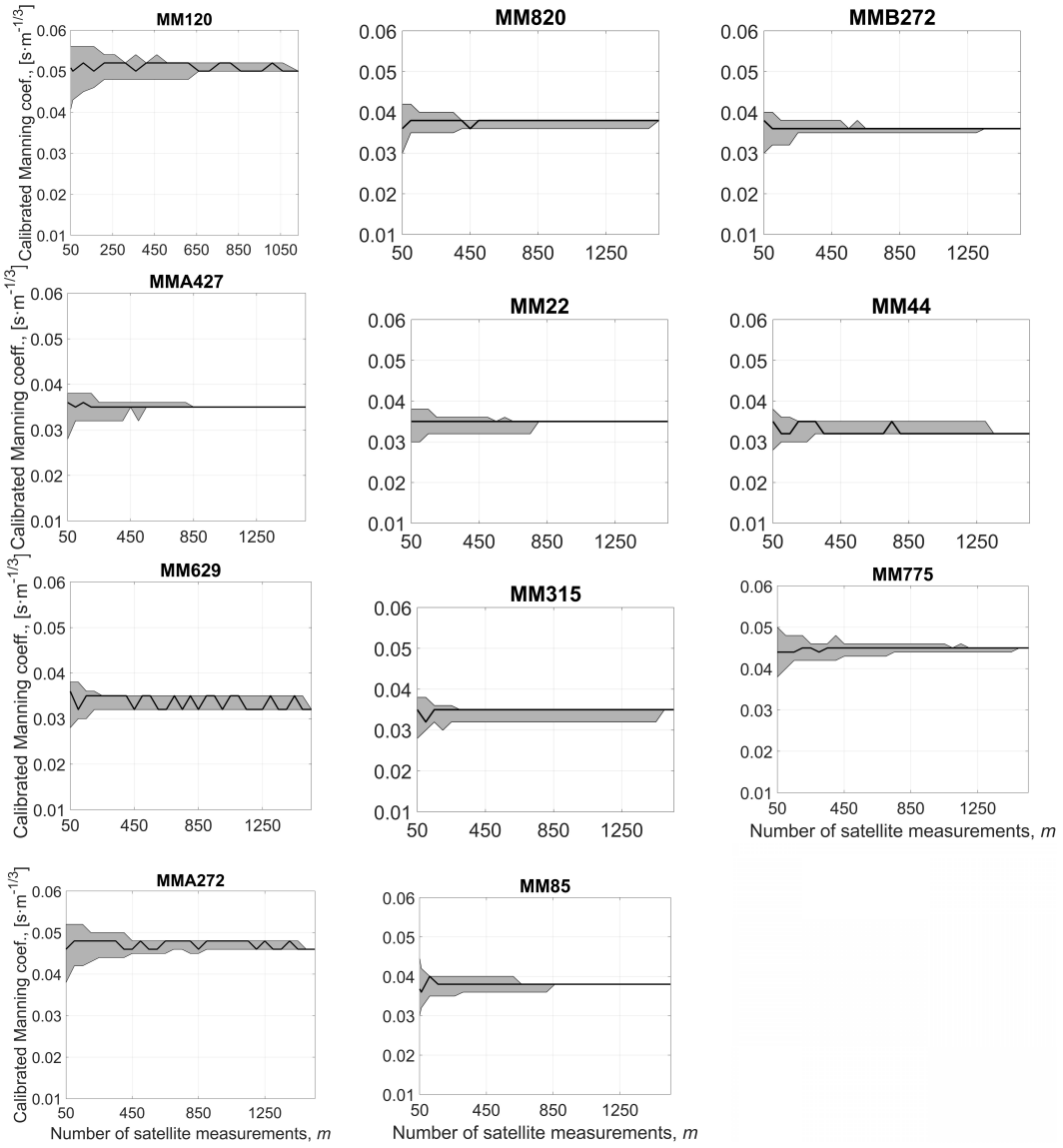

Figure 4.10: Calibration results for different MM series length: range of calibrated roughness coefficient (grey areas) and optimal Manning's value (black line) as a function of data length, m.

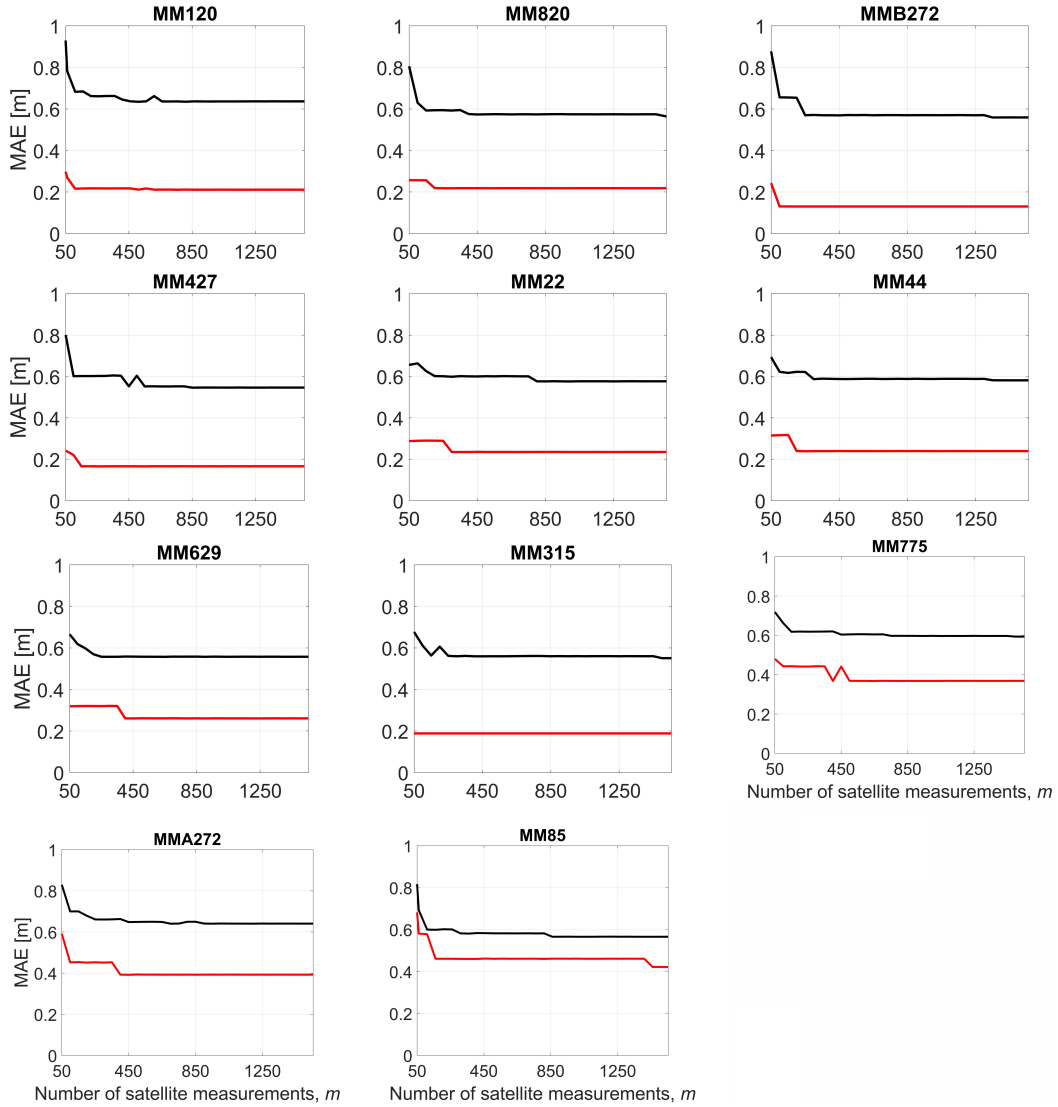

Figure 4.11: MAE obtained calibrating the numerical model with MM altimetry data (black line) and in-situ water levels (red line) as a function of data length, m.

4.3.4 Comparison of single and MM altimetry series

Table 4.6 presents the calibration results obtained using the MM time series. Results are compared with those achieved by calibrating the model with the original satellite altimetry available at the different VSs. Values reported in Table 4.6 refer to the case of considering the overall altimetry series length (m=L_{tot}). Last four columns report the calibration (validation) performances when considering the overall set of MM series along the Po river. Figures 4.12, 4.13, 4.14, 4.15, 4.16, 4.17 show the comparison between original satellite series and MM ones. Each figure represents one satellite mission, E22, J2-85, SA629, TP120, J3-85 and S3A-272 from Figure 4.12 to 4.17, respectively (S3B-272 is not shown since the limited amount of data). For each figure panel a) represents the number of measurements using MM series (grey columns) and unique sensor (black columns) considering different observation periods (temporal step equal to 20 months for E22 and SA44, 12 months for J2-85, J3-85 and TP120, 14 months for S3A-272). Panels b), c) and d) depict MAE, NSE variability and Manning's coefficient as a function of the number of available data, respectively.

Table 4.6: Calibration and validation results: optimal calibrated Manning's coefficient (n), and errors obtained adopting single and MM altimetry series ($m = L_{tot}$), as well as all MM series together (validation results are in brackets).

VS	Single Orig. n [$m^{-1/3}s$]	Sigle MM n [$m^{-1/3}s$]	Δ = MM - Orig. Δ n [$m^{-1/3}s$]	Δ-RMSE [m]	Δ-MAE [m]	Calib. (valid.) results - all MM series n [$m^{-1/3}s$]	NSE [-]	RMSE [m]	MAE [m]
MM-TP120	0.035	0.048	0.013	0.14	0.09		0.39	1.01	0.80
MM-J2120	0.040	0.048	0.008	0.45	0.33	0.048			
MM-J3120	0.040	0.048	0.008	0.02	0.11		(0.40)	(1.06)	(0.78)
MM-EX820	0.042	0.038	-0.004	0.19	0.04	0.045	0.53	0.81	0.55
							(0.80)	(0.60)	(0.41)
MM-B272	0.036	0.036	/	0.56	0.38	0.042	0.56	0.80	0.55
							(0.59)	(0.68)	(0.48)
MM-A427	0.032	0.035	0.003	0.31	0.22	0.04	0.58	0.80	0.55
							(0.78)	(0.63)	(0.44)
MM-E22	0.035	0.035	/	-0.003	0.19	0.036	0.62	0.80	0.56
							(0.75)	(0.70)	(0.50)
MM-SA44	0.032	0.032	/	0.08	0.02	0.033	0.61	0.81	0.57
							(0.75)	(0.69)	(0.50)
MM-SA629	0.035	0.032	-0.003	0.51	0.33	0.03	0.46	0.96	0.73
							(0.54)	(0.91)	(0.69)
MM-E315	0.035	0.035	/	0.30	0.26	0.03	0.44	0.98	0.76
							(0.53)	(0.93)	(0.70)
MM-EX775	0.046	0.045	-0.001	-0.70	-0.70	0.044	0.54	0.87	0.65
							(0.52)	(0.90)	(0.62)
MM-A272	0.040	0.046	0.006	0.46	0.33	0.046	0.26	1.17	0.95
							(0.11)	(1.22)	(0.96)
MM-TP85	0.030	0.038	0.008	/	-0.07		0.59	0.79	0.58
MM-J2-85	0.032	0.038	0.006	0.34	0.25	0.044			
MM-J3-85	0.032	0.038	0.006	0.21	0.13		(0.63)	(0.78)	(0.53)

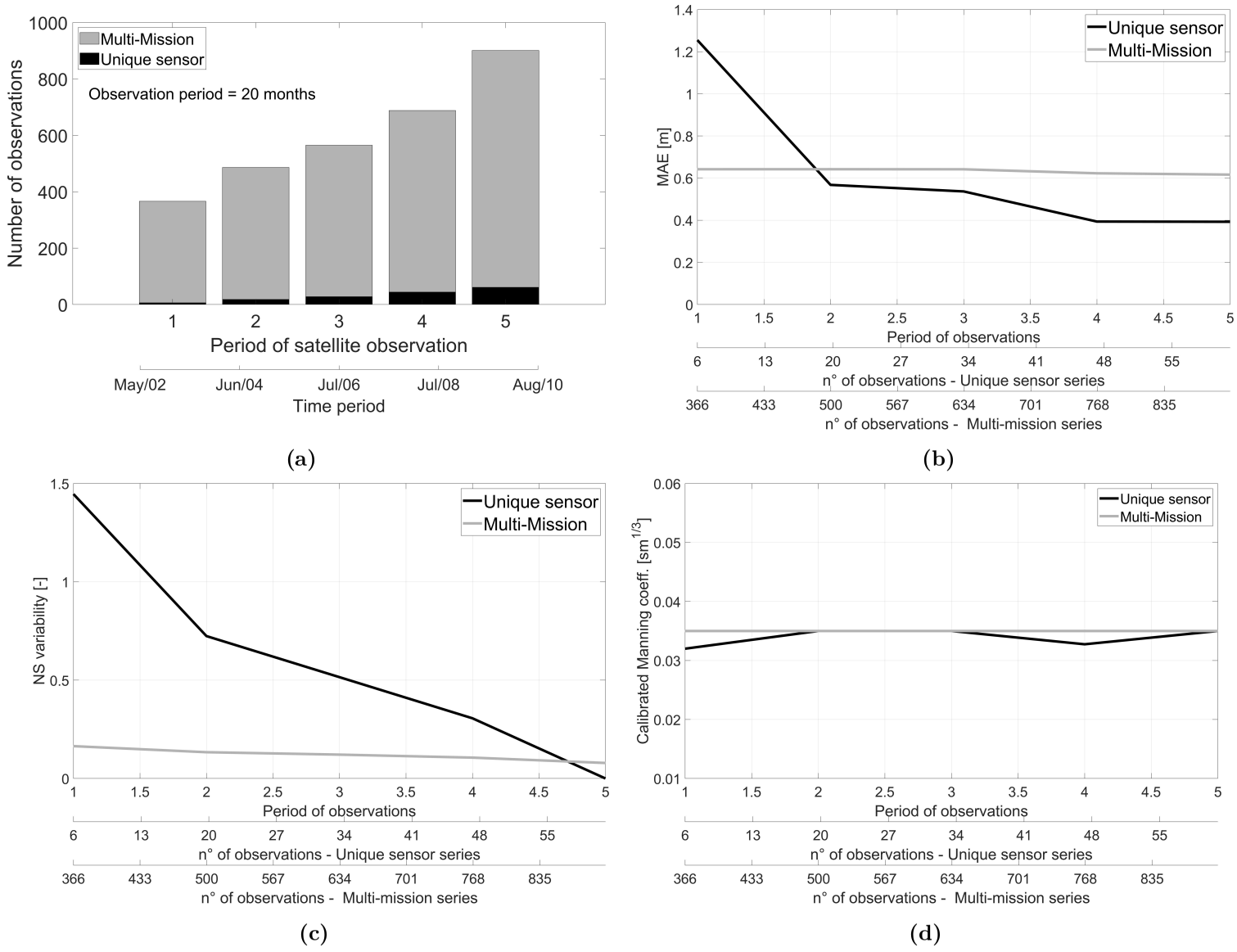

Figure 4.12: MM and E22: a) number of observations depending on the observation period; b) MAE, c) NS and d) Manning's coefficient as a function of the number of available observations for unique sensor (black line) and MM series (grey line).

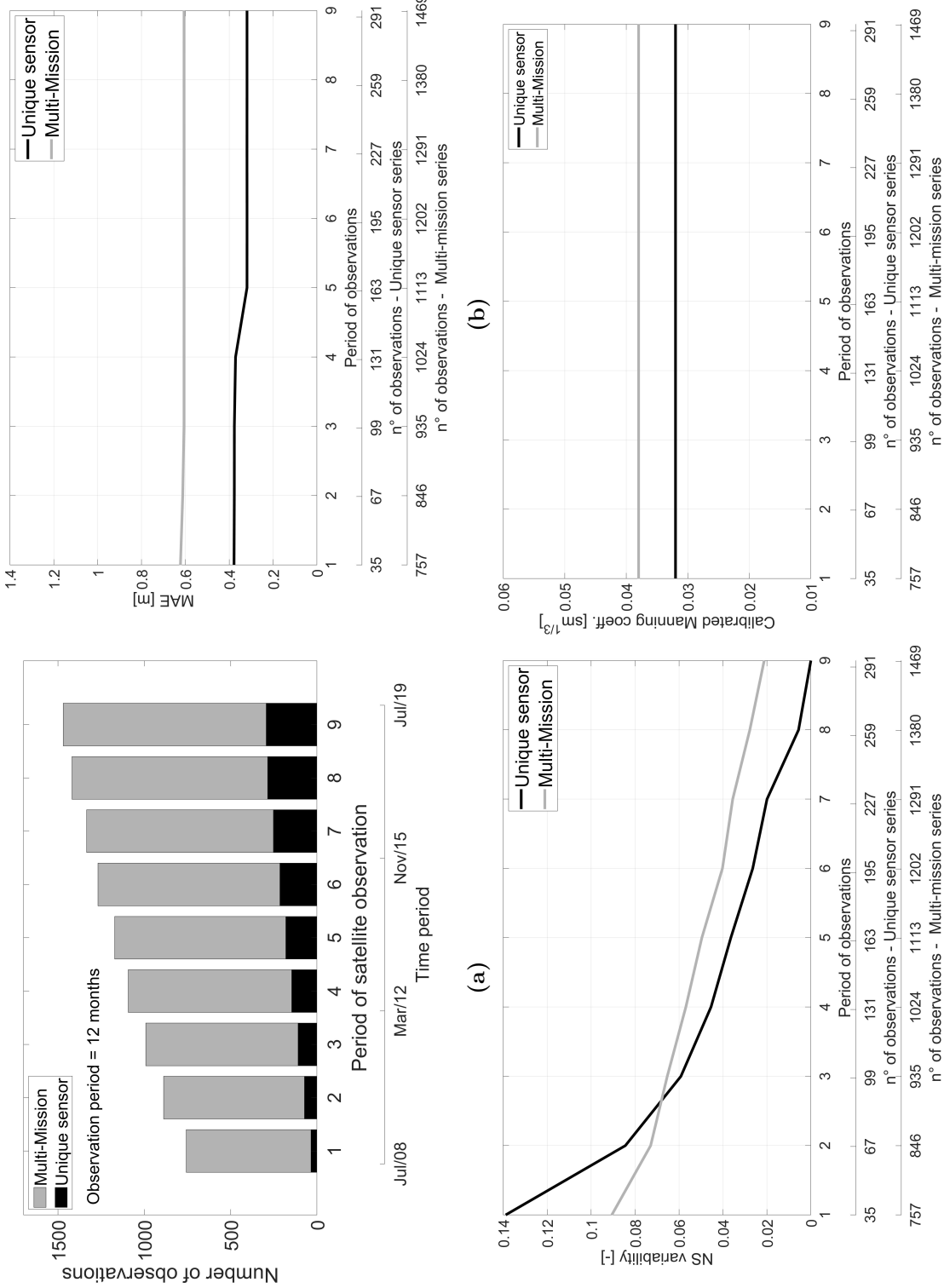

Figure 4.13: MM and J2-85: a) number of observations depending on the observation period; b) MAE, c) NS and d) Manning's coefficient as a function of the number of available observations for unique sensor (black line) and MM series (grey line).

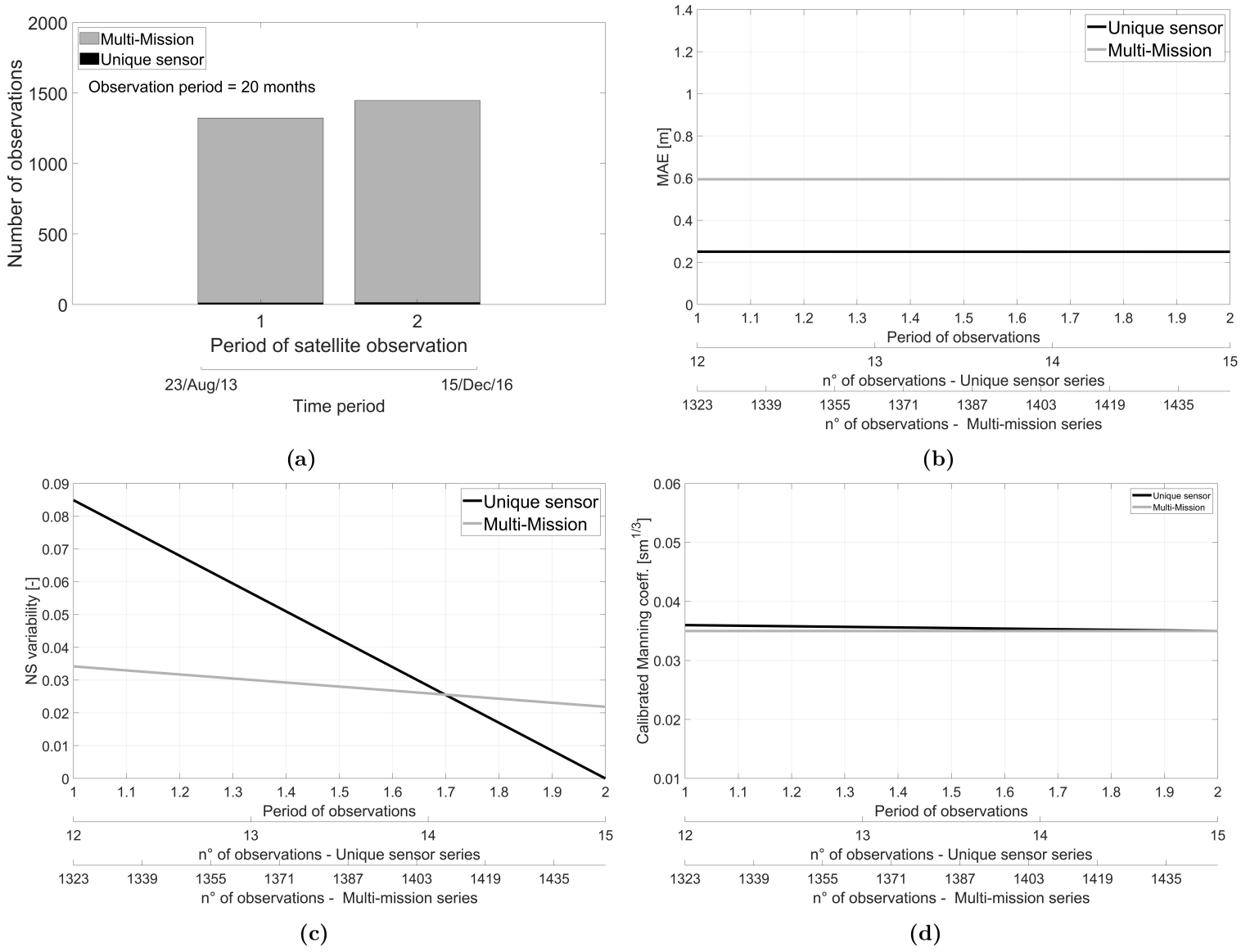

Figure 4.14: MM and SA629: a) number of observations depending on the observation period; b) MAE, c) NS and d) Manning's coefficient as a function of the number of available observations for unique sensor (black line) and MM series (grey line).

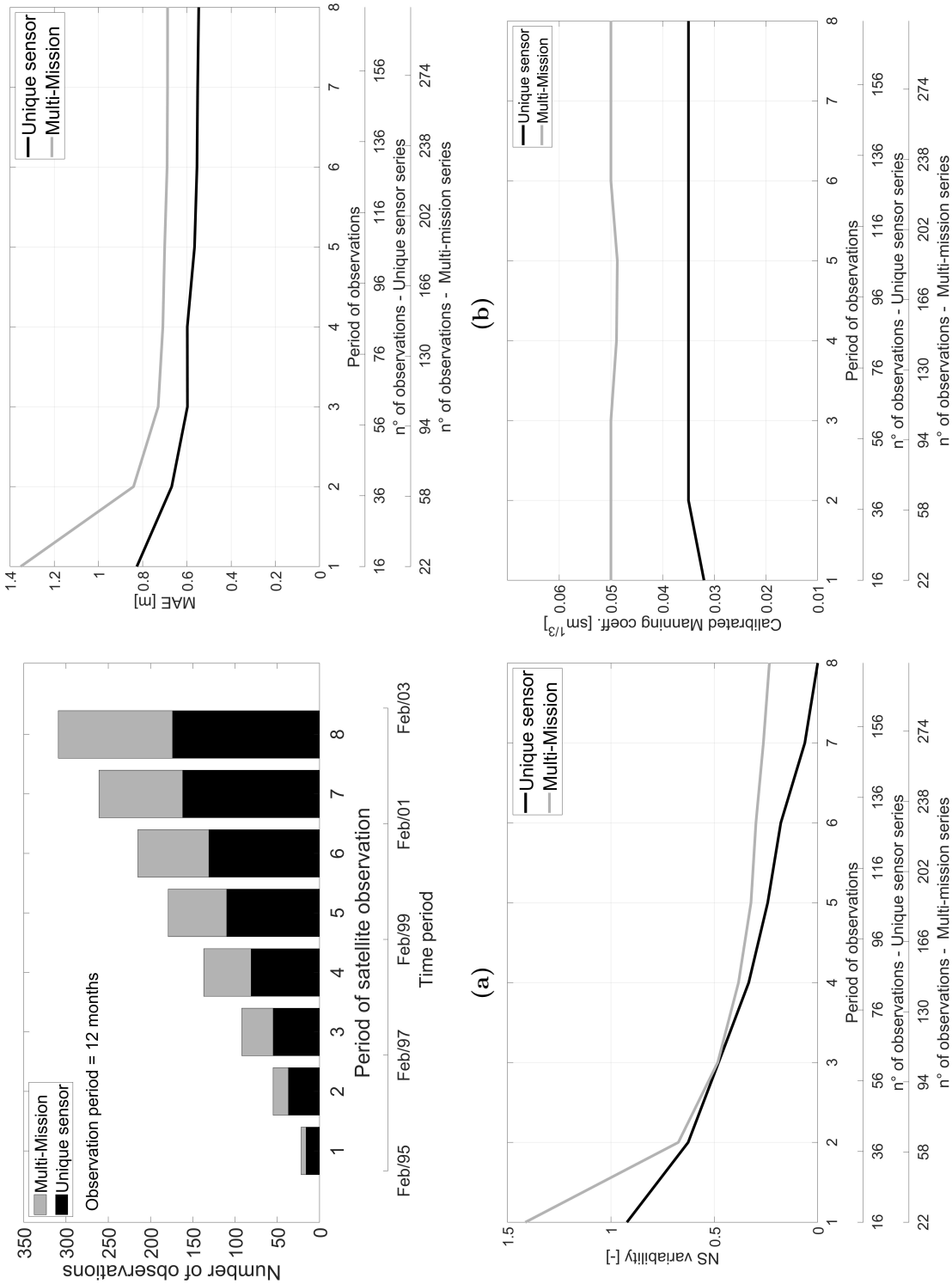

Figure 4.15: MM and TP120: a) number of observations depending on the observation period; b) MAE, c) NSE and d) Manning's coefficient as a function of the number of available observations for unique sensor (black line) and MM series (grey line).

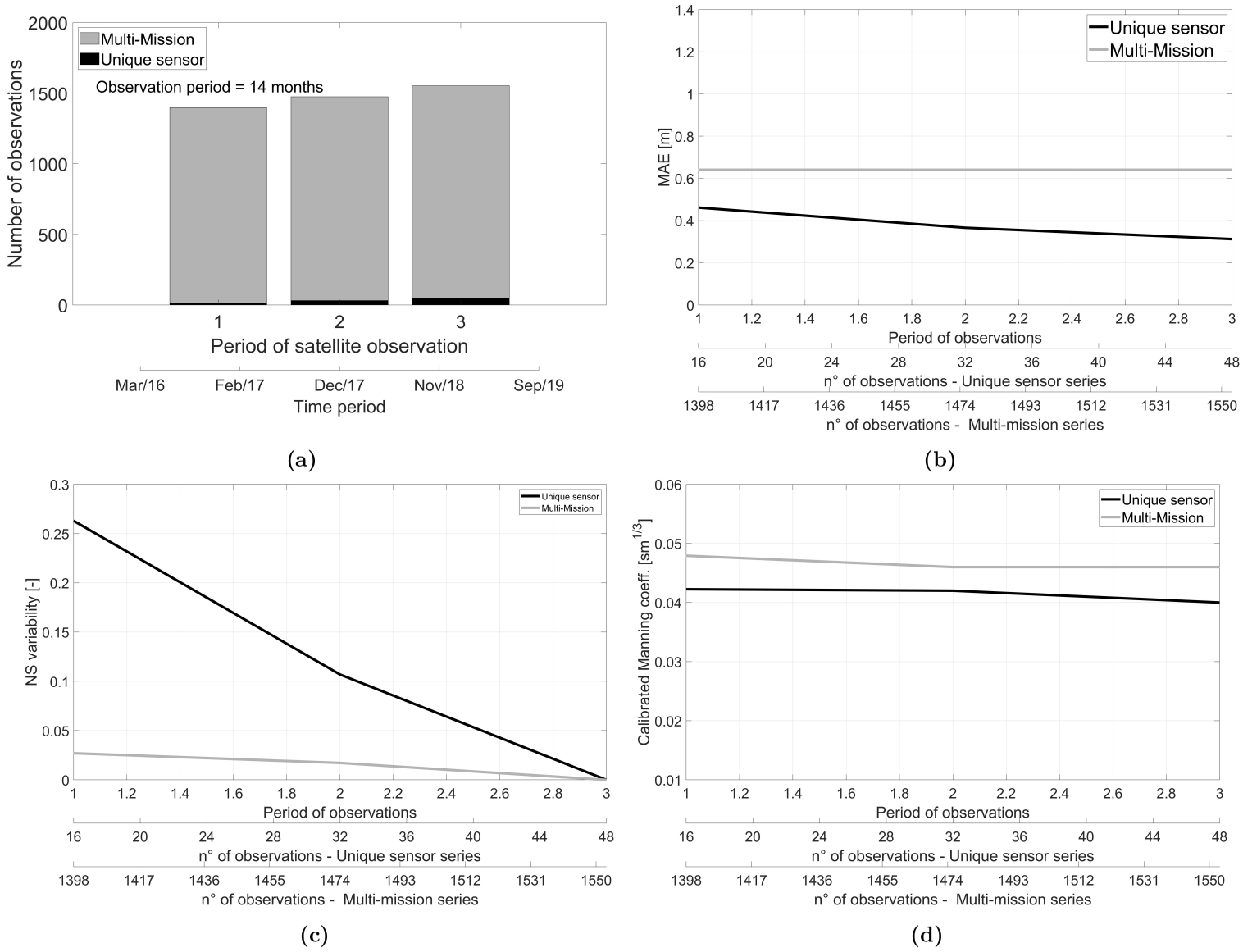

Figure 4.16: MM and S3A-272: a) number of observations depending on the observation period; b) MAE, c) NSE and d) Manning's coefficient as a function of the number of available observations for unique sensor (black line) and MM series (grey line).

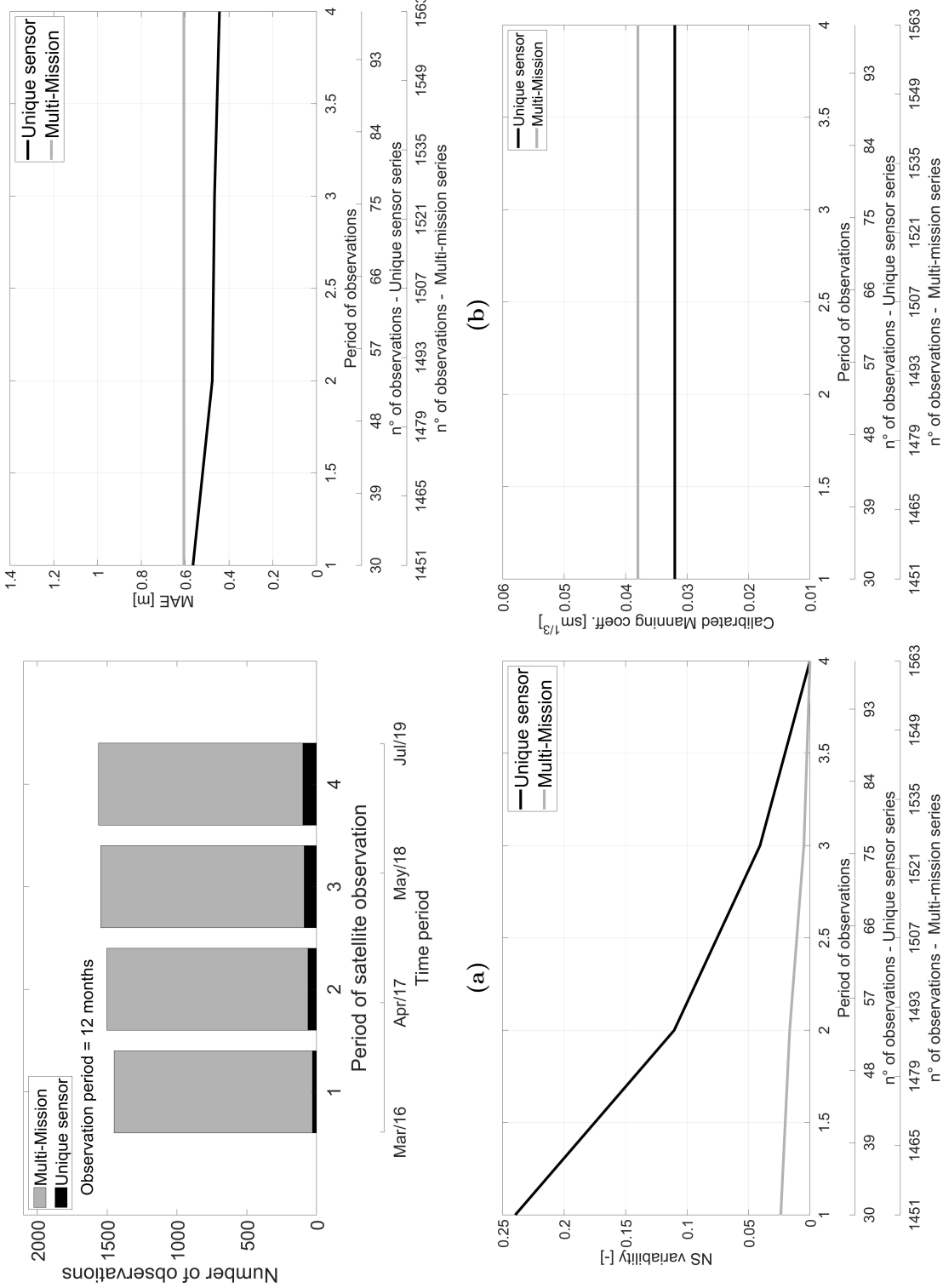

Figure 4.17: MM and J3-85: a) number of observations depending on the observation period; b) MAE, c) NSE and d) Manning's coefficient as a function of the number of available observations for unique sensor (black line) and MM series (grey line).

4.4 Discussion

4.4.1 Accuracy of altimetry products

Table 4.2 summarizes the comparison between satellite and original altimetry data. Excluding EX775, which has a very limited number of observations, all the altimetry series show quite high R values, which are always larger than 0.6 and generally improves moving from historical missions to the most recent ones. Similarly, NSE values are in general positive, with the few exceptions of EX775 and TP85. In general, J2 series outperform all other missions providing a mean error, μ, of about 20 cm and the lowest values of standard deviation ($\mu = 0.38$ cm in the worst case). Despite the limited amount of observations, S3B is the only time series having a lower mean error ($\mu = 0$), while S3A series show performance in line with those of J2 and S3B, unless irregular among the available VSs. J3 provides μ values comparable to those of J2, but higher standard deviations, σ. A possible justification can be due to the characteristics of J3 series, which appear shorter than those of J2 (nearly 1/3 in length; see Table 4.2) and characterized by a higher frequency of low-flow conditions. This latter aspect is evident in Figure 4.3, where J3 covers a period of time (2016-on) during which water levels are on average lower (meaning low flow period) than what observed by J2 (yellow lines). This aspect may play a significant role when considering possible hooking effect (or "off-nadir" effect, Schwatke et al., 2015), which is expected to be more relevant in case of smaller water extent. In addition to this, after a closer look at J3 data and correspondent observed level, the performance of J3 at VS 120 appears strongly influenced by few significant errors observed during a short period (beginning of 2018), during which the altimeter sensed water level considerably higher than the observed ones. Those errors, since the limited extent of J3 series, heavily affect the statistics, which would have been in line with those of J2 otherwise.
SA series ensure high correlation values, while MAE values are worse than those from the older mission E. This might be due to the limited length of the series (8 and 15 observations in total at the two available VSs). In contrast, despite the number of available observations, TP provides the worst results, with low NSE and high MAE values. The mean error values, μ, indicate a general overestimation of the satellite series ($\mu > 0$) with the only exception of TP120 that shows a negative bias. Finally, referring to ERS-2 data, Domeneghetti et al. (2015b) identify MAE values in the order of 0.7 m, with μ and σ up to 0.64 cm and 0.84 cm, respectively, at two VS along the Po river.
Table 4.3 shows the results of the same comparison performed with MM series. Results highlight a uniform performance in terms of R (0.80). NSE values are in general positive, even if always lower than 0.66. In general, performance indexes appear more homogeneous

along the study area, which is somehow expected considering the way the MM series are defined along the river.
Looking at the spatial distribution of the error, the analysis performed does not enable the identification of a specific relationship among error magnitude and river morphology, such as river width or river orientation. However, it is worth noting that in general the performances obtained considering the MM series at a given location are always lower than those obtained considering the original altimetry series, with the only exception of few VSs where the performances of the altimetry products were not convincing, perhaps due to their limited length (e.g., VS 775). In such a case, MM series is more capable to reproduce the observed water level dynamics.

4.4.2 Values of satellite altimetry and effects of time series length on model calibration

The results of the calibration performed using satellite altimetry shed some light on the potential of different products for modelling applications. In particular, the influence of the number of observations on the variability of the results varies in relation to the satellite product.
Assuming that a calibration result should be considered reliable when the variability of the roughness coefficient is very limited (i.e., ± 0.005 s $\cdot$ m$^{-1/3}$ in terms of Manning's coefficient), this condition is reached in case of considering a number of observations that varies from one mission to another. Looking at Figure 4.7, this target is reached for E in case of using more than nearly 35 observations, which means nearly 3.5 years of observation considering its revisit time (35 days). Similar results have been obtained considering ERS-2 series (Domeneghetti et al., 2015b). The lengths of required series become smaller in case of TP (revisit time equal to 10 days), which ensures reliable performance with 50 observations, recorded on average in 1.5 years. Better performances are obtained in case of J2 series, for which the same performance is obtained calibrating the model with nearly 30 observations (less than 1 year of record considering its temporal resolution). The same number of observations is required by S3A, although its lower repeat period extends the time series up to more than 2 years. Similarly, 30 observations are needed for J3-85, while nearly 60 (slightly more than 1.5 year) are required for the J3-120. Again, this latter difference can be justified by the errors noticed for J3-120 series and previously described. Regarding the satellite series EX, the limited number of available observations prevents us from drawing general conclusions. The same holds for SA44 (8 measurements in total). Despite the limited amount of data, the calibration results with S3B272 and

SA629 are good: the calibration appears reliable already with a limited number of data, nearly 10, which means a period of observation of approximately 1 year and less than 1 year for SA and S3B, respectively, considering their repeat periods. In addition, this seems to confirm the value of SA mission, which is the only one operating at Ka band among those considered. As a matter of fact, although considering wider inland water bodies and rivers (e.g. nearly 5 km) Schwatke et al. (2015) proved the higher potential of a Ka-band instrument compared to the typical Ku-band sensors, thus offering promising expectation from future satellite missions that envisage the adoption of Ka-band altimeter (e.g. SWOT mission).

The evolution of the calibration performance in relation to m, number of observations, is clearly depicted by Figure 4.8, where the maximum MAE obtained during the calibrations typically decreases with extensive series. Looking at the errors obtained using in-situ data (red lines), the maximum MAE reaches the minimum value after a limited amount of data, assuming errors that are almost uniform along the study area: the optimal error varies in the range ∼10-30 cm (see also Table 4.3). The evolution of the black lines (altimetry data) confirms previous findings on satellite potential. S3A, S3B, J3, J2 and TP products ensure the fastest achievement of the minimum error. However, regarding the distance between red and black lines, which can be considered as a measure of the error introduced in the model calibration when using altimetry data instead of in-situ, E series provide performances comparable to that of J2 (see Table 4.4). On the contrary, TP series, despite being more frequent, introduce larger errors: nearly double that of E or J2.

Finally, it is worth highlighting the performance of S3B272, which ensures the lowest error among all considered satellite series. These results are clearly summarized in Figure 4.9, which shows the temporal distribution of the satellite series together with their calibration performances. What is evident is that, with the only exception of EX and caution on considering J3, the error and its variability are generally decreasing in time, showing a constant improvement in satellite capacity to remotely observe water elevation. This potential of altimetry time series is also confirmed by the validation results (Table 4.4), for which the lowest NSE is equal to 0.54. In general, if not even better, NSE values are comparable to the ones obtained during the calibration phase. Only in few cases the validation provided accuracy significantly worse than the one achieved during the calibration (e.g., S3B272, S3A272).

Findings concerning SARAL/Altika might be misleading since the poor performance at SA44, which is responsible for the significant size of the error box of Figure 4.9. As a matter of fact, the additional error introduced at SA629 is equal to 0.09 m, which is the

lowest of all the series. Future analysis with longer SA series will reveal the real potential of this satellite product for model calibration.
Concerning the use of MM series on model calibration, in the light of the higher number of observations combined by MM series, the calibration easily converges to the final configuration (Figures 4.10 and 4.11). However, errors introduced using such series are higher than those associated with traditional series: Δ-RMSE and Δ-MAE are on average equal to 0.53 m and 0.38 m, respectively (Table 4.5). As expected, MM performances in terms of model calibration do not vary from one location to another being the result of a spatial and temporal combination of all available satellite dataset. However, it is also worth noting that using high frequency water level series reduces the calibration accuracy (NSE) also in case of referring to extended series of in-situ data (see comparison of NSE values for in-situ data in Tables 4.4 and 4.5). Since the calibration considers a constant Manning's coefficient, we argue that this loss of efficiency might be due to the consideration of a higher variability of river flow conditions, which include both low and peak flow regime. As a matter of fact, a model calibrated referring to medium-to-large flow conditions, that are those most frequent in the river, might have poor performance when used to reproduce low flow scenarios (see e.g. Moramarco and Singh, 2010; Domeneghetti et al., 2012). Validation results confirm the potential of MM time series for model calibration, reporting performances in line with those achieved calibrating the model using in-situ data for the same time period (values in brackets in Table 4.5).
Leaving aside specific performances of different single mission products, the calibrated roughness coefficients obtained considering one time series at time (first two columns of Table 4.6) appear in line with values obtained from previous studies performed over the study area, which shown a general decreasing trend moving downstream (reference values are 0.004-0.042-0.025 $sm^{-1/3}$ for the upper, middle e lower river portion, respectively; see Domeneghetti, 2016). Similar behaviour is also observed adopting MM series, with variation on roughness values not particularly significant.

4.4.3 Potential and limits of MM altimetry series for model calibration

Using MM series always entails an additional error: Δ-RMSE and Δ-MAE are always positive, with values up to 0.56 m and 0.38 m, respectively. The only exception is represented by MM-EX775, which is due to the poor performance of EX series at that location. Thus, in case of considering the overall altimetry series length ($m = L_{tot}$; which varies in relation to the series), the use of a single MM series for model calibration does

not provide benefits and is not recommended.
However, results presented in Figures 4.12-4.17 provide more insights: NSE variability (panel c)) associated to MM (grey lines) is always lower than the one obtained with the original series (black lines), thus providing more stable calibration even for very short calibration periods. This is particularly significant in case of altimetry series with limited observation frequency (i.e., 35 days, such as E and SA), for which the calibration immediately converges to the real Manning coefficient (black and grey lines overlap in panels d)), even using data observed within 1 observation period (i.e., 20 months; see e.g., Figure 4.12 and 4.14). On the contrary, differences are much larger and not negligible in case of satellite products characterized by higher temporal observation frequency (i.e., J2, J3 and TP). This might be explained by considering that, in case of high frequency series (i.e., those with revisit time of 10 days), the MM generation process further enhances the temporal coverage of the remote series, but it introduces errors larger than those associated with the original satellite series, which are still in any case frequent enough to provide a reliable calibration.
When using all MM series together, some differences emerged in terms of calibrated Manning's coefficients, which are not always in agreement with those obtained considering one VS at time (Table 4.6). This is due to the mutual interaction of the calibrating river cross-sections (VSs) that requires local modification of the friction values to deal with opposing biases. However, apart for few exceptions (MM120 and MMA272), the use of all MM series together provides performances along the entire river in line with those ensured by adopting one MM series at time, which is promising in assuring a proper simulation of flowing dynamics over long river stretch.
A possible strategy towards an improvement of MM reliability and accuracy, at the expense of some temporal frequency reduction, could be the adoption of only best performing single missions (e.g., E, J2, J3 and SA). Preliminary trials on this matter did not provide satisfying results, but future work will further investigate in this direction. In this context, future analysis could also consider the opportunity to include other recent altimetry products that, although characterized by long repeat cycles, have high accuracy on water level measurement. This is the case for example of IceSat-2 (ATLAS altimetry; available from December 2018) that can ensure high accuracy on water elevation sensing but has a repeat period of 91 days (see e.g., Yuan et al., 2020). Shifting in space such information could further sustain satellite products exploitation for inland river monitoring.

4.5 Concluding remarks

This study provides additional insights regarding the potential of satellite altimetry sensors for hydraulic applications. Although not aspiring at providing an evaluation and comparison of altimetry missions in absolute terms (a wider spectrum of rivers and flowing conditions would have been necessary), this work offers a comprehensive and cross-missions view of the potential of such products, together with MM series, which have been tested for hydraulic model calibration. To this end we referred to a reach of nearly 140 km of the Po river for which we implemented a quasi-2D hydraulic model based on detailed topographic data.

In general, altimetry time series properly reproduce observed water level time series, showing correlation coefficients (R) always larger than 0.6 in case of single missions. Despite limited to one VS, S3B (Sentinel-3B) ensures the lowest error (η=0). J2 (Jason 2) shows high accuracy (mean error equal to 20 cm), followed by S3A (Sentinel-3A), J3 (Jason 3) and Envisat (E). Even though the limited extent of the derived time series, SA (SARAL/Altika) shows promising performances with high R values (higher than 0.9). On the contrary and despite the high number of observations, TP (TOPEX/Poseidon) series do not ensure reliable estimation of water levels.

MM series ensures a uniform behaviour along the study area (R is nearly constant and equal to 0.80), however, their performances at a given location are always lower than those obtained considering the original altimetry series (see Tables 4.2 and 4.3).

Results of the model calibration depict a general temporal improvement of satellite performances moving from the oldest to more recent missions, with the only exception of EX series (see Figure 4.8). The lower additional error induced by the use of remote sensing data on model calibration (Δ-MAE) is limited to nearly 20 cm in case of using J2 and E series, while it is larger (up to 30÷40 cm) in case of other series (up to 60 cm in case of ERS-2 series; Domeneghetti et al., 2015b). J2 series ensure trustworthiness and reliability on the calibration process with the lower temporal observation extent: lower than 1 year of data ($\sim$ 30 observations), followed by J3 and S3A that reach the same reliability after 1.5, 1.6 and 2.2 years, respectively (i.e., 50, 60 and 30 observations, respectively). For a similar performance, E requires nearly 3.5 years of data (i.e, 35 observations). Using ERS-2 data would require a series extent up to 4.5 years (nearly 50 observations considering a satellite revisit time of 35 days). Unless limited in time, results show SA and S3B time series potential in achieving reliable calibration using only few observations (e.g., nearly 10).

The use of MM series for model calibration has provided errors higher than those obtained

using original satellite series in case of considering their overall length: additional errors are equal to 0.56 m and 0.38 m in terms of Δ-RMSE and Δ-MAE, respectively.
However, the comparison of MM and original series' performances in relation to the number of available observations depicts the potential of MM series, which are able to ensure calibrations more reliable than those obtained in case of altimetry series provided by low frequency satellites (i.e., E, SA) that cover very short period (e.g. 1÷2 observation period; 20-40 months). In such circumstances MM series offer calibration performances (i.e., reliable estimation of the friction coefficient and lower uncertainty) higher than those ensured with the original series. However, if satellite sensors with higher temporal observation frequency are available (i.e., J2 and J3), the use of original series, even though limited in terms of observations, appears to be the best option. That said, MM series ensure a higher spatial coverage of the river, which could be significant when referring to long river stretch and single altimetry missions characterized by long inter-track distances.

Part 2

CHAPTER 1

A conceptual model for basin with seasonally variable catchment size

A strong wind rose and soon a violent hurricane broke out. The castle well began to throw out water and soon the entire castle, the fields, the meadows... everything was covered by water. The hurricane ceased and instead of the castle and meadows, there was a lake, the lake of Monate.

Costanzo Ranci
"The lean shore. Legends of Maggiore Lake", 1931

This Chapter contains:

1.1 Introduction

In 1987 the World Commission on Environment and Development (WCED) in the paper *Our Common Future* introduced, for the first time, the concept of *Sustainable Development*, defined as "the development that meets the needs of the present without compromising the ability of future generations to meet their own needs". Sustainability goals (`https://sdgs.un.org/goals`) address the global challenges, including poverty, inequality, climate change, environmental degradation, peace and justice. The simultaneity between the human development and the natural systems, without undermining the integrity and stability of the environment, has to be guaranteed.
In particular, the famous American environmentalist and activist Paul Hawken defines the environmental sustainability as the stabilization of the currently disruptive relationship between human culture and the living world, avoiding the destruction of earth's resources faster than they can be regenerated and replenished.
The concept of Sustainable Development is one of the fundamental principles at the base of legislative decree of 3 April 2006, n.152, the Italian reference legislation in the environmental field. It was the first step of a series of legislations in environmental conservation and protection, from the law 68/2015, representing the long-awaited sanctioning response to combat criminal phenomena (i.e., environmental pollution, environmental disaster, Traffic and abandonment of highly radioactive material) that see the environment as a legal asset to be protected, to the law 221/2015 with the concepts of Green Public Procurement (GPP) and Minimum Environmental Criteria (MEC). The main instrument for the environmental conservation is the monitoring activity, aimed to assess the consequences of natural resource management actions to man and the environment. Respecting the competences of the Regions, the goal of National System (law 132/2006) is the monitoring of environmental resources and their evolution in qualitative and quantitative terms, using monitoring networks and modelling tools.
In this context, our research focuses on the basin of Monate Lake, an example of environmental area of inestimable value for the purity of the water, the excellent state of the banks and the strategic position for tourism, fishing and agricultural crops. The conformation of its shores and their prevailing privatization helped to prevent the lake from being surrounded by industrial settlements and mass tourism, thus preserving the quality of the water. Thanks also to an ordinance, under which motor navigation is forbidden, the lake is still one of the very few pre-alpine basins of glacial origin that can be bathed on the entire surface (Montanari and Castellarin, 2012). Moreover, the lake has no tributaries with the exception of the Roggia Riale stream and only one emissary, the Acquanegra

creek. Previous analysis (e.g. Barnaba, 1987) have widely investigated the water balance of the lake basin, hypothesising the presence of a groundwater basin.

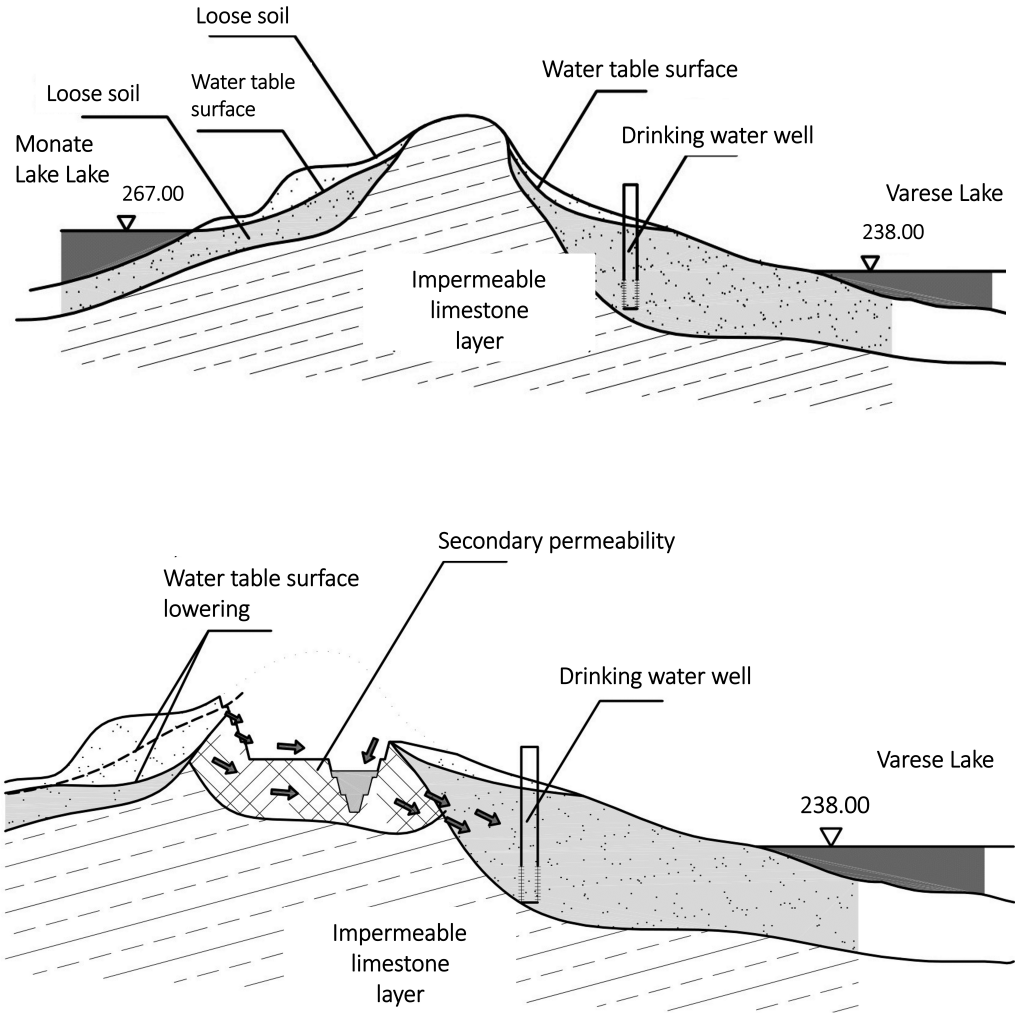

Figure 1.1: Geologic transect before (upper panel) and after (bottom panel) the quarry activities (Rabuffetti, 2012).

For all these considerations, the Monate Lake hydrology is the subject of considerable scientific interest. In order to evaluate the impact of quarry cultivation in Cava Faraona on the Monate Lake water balance, in 2012 an environmental monitoring plan was drawn up in agreement with the Municipal Administration of Travedona Monate and the company Holcim SpA. It aims to monitor several environmental variables, ranging from air quality, noise and vibrations to climatic and hydrogeological ones. The collected data, as well as the environmental monitoring plan documentation, are freely available on the Travedona Monate Municipality website (`http://www.comune.travedonamonate.va.it`). The Travedona Monate Municipality entrusted the Department of Civil, Chemical, Environmental and Materials Engineering (DICAM) of the University of Bologna with the

role of supervising the environmental monitoring. In particular, Cava Faraona and Cava Santa Maria, located between Travedona Monate and Ternate Municipalities, have been subject to an extension proposal, involving a further part of the lake catchment area. In accordance with Rabuffetti (2012), a significant correlation among the planned cultivation activities and the Monate Lake and wells waters can not be excluded. The goal is ascertaining any environmental criticalities and guaranteeing special precautions regarding the sustainability of an important operation conducted on its territory and more generally in the interest of its fellow citizens. Figure 1.1 illustrates geologic transects before (upper panel) and after (bottom panel) the quarry activities for estimating the effects of the quarry activities on the environment. After the quarry extension (bottom panel Figure 1.1), Rabuffetti (2012) have hypothesized depleted water tables towards Monate Lake and the filtrations to Varese Lake due to secondary permeability formation.
Exploiting the climatic, hydraulic and hydrological information (i.e., precipitation, lake water levels), a simple predictive model has been implemented, suitable for the basin peculiarities representations of the Monate Lake. Thus, the first goal of this research activity is:

To develop a parsimonious conceptual rainfall-runoff model suitable for predicting the hydrological unusual behaviour of the Lake of Monate.

The second part of this work is dedicated to the extension of the proposed model in order to represent a groundwater basin with variable catchment area. Thus, the second object is:

To address a simplified modelling of the seasonal dynamics of the groundwater catchment of the Lake of Monate.

Given this general framework, the Part 2 of this dissertation is structured as follows. The Section 1.2 presents the study area and the monitoring network, illustrating in details the instruments and data useful for the analysis. The Section 1.3 focuses on the hydrological model used and its adaptation to the study case, as well as, the proposed modifications to the original model. The Section 1.4 is dedicated to the presentation of calibration and validation phases of the model, followed by the results discussion (Section 1.5).

1.2 Study area and monitoring network

1.2.1 Study area

The Monate Lake is located East of Maggiore Lake in the Province of Varese (Italy) at 266 m a.s.l. with an area of 2.58 km^2 and 7.8 km of coasts. The mean depth is about 18 m, reaching 35 meters in some locations. The lake is mainly feed by spring origin waters, has no tributaries with the exception of the Roggia Riale stream. The only emissary is the Acquanegra creek, originating from the lake shores and flowing into the Maggiore Lake, of an overall length of 11 km. Its outflow is about 3.45 Mm^3 per year.

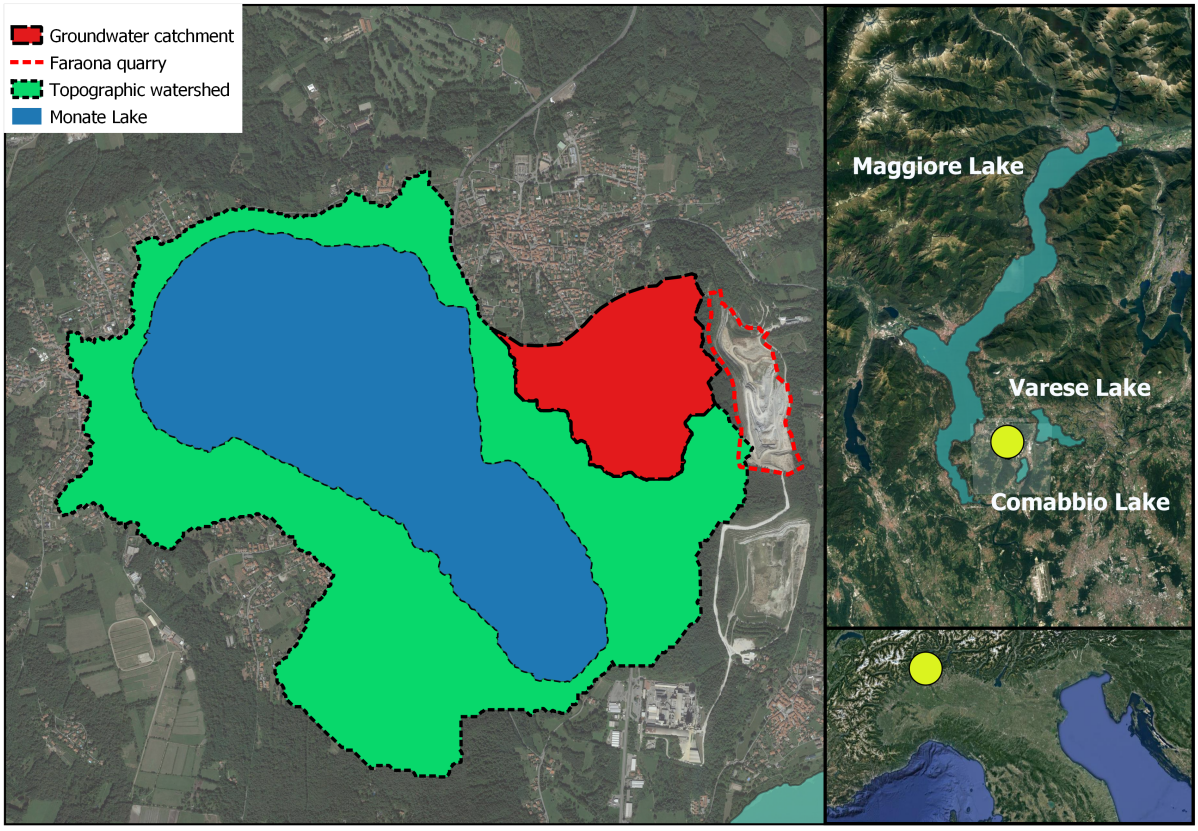

Figure 1.2: The catchment area of Monate Lake. The topographic watershed is shown in green, obtained from Digital Terrain Model (DTM). The estimated groundwater catchment is represented in red (Barnaba, 1987), the Monate Lake in blue. The Cava Faraona is depicted as as a red dashed line.

Regarding the catchment area of Monate Lake, several geological studies have proved the presence of an impermeable rocky substratum of the tertiary age, arranged in layers inclined towards West, therefore towards the Lake itself. This substrate is covered by a moraine layer of quaternary origin, whose thickness varies from few to some dozen meters, locally reaching even a hundred meters. The area is also affected by an important outcrop

of Eocene Nummulitic limestones, cultivated in Santa Marta and Faraona quarries, located East of the Lake (Barnaba, 1987; Montanari and Castellarin, 2012). Although the rocky substrate is mainly impermeable, the presence of tectonic or primary origin cracks is possible that may be site of water veins. This hypothesis is supported by the presence of an aqueduct and industrial wells characterized by a water level compatible with the bedrock levels. The aforementioned wells, in particular the one located East of Cava Faraona (Figure 1.2), have a significant importance and a permanent supply. It is possible that the supply dynamics of these wells are more complex than simple feeding by the quaternary substrate, speculating the presence of cracks, albeit modest, in the rocky substrate. As evidence of this, the quaternary substrate could not guarantee a permanent and constant water supply, especially during periods of prolonged dry season. Despite this, the deposits are feed by the aquifer on during the upwelling of the aquifer itself, originated by meteoric precipitation. Thus, the water volumes remain for long time, guaranteeing supply to the lake even in the dry periods (Montanari and Castellarin, 2012). Given the absence of important tributaries, the contributions to the basin are mainly of a meteoric nature, which feeds the lake through direct precipitation and the aquifer by percolation and underground infiltration. The low ratio between the areas of the catchment and lake surface involves a difficult and slow renewal of the water lake, due to the limited volume of inflows into the basin. Considering the volume of water stored in the lake (about 45 Mm^3) and the average annual outflow (about 3.45 Mm^3), a renewal time of over 13 years is estimated. This information is relevant for the lake health evaluation: in such long periods, accumulations of the polluting materials in the waters could originate. Barnaba (1987) has widely investigated the identification of hydrological Monate Lake basin boundaries. For the descending inclination of the predominantly impermeable substrate layers from East to West, the phreatic watershed between Monate and Varese Lakes does not coincide with the topographical watershed. For this reason, in addition to the surface and underground contributions of the hydrographic basin, it is also necessary to take into account groundwater catchment outside the superficial catchment basin South-East of Travedona, which favors the percolation of the water towards the Lake (Figure 1.2). In particular, according to Barnaba (1987), the extension of the hydrological basin of Monate Lake is about to 6.49 km^2, a value including the 5.75 km^2 resulting from the analysis of the topographical watershed position (surface catchment basin) and 0.74 km^2 which are located South-East of Travedona beyond the topographical watershed with Varese Lake.

1.2.2 Monitoring network

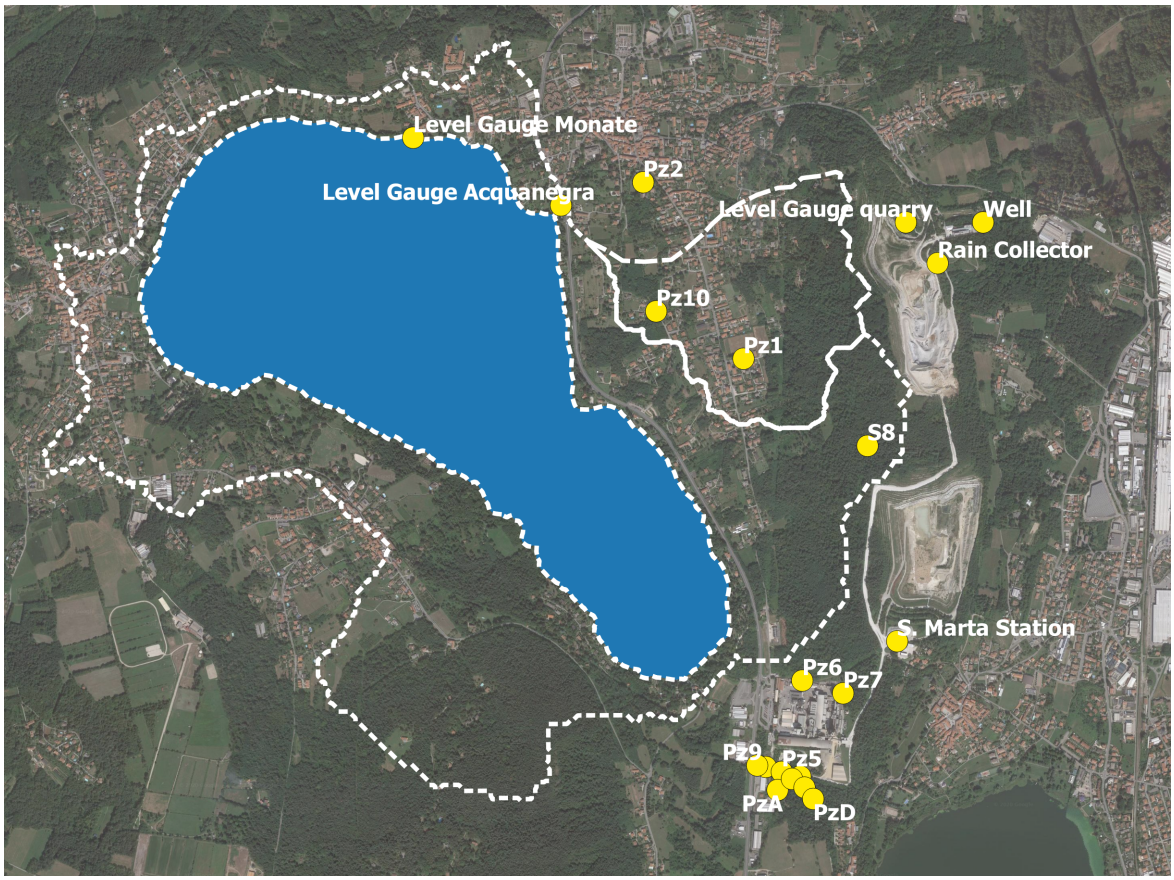

Figure 1.3: Study area monitoring network (yellow points).

In 2013 Holcim SpA has installed a hydrometeoclimatic monitoring network in order to study the lake behaviour relating to the quarrying activities in Cava Faraona (Figure 1.2). To evaluate the possible quarry cultivation work effects on the lake water balance and to detect hydrometric level changes in the subsoil, a dense network of piezometers was created throughout the area (see "Pz" in Figure 1.3). The observation period considered in this work is 01/01/2014 - 01/12/2019. The latest monitoring report updated to 2020 confirms the presence of a watershed placed in an intermediate position between Pz1 and Pz2 piezometers (Figure 1.3), already hypothesized in previous studies (Barnaba, 1987; Montanari and Castellarin, 2012). To verify the existence of the groundwater divide and better estimate pressure surface contours trends, a new piezometer (Pz10) was introduced in June 2016. In this point, the lake being fed by the aquifer (in the Southern portion where the Pz1 is located), is going to feed the aquifer itself, in the Northern portion (Pz2 location). Comparing the trend of phreatimetric simulations referring to different seasons, the position variation of the phreatic line relative to 266 m a.s.l. (average altitude of Monate Lake and therefore it can be interpreted as an approximation of the groundwater

catchment) is evident (Figure 1.4).

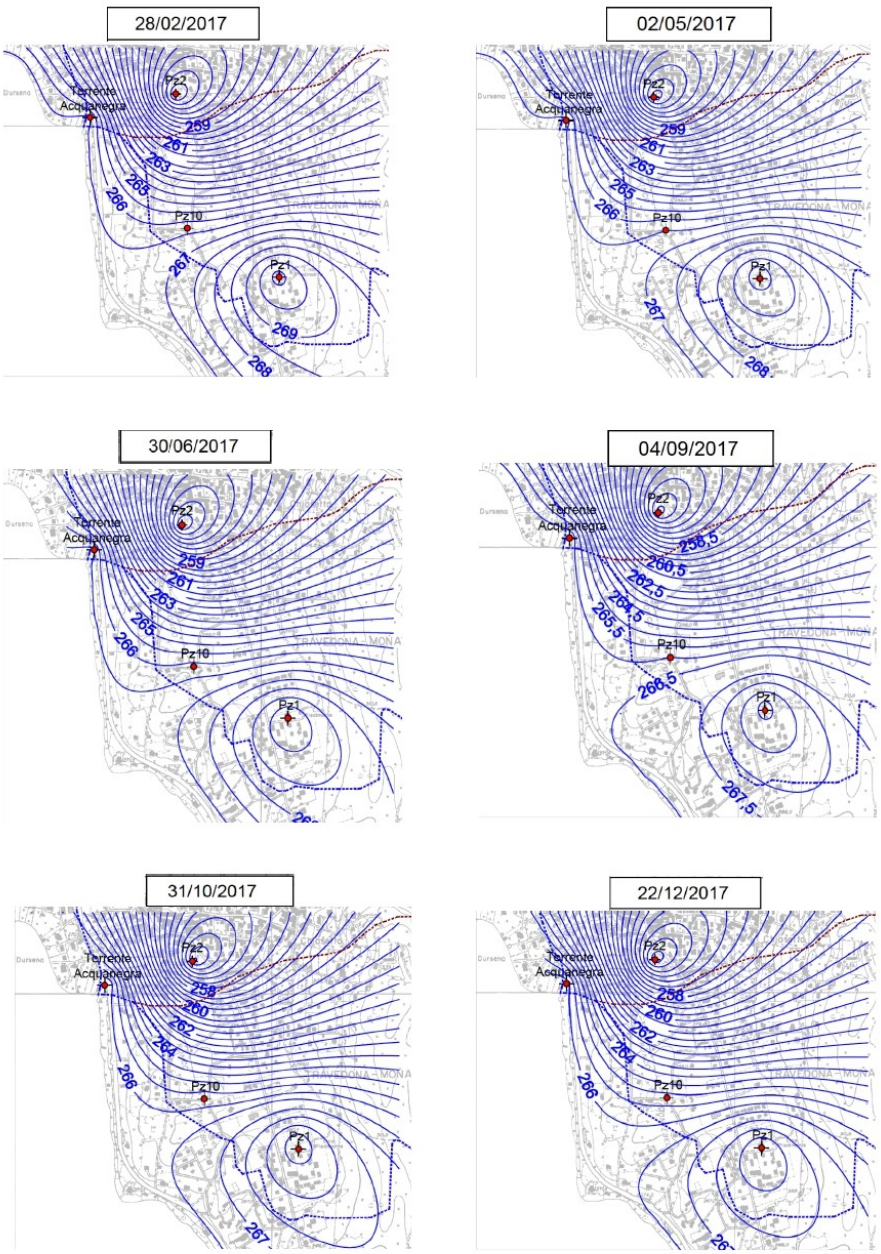

Figure 1.4: Example of isoline representation of the water table relative to 266 m a.s.l. during IV monitoring year.

Hydrometric and meteorological data

A data logger and biweekly campaigns with hydrometric rod (Level Gauge Monate, Figure 1.3) assess Monate Lake water levels. Regarding the Acquanegra stream, a digital hydrometric rod is installed, allowing remote monitoring of the creek levels (Level Gauge Acquanegra, Figure 1.3). This information is useful for the flow rate hydrogram reconstruction, after identification of the most suitable flow scale. The available data for the

hydrological model implementation are collected by:

- Two/four-monthly reports that, since October 2013, have been dealing with environmental monitoring of the survey area,in particular, it collects:
  - Flow data from Mainstream, located at "Level Gauged Acquanegra" in Figure 1.3;
  - Piezometric data (Pz1-10 and PzA-D, Figure 1.3);
  - Hydrochemical monitoring and measurements of the hydrometric levels of Monate Lake, carried out both manually through the use of a hydrometric rod installed on the North shore of the lake, and continuously via data-logger, present since Decemeber 2013;
  - Measurements of hydrometric levels and survey of Acquanegra stream section: a digital hydrometric rod is used for remote level measurements;
  - Recording of water volumes pumped from the quarry lake to Varese Lake.
- Thermopluviometric station owned by Holcim SpA, installed in September 2013 at S. Marta quarry ("S.Marta Station", Figure 1.3). The station provides meteoclimatic data such as:
  - Hourly cumulative precipitation values (mm/h);
  - Average, maximum and minimum hourly values of temperature (°C), atmospheric pressure (hPa) and relative humidity (%).
- *Agenzia Regionale per la Protezione dell'Ambiente Lombardia (ARPAL)* (Regional Agency for environmental protection) with the management of fourteen evaporimetric stations installed in 2008 in order to contribute to groundwater levels monitoring. They are distributed throughout territory of Province of Varese and one is located in Cava Faraona, about 1.5 km away from the Holcim SpA thermo-snow-pluviometric station. Meteoclimatic data collected include:
  - Average and maximum daily and hourly wind speed values (m/s);
  - Total daily (MJ/m^2d) and hourly average solar radiation (W/m^2);
  - Cumulative values of hourly (mm/h) and daily (mm) precipitation;
  - Average hourly values of temperature (°C), atmospheric pressure (hPa) and relative humidity (%);
  - Average, maximum and minimum daily values of temperature (°C) and relative humidity (%).

- ARPAL Varano Borghi Station located 3 km from Santa Marta quarry:
  - Average and maximum daily and hourly wind speed values (m/s);
  - Cumulative precipitation over 24 h (mm) and minimum, average and maximum daily temperature (°C).
- ARPAL Somma Lombardo station located 16 km from Santa Marta quarry:
  - Total daily (MJ/m^2d) and hourly average solar radiation (W/m^2).

The period analysed in this work is January 2014 – December 2019. For the data relating to the average daily wind speed and the daily average global solar radiation, useful for evaluating the potential evapotranspiration, reference information are provided by ARPAL Province of Varese. The hourly rainfall and temperature data, pressure and relative humidity (maximum, minimum and average hourly values) information are collected from measurements at "S.Marta Station" managed by Holcim SpA, located at S.Marta quarry.

Mainstream data

From November 2016 a new instrumentation was introduced for the direct measurement of the flow at the Acquanegra stream. Mainstream devices represent a new generation of Area-Velocity transmitters and flow meters. The basic instrumentation consists of an electronic microprocessor unit, an ultrasonic sensor for measuring the average speed of the fluid and a level sensor. Mainstream meter allows the user to configure the precise geometry of the measurement section within the entire equipment, for all regular geometric shapes. Once geometry of the cross-section has been established, the discharge is determined as the product among mean velocity and flow area.
The main strength of this instrumentation is the versatility: it works both in conditions of clean water and in the presence of wastewater, in channels of any shape and size, without requiring the construction of any specific hydraulic work. Within the following analysis, Mainstream flow measurements derived are pivotal: these data allow flow rating curve update for the evaluation of Acquanegra discharge (see Section 1.3.2).

Pre-processing of meteorological data and dataset management

The first phase of data processing required the integration of missing hourly meteorological data, in order to create a complete database suitable for subsequent analyses. The reconstruction of missing data is carried out starting from the values recorded 24 hours before and 24 hours after the missing data, as follows:

- the mean between the two values is calculated for the average values;
- the maximum/minimum between the two values is taken for the maximum/minimum values;
- a null value is taken for precipitation.

Once the hourly data archive is completed, an evaluation of daily step values is performed, according to the following procedure:

- the average over the 24-hour interval is calculated for the average values;
- for the maximum/minimum values the maximum/minimum over the 24-hour interval is considered;
- the cumulative values over the 24-hour interval is taken for the precipitation.

Specifically, both operations are performed automatically by the use of a script set in the R environment (R Core Team, 2019). Exploiting as input hourly meteoclimatic data, the user achieves a dataset with daily data and without missing values. This approach is particularly useful by allowing continuous updating of the database, since the monitoring activities of the area is still ongoing.

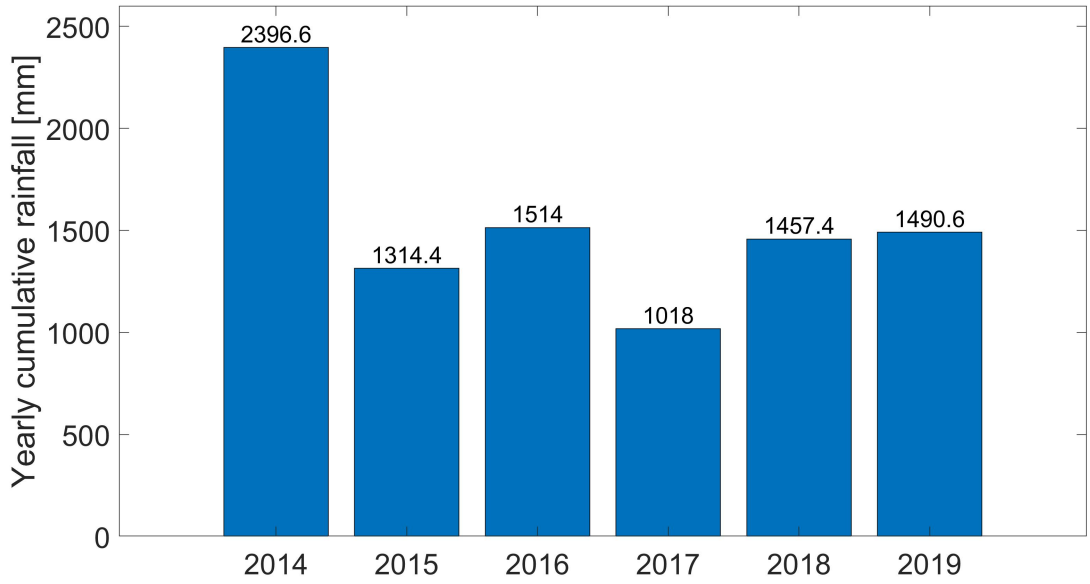

Figure 1.5: Yearly cumulative rainfall [mm] at Varano Borghi station.

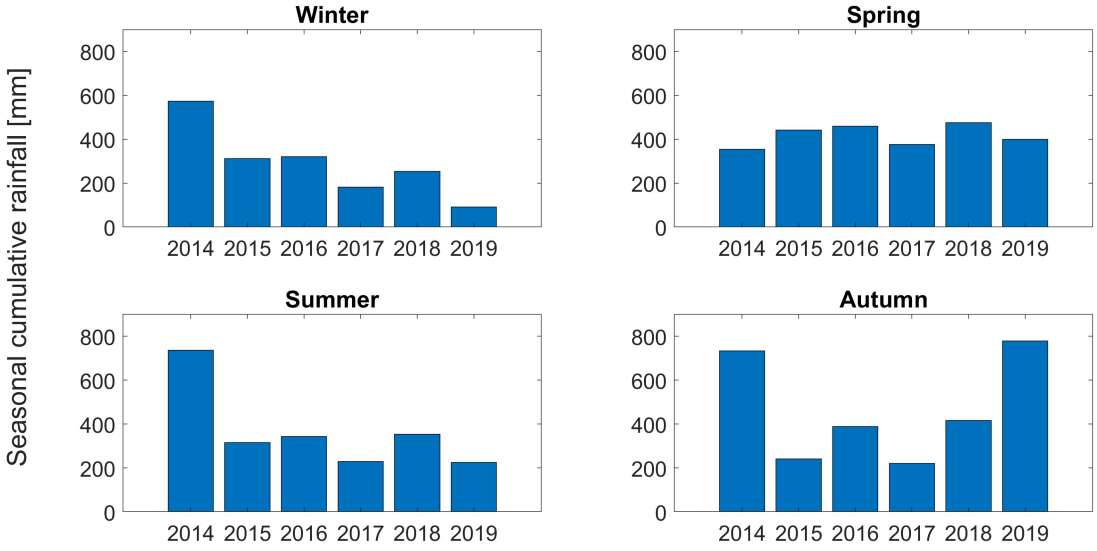

Figure 1.6: Seasonal cumulative rainfall [mm] at Varano Borghi station.

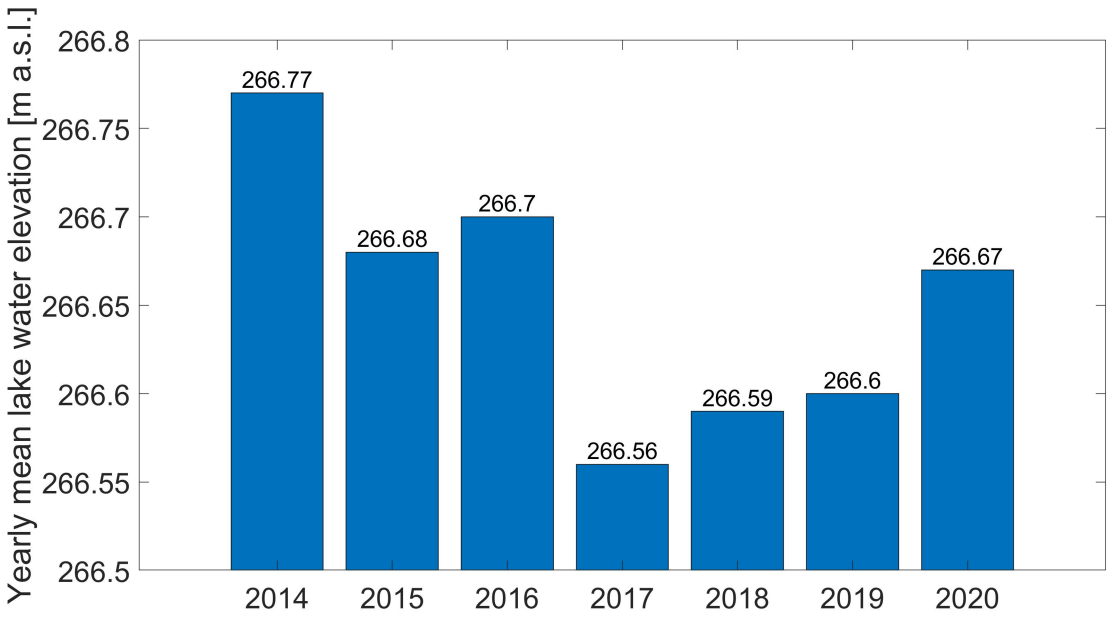

Figure 1.7: Yearly mean lake water elevation [m a.s.l.].

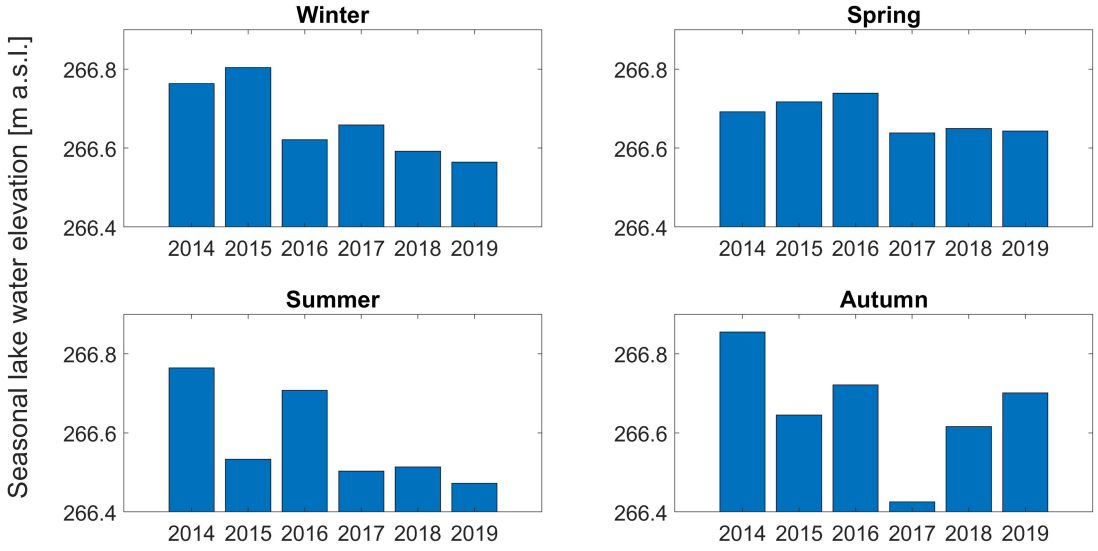

Figure 1.8: Seasonal mean lake water elevation [m a.s.l.].

1.3 Hydrological model

The objective of rainfall-runoff models is to simulate outflow produced by precipitation on a basin. They aim to represent the set of processes at the base of the hydrological cycle at the basin scale. The integrated models are particularly versatile and suitable for the description of floods, mitigation of flood risk, but also for water resources management. An example is the Bucket Model, an empirical integrated model with concentrated parameters which assimilates the hydrographic basin to a reservoir, or to a series of reservoirs, receiving a meteoric precipitation as an input and releasing the water volume by means of appropriately positioned discharges. The great limitation of the standard Bucket Model is the presence of a single discharge threshold of the surface runoff, not describing its real gradual production. The organic soil, that concerns the first layer of soil where evapotranspiration occurs, has different water storage capacities depending on the considered area within the same basin. In particular the storage capacity increases in flat areas, vice versa in mountainous zones. To overcome this limit, applications of different Bucket Model have been developed, arranged in series or in parallel, in order to make the representation of the basin surface flow more realistic. However, this solution does not definitively solve the problem. Despite this, the simplicity of this type of models makes them particularly suitable for applications that are not supported by an adequate knowledge of the contributing basin, for example for uninstrumented basins.
The Probability Distributed Model (PDM) (Moore and Clarke, 1981; Moore, 2007) represents an extension of the Bucket Model when the distribution of different water storage capacities that characterize the basin is to be reproduced. The PDM model aims to overcome the limitation imposed by the linear reservoir model, proposing an approach capable of providing more regular objective functions. The absorption capacity variability (i.e. of the canopy and of soil) within the catchment is characterised by a probability density function of a determined shape, defined by parameters that will later need to be fixed or calibrated. The model inputs are the precipitation on the basin and the potential evapotranspiration.
Its functioning mechanism is described as follows: the rain is stored in a reservoir, representing the ground, thus the stored water level and the saturated area are estimated. The surface runoff originates from the excess of saturation. The water that does not infiltrate defines the surface accumulation and it is stored in another reservoir (or more reservoirs in series) from which, through the bottom outflow, the surface contribution to the river flow escapes. Otherwise, the deep contribution originates from the reservoir bottom discharge. For this work HyMOD model is used (see Section 1.3.1), which has a series of common

features with the previously described models. HyMOD is widely investigated in literature and exploited in hydrological applications (Castiglioni et al., 2010; Lombardi et al., 2012; Cervi et al., 2018) .

1.3.1 HyMOD model

The HyMOD model proposed by Boyle (2001) is based on the same principle of the PDM model, assuming the storage capacity of the soil is variable within the basin. The conceptual scheme of the HyMOD model is reported in Figure 1.9.

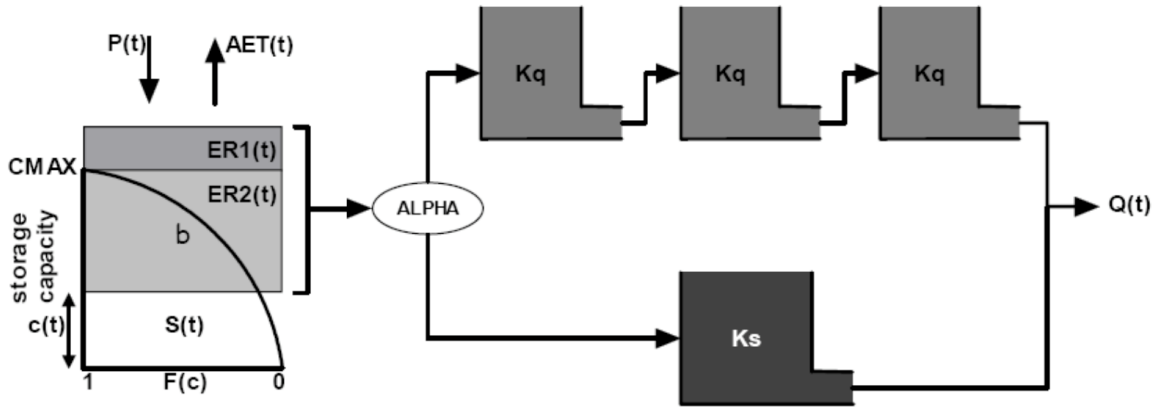

Figure 1.9: Schematic representation of HyMOD model (Boyle, 2001)

The structure of the model requires that the quantity of water falling on the basin in form of precipitation, once purged from evapotranspiration, is divided into underground and surface flows. This conceptual scheme derives from the experimental evidence that the precipitation only partly infiltrates the soil, depending on the local value of storage capacity. For this reason, the superficial and underground portions of soil, represented from distinct reservoirs, receive a quantity of water directly depending on their storage capacity.
In particular, to represent the frequency distribution and therefore the spatial variability of the storage capacity of the basin $C(t)$ [mm], the HyMOD model exploits the Pareto distribution, expressed as:

$$F(C(t)) = 1 - \left(\frac{C(t)}{C_{\max}}\right)^{\beta} \qquad 0 \leq C(t) \leq C_{max} \tag{1.1}$$

Equation 1.1 describes the probability of not exceeding the water storage capacity for a particular local value of $C(t)$.

The distribution parameters are:

- C_{max} [mm] identifies the maximum retention capacity of the basin;
- β [/] identifies the shape of the distribution. It is a calibration parameter that quantifies the variability of the water retention capacity of the basin. In particular:
  - if $\beta = 1$ the distribution is uniform, so all values between 0 and C_{max} have the same probability. There is therefore a linear trend in the distribution;
  - if $\beta > 1$ the distribution assumes a downward concavity, thus low values of C are more frequent than high values;
  - if $\beta < 1$ the distribution assumes a concavity towards the top, thus high values of C are more frequent than low values;
  - if $\beta = 0$ the distribution degenerates into a probability function always equal to 0 except for the value equal to C_{max} (for which the probability is equal to 1), therefore constant storage capacity (see Bucket Model).

$C(t)$ represents the local water content at the generic instant of time, expressed as water height. In areas where the storage capacity is higher than $C(t)$, the rain is intercepted by the basin, infiltrates and is stored; once the basin is saturated, the rain volume part that organic soil is unable to retain, becomes outflow $ER(t)$. This amount of water can be expressed as:

$$ER(t) = ER_1(t) + ER_2(t) \tag{1.2}$$

Both components of equation 1.2 depend on a new parameter α [/] as follow:

- $ER_1 = \alpha ER(t)$, input of a cascade of linear reservoirs (concept of Nash Model), characterized by K_{quick} [T^{-1}] that identifies the surface runoff;
- $ER_2 = (1 - \alpha)ER(t)$ input of a single linear reservoir, characterized by K_{slow} [T^{-1}] that identifies the based flow.

The surface runoff and baseflow determinate the total discharge at the basin outlet. The water volume stored on the basin can be expressed as:

$$W(t) = C(t) - \left[\int_0^{C(t)} F(\Psi) d\Psi \right] \tag{1.3}$$

Through the integral development of 1.3:

$$\int_0^{C(t)} F(\Psi) d\Psi = \int_0^{C(t)} \left[1 - \left(1 - \frac{\Psi}{C_{max}} \right)^{\beta} \right] d\Psi \tag{1.4}$$

$$\int_0^{C(t)} F(\Psi)d\Psi = C(t) + \left[\frac{C_{max}}{\beta+1}\left[1 - \frac{\Psi(t)}{C_{max}}\right]^{\beta+1}\right]_{\Psi(t)=0}^{\Psi(t)=C(t)} \tag{1.5}$$

$$\int_0^{C(t)} F(\Psi)d\Psi = C(t) + \frac{C_{max}}{\beta+1}\left[1 - \left(1 - \frac{C(t)}{C_{max}}\right)^{\beta+1}\right] \tag{1.6}$$

$$W(t) = \frac{C_{max}}{\beta+1}\left[1 - \left(1 - \frac{C(t)}{C_{max}}\right)^{\beta+1}\right] \tag{1.7}$$

Imposing $C(t) = C_{max}$ in 1.7:

$$W(t) = \frac{C_{max}}{\beta+1} \tag{1.8}$$

Explaining C(t):

$$C(t) = C_{max}\left[1 - \left(1 - W(t)\frac{\beta+1}{C_{max}}\right)^{\frac{1}{\beta+1}}\right] \tag{1.9}$$

Imposing stored water volume in the basin $W(t)$ at a generic time, equation 1.9 allows to estimate stored water volume in areas with the maximum water storage.
The algorith has 7 steps as follow:

1. $C(t) = F(W(t))$ (Equation 1.9);

2. $C(t + \Delta t) = min(C_{max}; C(t) + P(t + \Delta t))$;

3. $ER_1(t + \Delta t) = max(0; C(t) + P(t + \Delta t) - C_{max})$;

4. $W(t + \Delta t) = f^{-1}(C(t + \Delta t))$;

5. $ER_2(t + \Delta t) = max(0; C(t + \Delta t) - C(t) - (W(t + \Delta t) - W(t)))$;

6. Effective evapotranspiration relative to current calculation step is

$$ET(t + \Delta t) = ETP(t + \Delta t) * \frac{W(t + \Delta t)}{W_{max}} \tag{1.10}$$

7. The water volume relative to the current computational step is updated:

$$W(t + \Delta t) = max(0; W(t + \Delta t) - ET(t + \Delta t) \tag{1.11}$$

In the present work the potential evapotranspiration estimation refers to Penman Monteith Formula:

$$ET_0 = \frac{0.408\Delta(R_n - G) + \gamma\frac{900}{T+273}u_2(e_s - e_a)}{\Delta + \gamma(1 + 0.34u_2)} \tag{1.12}$$

where:
R_n = net radiation [$MJm^{-2}d^{-1}$]
G = soil heat flow [$MJm^{-2}d^{-1}$]
T = average air temperature [°C]
u_2 = wind velocity at 2 meters height [ms^{-1}]
e_s-e_a = vapor pressure deficit [kPa]
Δ = saturation curve slope [kPa°C^{-1}]
γ = psychrometric constant [kPa°C^{-1}]

In summary, the HyMOD model is characterised by 5 parameters:

- α [/] which distributes the flow between slow and quick release reservoirs;
- $K_{quik}[\Delta T]$ representing the residence time of the slow release reservoir, where Δt is the selected time step (i.e., 1 day in our case);
- $K_{slow}[\Delta T]$ representing the residence time of the quick release reservoir;
- C_{max} [mm] identifying the maximum local storage capacity of the soil;
- β [/] is the degree of spatial variability of the soil moisture capacity.

The strength of HyMOD model is represented by the basin discretisation in infinitesimal cells which allows to obtain a continuous variation of storage capacity values. Therefore, HyMOD describes the storage capacity in details by the introduction of other parameters, whose limited number allows an easy practical application and a quick model calibration.

1.3.2 Hydrological model of the Monate Lake

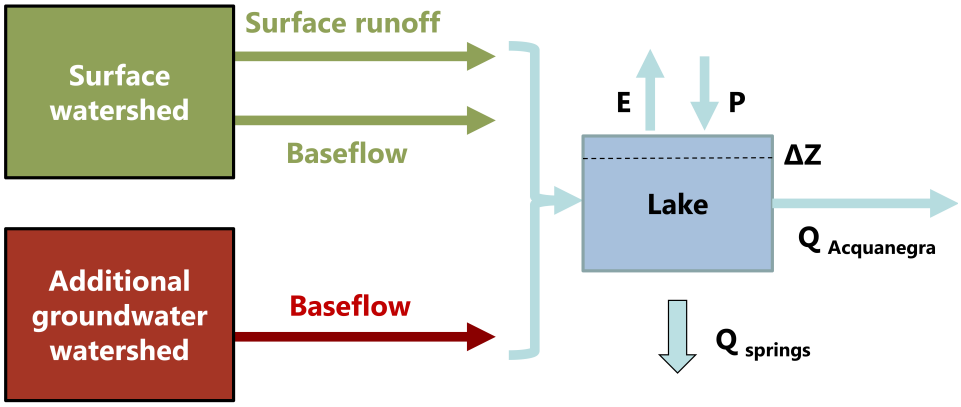

Figure 1.10: Conceptual scheme of the Monate Lake hydrological model.

The study starts from considering the hydrological balance of the lake as conceptualized in Figure 1.10. This model structure has been initially implemented during previous investigations (Soligno, 2015; Tomesani, 2016; Leuci, 2017; Stumpo, 2019) in R environment. The model structure reflects the hydrogeological setting of the survey area, in which the groundwater catchment is larger than the topographical catchment. The model assumes that an additional groundwater catchment concurs to baselow towards the Monate Lake. In summary, the water supplies to Monate Lake come both from the surface or topographical catchment and the additional groundwater catchment in terms of baseflow; the surface runoff is only relative to the superficial hydrographic basin.
In particular, the hydrological model consists of by two Parts (Figure 1.10):

- Part 1: HyMOD for the simulation of daily surface runoff (green box, Figure 1.10) and baseflow (brown box, Figure 1.10). The HyMOD equations are applied to the topographic catchment (excluding the lake area) and to the groundwater catchment. The necessary data for this application are: daily cumulated rainfall and daily cumulated potential evapotranspiration on hydrographic and groundwater catchment, respectively;

- Part 2: lake water body. This component simulates outflow. The component receives precipitation as a direct inflow and simulates evapotranspiration fluxes at each daily time step. This net inflow volume is then converted into water level variations (ΔZ, Figure 1.10). Based on the water level and the Acquanegra rating curve, the stream discharge is computed. Near the Acquanegra gauging station ("Level Gauge Acquanegra", Figure 1.3), two gates are present for the regulation of the Acquanegra flows. These gates are normally open, yet if closed, they prevent the

water to flow into the stream. The gates are closed when the Acquanegra channel undergoes maintenance operations. A lateral bypass prevents excessive water levels when gates are closed, protecting the shores from flooding (Figure 1.11). The lateral weir has a single span of 0.11 x 7.83 m at an average elevation of 266.96 m a.s.l. Thus when the gates are closed and the water level is higher than this elevation, the lateral weir comes into operation allowing the water to bypass the gates and to reach the Acquanegra emissary. In the condition of maximum levels above the lateral weir (i.e. for lake water levels of 267.27 m a.s.l.), the discharge is equal to 2.30 m^3/s. The model represents the by-pass and correctly simulates its hydraulic behaviour once the maintenance periods are known and the gates are simulated as closed. The input data for the simulation are the cumulated rainfall, lake evaporation, lake water level at the beginning of simulation period and simulated inflow from Part 1. The variation of water level is estimated as:

$$\Delta Z = \frac{q_{tot}\Delta t}{A_{lago}} + (P - E) \tag{1.13}$$

where

- q_{tot} is the entire inflow simulated at each time step by Part 1;
- Δt is the time step (in seconds);
- P and E are the lake precipitation and evaporation, respectively in [mm].

The Acquanegra discharge can be evaluated through an empirical rating-curve which reads:

$$Q(t)_{stream} = a(Z_{masl}(t) - Z_{bottom})^b = 1.671(Z_{masl} - 266.44)^{1.765} \tag{1.14}$$

where Z_{masl} and Z_{bottom} indicate the water level elevation and Acquanegra cross-section lowest elevation of the gauging station. This relationship is valid only in case of open gates, whereas when the gates are completely closed:

- if $Z \leq 266.96$ m a.s.l., $Q(t)_{\text{stream}} = 0$;
- if $Z > 266.96$ m a.s.l., the discharge can be calculated by:

$$Q(t)_{torrente} = \mu L(Z_{masl}(t) - Z_{weir})\sqrt{2g(Z_{masl}(t) - Z_{weir})} \tag{1.15}$$

where Z indicates the quote of lake water level, with μ equal to 0.385, L is the lateral weir length and g the gravitational acceleration. Once Acquanegra

discharge is calculated, an updating of lake water level is needed:

$$Z(t+\Delta t)_{updated} = Z(t+\Delta t) - \frac{Q_{stream}\Delta t}{A_{lake}} \tag{1.16}$$

Figure 1.11: The lateral weir for by-passing the Acquanegra gates.

As shown in Figure 1.10, an additional outflow from the Lake is represented in the model (Q_{springs}). This additional loss term represents a deep percolation from the lake which feeds a system of springs located North-East to the lake of Monate, where a golf course is present. A survey campaign in May 2019 quantified this perennial discharge in about 56 l/s. The introduction of this loss in the model is fundamental to accurately represent the water balance.

1.3.3 Generalization: the groundwater catchment contributing area as variable of the system

The size of the additional groundwater catchment can be roughly estimated from Barnaba (1987) in about 0.576 km^2. The present work aims to consider the underground extrabasin area (A_{u}) as a variable of the system, proposing four strategies for HyMOD modification.
In the first modelling strategy (H1), A_{u} is simply considered as a sixth parameter, calibrated within the range 0.3 km^2 - 0.9 km^2. In order to introduce the concept of seasonality for A_{u} variation, the second modelling strategy (H2) adopts a sinusoidal behaviour of A_{u} during the observation period, according to the following expression:

$$A_u(i) = 0.576 * \mathbf{param\ 6} * sin\left(2\pi * \frac{(i + \mathbf{param\ 7})}{\mathbf{param\ 8}}\right) \tag{1.17}$$

Considering i as the reference day, A_{u} shows sine trend along the whole observation period, varying within minimum and maximum values [km^2] given from the sinusoidal

amplitude [/] (**param 6**). Since the seasonality variation of A_{u} can start shifted from the reference day, a sinusoidal phase is inserted (**param 7**), whereas the period (the length of one cycle of the curve) is represented by **param 8**.
In order to reduce the number of additional parameters, the third modelling strategy (H3) aims to introduce a direct relationship between A_{u} and the antecedent cumulative precipitation on the basin.
As said in Section 1.3.2, the HyMOD equations are applied to the surface and the additional groundwater watersheds distinctly. The two model inputs are the daily cumulative rainfall and the daily potential evapotranspiration for both topographic and additional groundwater catchment, provided by the monitoring network. In the third modelling strategy (H3) the input to the additional groundwater catchment is a series of adjusted daily rainfall values (p_{sott}) calculated as:

$$p_{sott}(i) = p(i) * \left[1 + \textbf{param 6}\left(\frac{p_{cum}(i)}{p_m} - 1\right)\right] \tag{1.18}$$

As indicated by eq. 1.18, p_{sott} is given by the product between the daily precipitation at the reference day ($p(i)$) and an adjusting coefficient that is a function of the ratio between the cumulative 90-day rainfall before i ($p_{\mathrm{cum}}(i)$) and the mean cumulative 90-day precipitation over the entire observation period (p_{m}), multiplied by an amplitude coefficient [/] (**param 6**). The rainfall data used in this modelling strategy were observed at ARPAL Varano Borghi raingauge, located 3 km from Santa Marta quarry. The Figure 1.5 depicts the yearly cumulative rainfall trend at Varano Borghi station, whereas the Figure 1.6 shows the seasonal cumulative rainfall.
In the presented models (H1, H2 and H3), Q_{springs} has a fixed value of 56 l/s, measured during the survey of May 2019. A fourth modelling strategy (H4) uses assumption of H3 and adopts as **param 7** the discharge of deep percolation Q_{s}, which is calibrated between the arbitrary selected upper and lower limits, 20 l/s and 150 l/s, respectively.

1.4 Calibration and validation strategies

We adopted the Genetic Algorithm (GA) as the automatic model calibration procedure. GA is a type of evolutionary computer algorithm in which genes representing possible solutions are generated. This breeding of genes includes the use of mechanism analogous to the crossing-over process in genetic recombination and an adjustable mutation rate (Hosch, 2017). A fitness function is used on each generation of algorithms to gradually improve the solutions in analogy to the process of natural selection. GA inherits and readjusts biological terminology, such as:

- Population: set of multiple solution candidates which are iteratively refined;
- Chromosome: one of the problem solution, generally codified with a characters or bit array;
- Gene: part of a chromosome;
- Fitness: assessment grade relative to a solution. The evaluation is based on *ah hoc* fitness function;
- Crossover: the process of improving and combining traits of the currently known solutions;
- Mutation: random alteration of a solution. The mutation process can generate a better or worse solution but in each chance limits the trapping of subsequent generations in local optima.

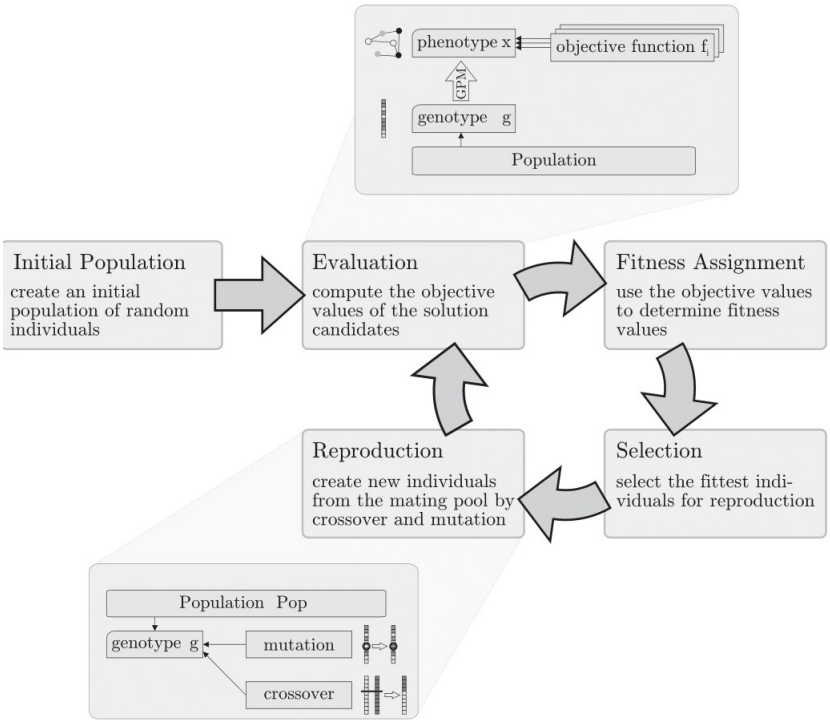

Figure 1.12: The basic cycle of Genetic Algorithms (Weise, 2009).

Figure 1.12 summarizes GA process. In this work GA package (Scrucca, 2013) in R environment is exploited for the automatic calibration. Three different calibration strategies have been developed. The Objective Function (F.O.) of the first strategy (S1)

is the NSE estimated on the observed (from data logger) and simulated Monate Lake water levels, defined as:

$$NSE(\Theta) = 1 - \frac{\sum_{t=1}^{N} [x(t) - \hat{x}(t)]^2}{\sum_{t=1}^{N} [x(t) - \bar{x}(t)]^2} \tag{1.19}$$

where $\bar{x}(t)$ indicates the average observed water level and N is the number of observation. NSE ranges between - ∞ and 1, when the simulated values fit perfectly the observed ones. Thus NSE must be maximised in the calibration phase.
In the second calibration strategy (S2), F.O. is the combination of NSE estimated on the water levels (see S1) and Spearman's rank correlation coefficient (ρ_s) on daily simulated baseflow and the daily average of piezometric levels of Pz1 and Pz10 . These two piezometers are located inside of the groundwater area (red area, Figure 1.2). ρ_s is a non parametric measure of the statistical dependence between the rankings of two variables, defined as:

$$\rho_s = 1 - \frac{6 \sum_i D_i^2}{N(N^2 - 1)} \tag{1.20}$$

where $D_i = r_i - s_i$ is the difference between the two ranks of each observation, with r_i and s_i first and second variable ranks respectively; N is the number of observations. Spearman correlation ranges among -1 and + 1. The sign indicates the direction of association between the two variables, X and Y. If Y tends to increase when X increases, the Spearman correlation coefficient is positive. If Y tends to decrease when X increases, the Spearman correlation coefficient is negative. A Spearman correlation of zero indicates that there is no tendency for Y to either increase or decrease when X increases.
The strategy 3 (S3) assesses the NSE among observed (from spot measurements) and simulated lake water levels.
S1 and S3 have been tested on the whole observation period (01/01/2014 - 1/12/2019), whereas S2 on a shorter temporal window (01/07/2016 - 31/12/2016) since Pz10 data are available only from 15/06/2016. The goodness of simulation results is evaluated estimating ME, RMSE and NSE among observed and simulated lake water levels and among Acquanegra discharge from Equation 1.15 (from now on called "reference Acquanegra discharge") and simulated one.
For S1 and S3, other calibrations have been explored relative to different periods (see Figure 1.5):

- 2017, which has been characterized by the lowest yearly cumulative precipitation value;
- 2016, representing the average precipitation trend of the whole observation period;

- 2014, the most rainy year during the observation period.

Considering these observation periods, the validation is carried out comparing observed and simulated variables (i.e., lake water levels, Acquanegra discharge) for the remaining period within the considered time frame (2014-2019). The Mainstream data would be more suitable than reference Acquanegra discharge data (provided by equation 1.14) in this phase. Unfortunately, it is impossible to exploit Mainstream information since available only from the second half of the observation period (from 1/1/2017). In this case, Acquanegra discharge values are in good agreement with Mainstream ones (see Figure 1.13), thus it can be assumed that using empirical discharge values does not introduce significant errors.

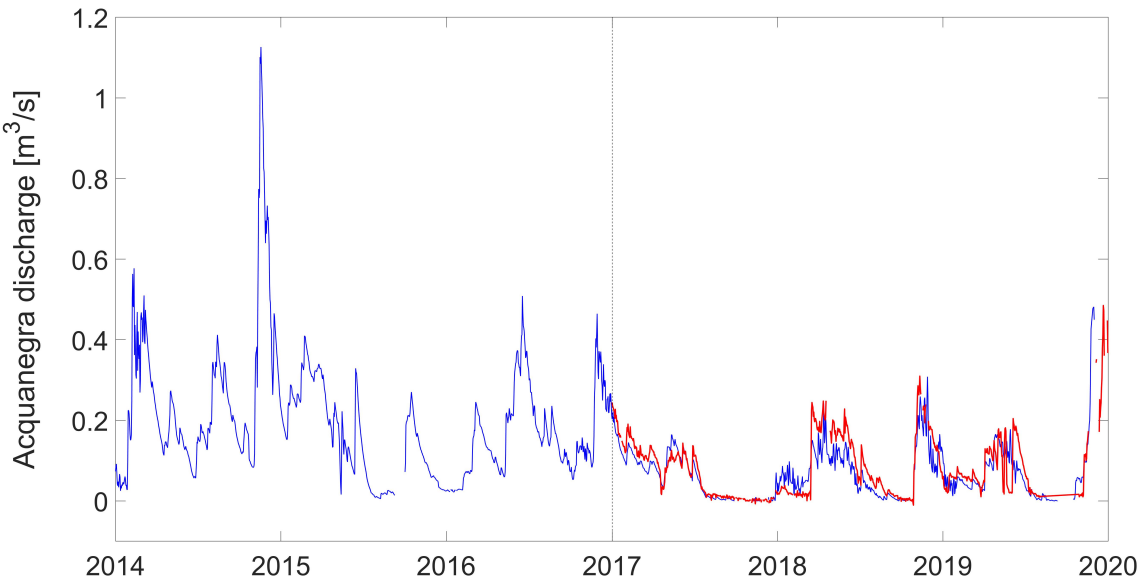

Figure 1.13: Acquanegra discharge [m^3/s] estimated with Equation 1.15 (blue line) and measured by Mainstream (red line) from 01/01/2017.

1.5 Results and discussion

Since the higher completeness ensured by H4 with respect to the previous configurations and for the sake of brevity, in this section only the comparison between the original HyMOD (H) and the H4 model is presented. H4 has been tested for several periods of cumulative rainfall (i.e. 30, 60, 90 and 180 days). Since these different parametrizations produced very similar results in calibration performances, it has been decided to only present H4 with 90 days-period results. Table 1.1 reports the variability range of the calibrated parameters for H and H4 models.
Table 1.2 sums up the calibration results for both models relative to different calibration strategies and periods (see Section 1.3).

Table 1.1: Variability ranges of the model parameters.

Model	$C_{\mathbf{max}}$ [mm]	β [/]	α [/]	$K_{\mathbf{slow}}$ [ΔT]	$K_{\mathbf{quick}}$ [ΔT]	$A_{\mathbf{rain}}$ [/]	$Q_{\mathbf{s}}$ [l/s]
H	50 - 500	0.1 - 2	0.2 - 0.8	0.005 - 0.99	0.05 - 0.99	/	/
H4	50 - 500	0.1 - 2	0.2 - 0.8	0.005 - 0.99	0.05 - 0.99	-2 - 5	30 -100

Considering the entire observation period (2014 - 2019) the second calibration strategy (S2) does not prove suitable solutions, while S3 outperforms (i.e. F.O. equal to 0.70) in both H and H4. S1 and S3, in general, are in agreement for both H and H4; the better outcome of S3 might probably be due to the estimation of NSE on minor number of lake water level observations (see Section 1.3). For H4, S1 and S4 provide higher values of β, α and K_{slow} compared with H. Q_{s} is about 42 l/s for both calibration strategy, highlighting an overestimation of the fixed Q_{springs} value for H (i.e. 56 l/s). It is probably due to the fact that the survey campaign providing this information was during the spring 2019, which was a rainy period as shown in Figure 1.6.
Table 1.3 reports the simulation performances presenting ME, RMSE and NSE among observed and simulated lake water elevations and Acquanegra discharge. The first calibration strategy (S1) outperforms the calibration strategies for both hydrological models, in particular for H and in lake water levels representation. Figures 1.14 and 1.15 depict simulation results exploiting S1 for H and H4, respectively. Upper panels show the observed (black line) and simulated (red line) Acquanegra discharge [m^3/s]. H4 provides higher discharge values than H in May 2015 - May 2016 and May 2018 - May 2019 periods, whereas presents a better description for 2017. The same tred is present for the lake water level simulation (middle panels). Generally the realistic representation of the

Table 1.2: Calibration performances for H and H4 models.

Model	**Strategy**	**Period**	$C_{\mathbf{max}}$ [mm]	β [/]	α [/]	$K_{\mathbf{slow}}$ [ΔT]	$K_{\mathbf{quick}}$ [ΔT]	$A_{\mathbf{rain}}$ [/]	$Q_{\mathbf{s}}$ [l/s]	**F.O.**
H	S1	2014-2019	198.31	0.12	0.26	0.005	0.23	/	/	0.66
H	S2	2016	369.05	0.11	0.20	0.13	0.10	/	/	0.14
H	S3	2014-2019	101.26	0.32	0.52	0.005	0.38	/	/	0.70
H	S1	2014	341.05	1.99	0.48	0.005	0.19	/	/	0.84
H	S3	2014	101.10	1.98	0.60	0.005	0.37	/	/	0.57
H	S1	2016	105.87	1.98	0.21	0.022	0.11	/	/	0.81
H	S3	2016	103.61	1.98	0.22	0.047	0.12	/	/	0.95
H	S1	2017	217.26	0.11	0.60	0.027	0.57	/	/	0.81
H	S3	2017	440.91	0.14	0.59	0.027	0.59	/	/	0.94
H4	S1	2014-2019	115.71	0.46	0.59	0.22	0.09	1.95	41.57	0.47
H4	S2	2016	212.55	1.88	0.21	0.08	0.13	0.79	190.74	0.06
H4	S3	2014-2019	111.83	0.58	0.56	0.13	0.09	4.91	42.84	0.70
H4	S1	2014	425.65	1.88	0.59	0.48	0.09	-1.86	34.76	0.77
H4	S3	2014	101.45	1.95	0.59	0.01	0.39	-1.94	34.13	0.87
H4	S1	2016	425.10	1.83	0.24	0.04	0.09	4.87	39.39	0.89
H4	S3	2016	210.14	1.65	0.60	0.09	0.11	-0.31	37.19	0.96
H4	S1	2017	221.04	0.12	0.59	0.02	0.54	0.04	153.39	0.85
H4	S3	2017	158.45	1.08	0.59	0.09	0.58	-1.94	90.02	0.97

second half of 2018 and 2019, featured by very low flows, seems to be critical for both the models. The main difference between H and H4 simulation results is evident in the bottom panel that plots the observed Acquanegra discharge (blue line), simulated surface runoff (in red) and baselow (in black). H4 provides a sort of pulsation of the baselow, underlining the variation of groundwater catchment with rainfalls.

Table 1.3: Simulation performances for H and H4 models on the observation period 2014-2019. The error metrics are relative to lake water levels (subscript "L") and Acquanegra discharge (subscript "Q").

Model	**Strategy**	$\mathbf{ME_L}$ [m]	$\mathbf{RMSE_L}$ [m]	$\mathbf{NSE_L}$ [/]	$\mathbf{ME_Q}$ [m^3/s]	$\mathbf{RMSE_Q}$ [m^3/s]	$\mathbf{NSE_Q}$ [/]
H	S1	0.02	0.08	0.61	0.01	0.09	0.57
H	S2	-0.05	0.13	-0.06	-0.02	0.11	0.34
H	S3	0.03	0.09	0.54	0.02	0.10	0.37
H4	S1	0.01	0.09	0.47	0.01	0.09	0.47
H4	S2	-1.11	1.30	<-20	-0.09	0.14	-0.09
H4	S3	0.02	0.10	0.45	0.02	0.10	0.37

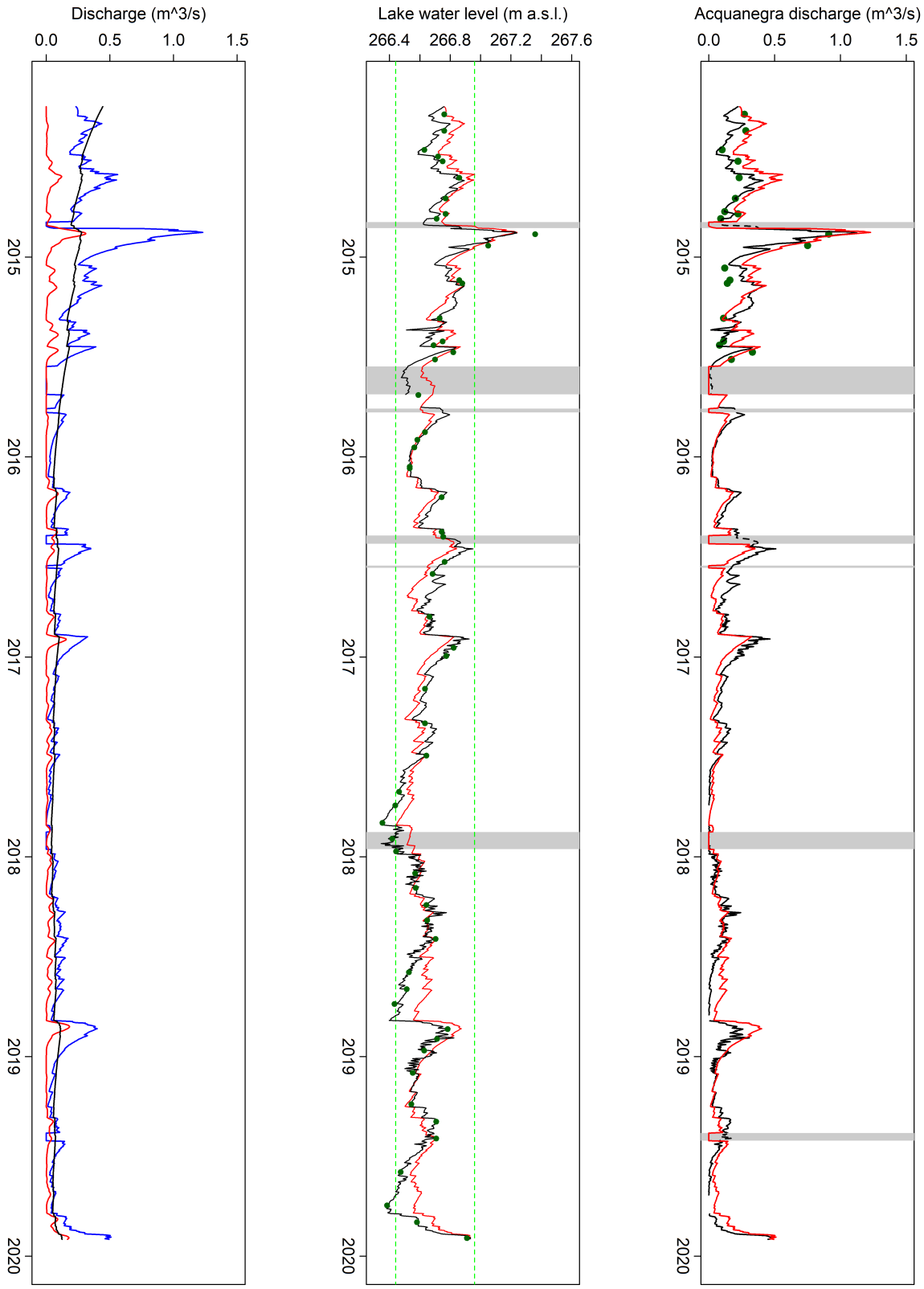

Figure 1.14: H model simulation results. Upper and middle panels depict Acquanegra discharge and lake water levels, respectively. In both images, the red line represents the simulated data, the black line the observed one, while green points indicate the spot measurements. Lower panel shows simulated Acquanegra discharge (blue line), surface runoff (in red) and baselow (in black). The vertical grey boxes show the periods of closed gates.

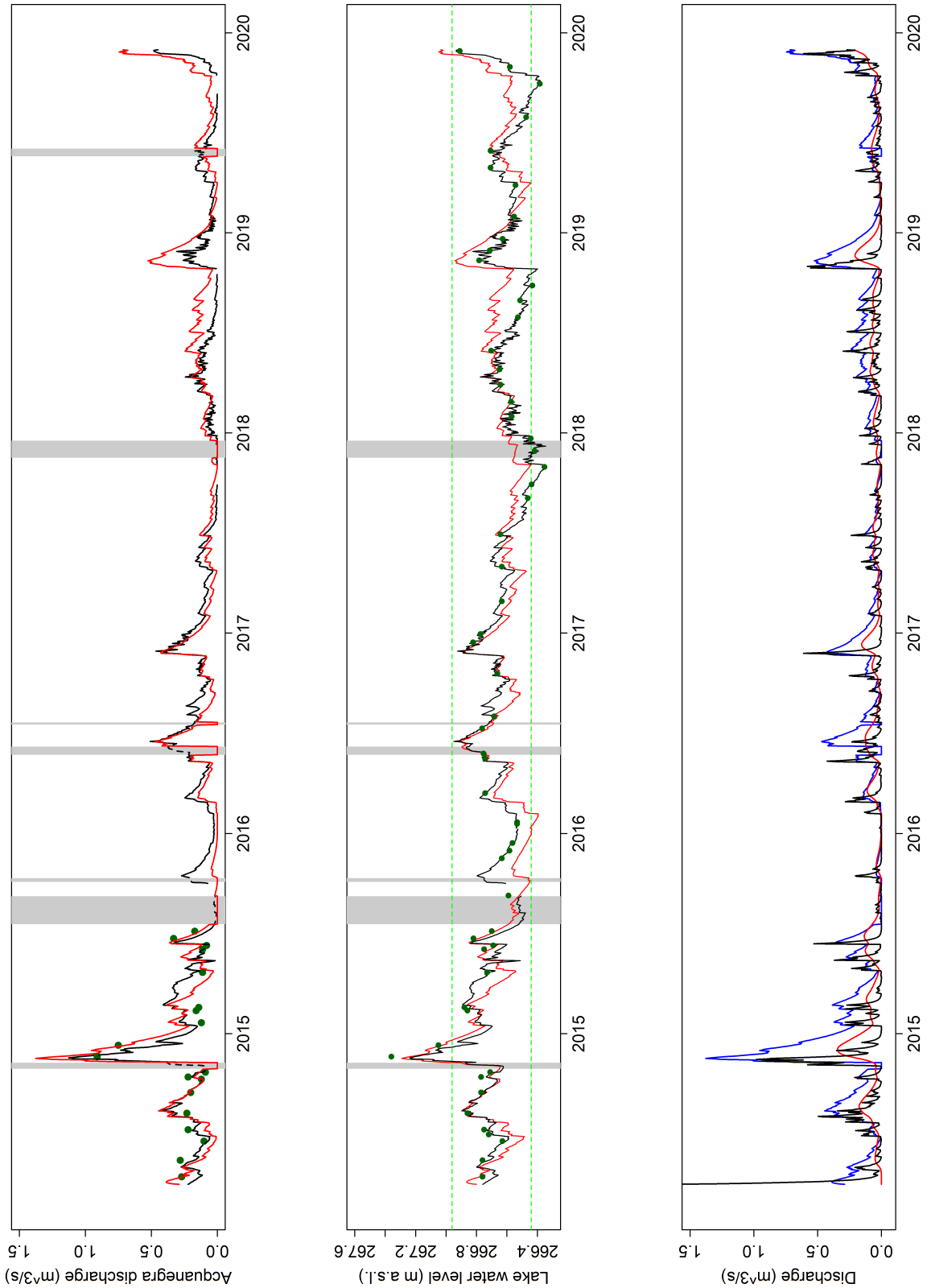

Figure 1.15: H4 model simulation results. Upper and middle panels depict Acquanegra discharge and lake water levels, respectively. In both images the red line represents the simulated data, the black line the observed one, while green points indicate the spot measurements. Lower panel shows simulated Acquanegra discharge (blue line), surface runoff (in red) and baseflow (in black). The vertical grey boxes show the periods of closed gates.

In order to highlight the different meteorological features among the years, Table 1.2 reports also the calibration performance for both H and H4 models relative to:

- 2014, characterized from high rainfalls values;
- 2016, representing the average precipitation trend of the observation period;
- 2017, the driest year.

As hypothesised, the parameters of calibration on 2014 and 2017 are not suitable for the lake behaviour representation on the observation period (Table 1.4). Calibrating on 2016 provides quite good results, in particular with S3 (Table 1.4, Figure).

Table 1.4: Validation performances for H and H4 models. The validation period is the year indicated in the third column, while the remaining part of the observation period 2014-2019 is used for calibration. The error metrics are relative to lake water levels (subscript 'L') and Acquanegra discharge (subscript 'Q').

Model	**Strategy**	**Period**	**ME_L** [m]	**$RMSE_L$** [m]	**NSE_L** [/]	**ME_Q** [m^3/s]	**$RMSE_Q$** [m^3/s]	**NSE_Q** [/]
H	S1	2014	0.07	0.11	0.12	0.04	0.10	-0.01
H	S3	2014	0.07	0.11	0.07	0.05	0.11	-0.33
H	S1	2016	0.08	0.12	0.25	0.07	0.11	0.37
H	S3	2016	0.05	0.10	0.38	0.04	0.10	0.44
H	S1	2017	-0.04	0.13	0.01	-0.02	0.10	0.43
H	S3	2017	-0.05	0.13	-0.03	-0.03	0.10	0.43
H4	S1	2014	0.04	0.11	0.17	0.02	0.10	-0.02
H4	S3	2014	0.10	0.16	-0.97	0.11	0.26	-5.93
H4	S1	2016	0.07	0.13	0.14	0.07	0.14	-0.05
H4	S3	2016	0.05	0.11	0.35	0.04	0.11	0.37
H4	S1	2017	-0.39	0.55	-17	0.09	0.14	0.04
H4	S3	2017	-0.07	0.16	-0.45	-0.03	0.11	0.33

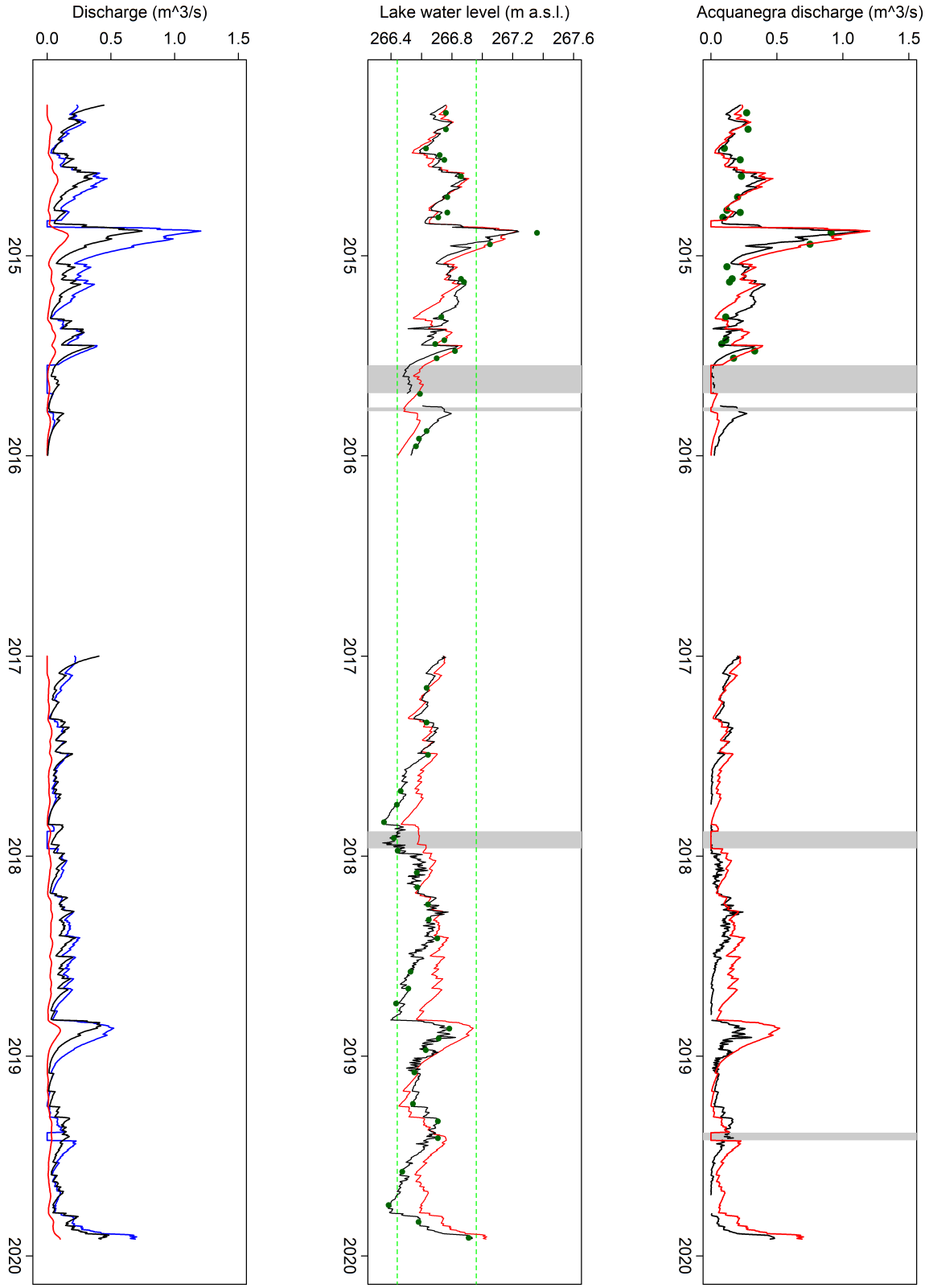

Figure 1.16: H model validation results calibrating on 2016 with S3. Upper and middle panels depict Acquanegra discharge and lake water levels respectively. In both images, the red line represents the simulated data, the black line the observed one one while green points indicate the spot measurements. Lower panel shows simualted Acquanegra discharge (blue line), surface runoff (in red) and baseflow (in black). The vertical grey boxes show the periods of closed gates.

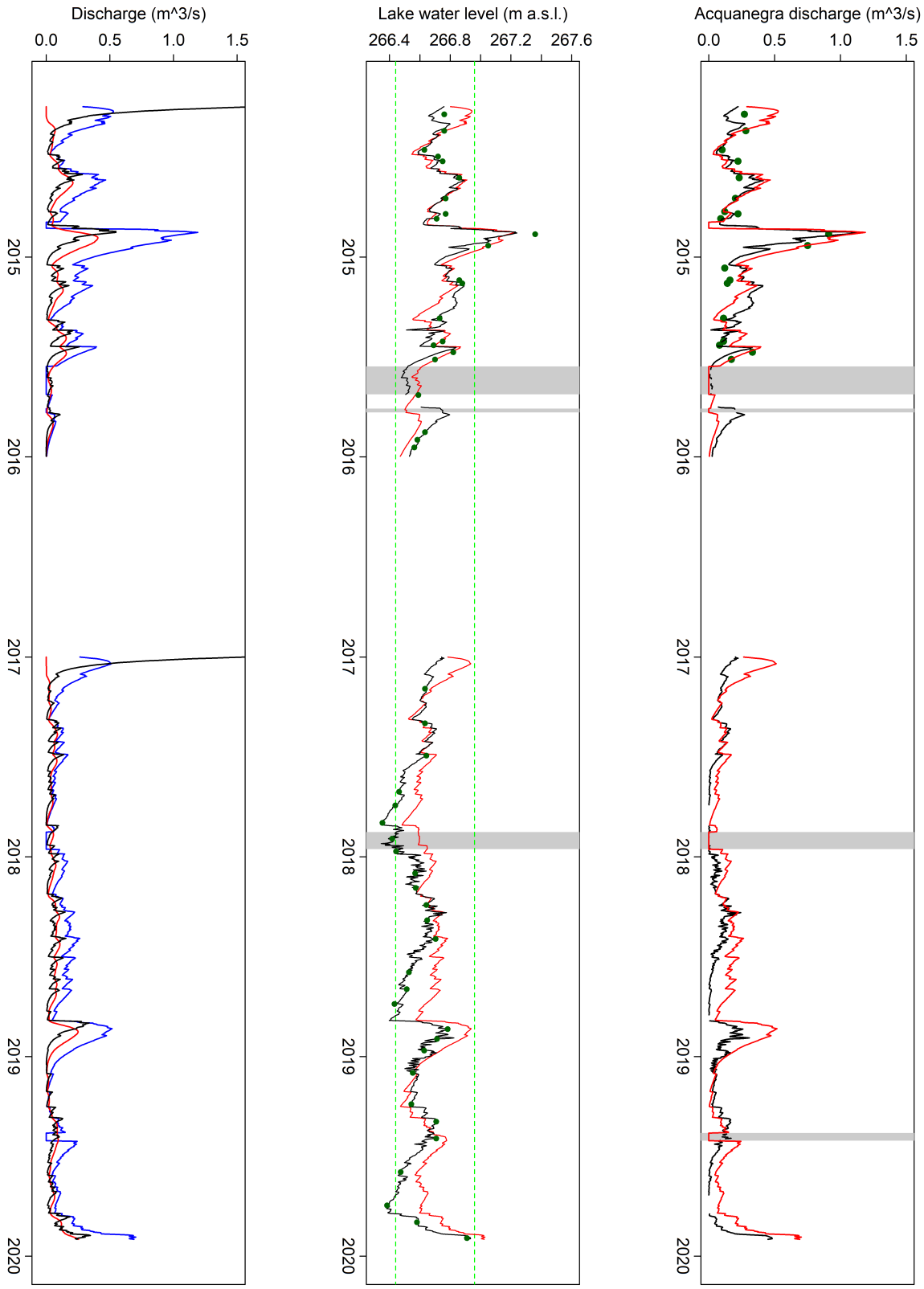

Figure 1.17: H4 model validation results calibrating on 2016 with S3. Upper and middle panels depict Acquanegra discharge and lake water levels respectively. In both images, the red line represents the simulated data, the black line the observed one one while green points indicate the spot measurements. Lower panel shows simualted Acquanegra discharge (blue line), surface runoff (in red) and baseflow (in black). The vertical grey boxes show the periods of closed gates.

In the light of presented results, H4 seems to not provide significant benefits in the lake behaviour simulation respect with H. The proposed modified HyMOD (H4) aims to consider the groundwater catchment, whose determination is quite complex, strictly correlated to the cumulative precipitation on the basin. However, a strong rainfall seasonality is missing along the observation period. Referring to Figure 1.5, 2014 was an extremely rainy year: several reports of ARPAL defined the Winter 2013/2014 *anomalous*, characterized from rainfalls three times superior than the average values. On the other hand, 2017 was very dry, with about one third less precipitation respect with previous and following years. The lack of rainfall seasonality appears also evident analysing the seasonal cumulative rainfall (Figure 1.6): excepting the Spring, the other seasons present a fluctuating trend. Similar patterns are found for yearly and seasonal mean lake water levels (Figures 1.7 and 1.8), evidencing its correlation with rainfall on the basin. Also the validation results based on calibration of 2014, 2016 and 2017 demonstrate this hypothesis. Furthermore, the data availability for the survey area (only 6 years) strongly limits the observation period, that is quite short for considering the seasonality of this complex system. Moreover, some inaccuracies might have been introduced by considering punctual rainfall information (i.e. Varano Borghi station), which may not be representative of the whole basin, and in the assessment of evapotranspiration (see eq. 1.12).

1.6 Concluding remarks

Part 2 of this dissertation is dedicated to the implementation of a semi-distributed conceptual model for a basin with seasonally variable catchment size. Starting from the end of 2013, the Monate Lake basin is surveyed by a dense monitoring network, built in order to study the impact of Cava Faraona activities on the lake behaviour. The peculiarity of this basin consists in the presence of a groundwater catchment located East of the Monate Lake, whose extension was only speculated by previous studies (Barnaba, 1987). The HyMOD model (called "H") is exploited as hydrological model, suitable for reproducing the spatial variability of basin storage capacity. In order to take into consideration the complexity of the study area, the groundwater catchment extent is considered as a variable of the system, proposing different modification of the HyMOD model. In particular, the configuration "H4" considers the groundwater catchment area closely linked to the rainfall seasonality. For brevity, the results are only relative to the comparison between H and H4 models. The goodness of simulations is evaluated from the comparison among observed and simulated lake water levels and Acquanegra discharges, the only emissary of the lake.

The outcomes of the two formulations (H and H4) show similar capabilities in reproducing the lake dynamics, suggesting that the modification of the original model setting (H) does not provide significant benefits. We argue that a 6-years observation period might be too short for investigating the seasonal behaviour of the groundwater catchment, while the influence of single year peculiarity (i.e. high cumulative annual rainfall) influence the analysis. In general, HyMOD reproduces the lake water levels and Acquanegra discharge dynamics (i.e. NSE equal to 0.61), even if showing some limitations in reproducing the driest periods (i.e. summers 2018 and 2019).

Conclusions

This Thesis focuses on the assessment of hydraulic and hydrological variables, proposing innovative methodologies and instruments. The Part 1 addresses three main issues: the river bathymetry estimation based on space-borne data, the river discharge assessment by means Data Assimilation (DA) approaches, the use of satellite altimetry information in hydraulic modelling.

Firstly, in order to overcome the inability of satellite DEMs (i.e. SRTM) in describing the submerged part of the river, the Slope-Break (SB) method, exclusively based on topographic information (i.e. river channel width and elevation), is proposed (Domeneghetti, 2016). Three different study area are surveyed: Po River (Italy), an example of heavily human impacted river, Limpopo River (Mozambique) located in a remote areas and Clarence River (New South Wales, Australia) featured by the presence of vast floodplains. For an automatic applications of this approach, a Matlab-tool (RiBEST, see Paragraph 2.2) is developed, exploiting only the river channel shapfile and a DEM of the survey area. In this work, SRTM has been selected for its high spatial resolution (i.e. 30 m) suitable for a quite realistic representation of cross-sections profile. Generally, SB approach proves to be suitable in the description of the submerged part, providing evident improvements to original SRTM information (see Table 2.2). Moreover, hydraulic parameters (i.e., flow area, hydraulic radius) are evaluated, proving representative of the real ones (see Figures 2.8, 2.9). The benefits of river bathymetry knowledge is evident also in the hydraulic modelling. The SRTM cross-sections modified by means of RiBEST are exploited to implement i) two 1-D hydraulic models for Po and Limpopo River, ii) a 2-D hydraulic model for Clarence River. In both cases, the outcomes are encouraging.

Secondly, the research refers to the assessment of DA approaches for river discharge estimation. In particular, a 4D-Var method is exploited, based solely on space-borne information (i.e. water surface elevations from SWOT) and global available data (i.e. prior discharge value from WBM). In order to assess how the bathymetry knowledge impact on the DA discharge estimation, the hydraulic model (i.e. SIC^2) is implemented on the cross-sections profiles derived from SRTM modified with RiBEST tool (see Paragraph 2.2) for a 132-km stretch of Po River. The results show a good representation of low flows (i.e. 0 - 2000 m^3/s), while a general underestimation of discharge peaks is evident. Also the Strickler coefficient is simultaneously estimated with river discharge. It presents

a fluctuating trend along the study area, not providing a reliable global information of bed roughness. The limitations in DA estimation might be due to the inaccuracy introduced by the cross-section representation (i.e., SRTM integrated with RiBEST-derived bathymetry).

Thirdly, a comprehensive and cross-missions view of the potential of satellite altimetry mission for hydraulic modelling calibration is addressed. Moreover, Multi-Mission series (MM), combining information provided by all single-missions, are proposed to overcome of temporal resolution and series length limitations. Generally, altimetry time series prove to be suitable in reproducing the observed water levels, in particular Sentinel-3B and Jason 2, while MM series ensures a uniform behaviour along the study area. Moreover, J2 series ensure trustworthiness and reliability on the calibration process with the lower temporal observation extent: lower than 1 year of data ($\sim$ 30 observations). Regarding the MM approach, it provides better results in term of calibration reliability than those obtained by series of low frequency satellites (i.e., E, SA) that cover very short period (e.g. $1 \div 2$ observation period; 20-40 months). On the other hand, in the case of higher temporal observation frequency (i.e., J2, J3), the use of original series is recommended. That said, MM series ensure a higher spatial coverage of the river, which could be significant when referring to long river stretch and single altimetry missions characterized by long inter-track distances.

The Part 2 illustrates an example of monitoring activities for the environmental conservation and protection of the Monate Lake, located in Varese (Italy). Exploiting the information provided by a dense monitoring network built in 2013, this work is dedicated to the implementation of a semi-distributed conceptual model for a basin with seasonally variable catchment size. In particular, previous studies (i.e. Barnaba, 1987) have investigated the presence of an groundwater catchment located East of the Monate Lake. The HyMOD model (called "H") is exploited as hydrological model, suitable for reproducing the spatial variability of basin storage capacity. In this work an extension of this original model is proposed (called "H4"), considering the groundwater catchment extent variable and closely linked to the rainfall seasonality. The outcomes of the two formulations (H and H4) show similar capabilities in reproducing the lake dynamics, suggesting that the modification of the original model setting (H) does not provide significant benefits.

In conclusion, this Thesis provides an overview of innovative methodologies for the estimation of hydraulic variables. In particular, the analysis performed in this work underline the added value of the satellite data in hydraulic fields, representing a valid alternative to the in-situ measurements.

List of Acronyms

1-D one-dimensional

2-D two-dimensional

AdBPo Autorità di Bacino Distrettuale del Fiume Po

AIPO Agenzia Interregionale per il Fiume Po

ARPAL Agenzia Regionale per la Protezione dell'Ambiente Lombardia

ASTER Advanced Spaceborne Thermal Emission and Reflection Radiometer

CNSE Centre National D'Etudes Spatiales

CSA Canadian Space Agency

CSI Critical Success Index

DA Data Assimilation

DEM Digital Elevation Model

DTM Digital Terrain Model

ERS Emergency Recovery System

F.O. Objective Function

FAO Food and Agricultural Organization

GA Genetic Algorithm

GIS Geographic Information System

GPS Global Positioning System

GRDC Global Runoff Data Centre

HEC-RAS Hydrologic Engineering Center's River Analysis System

ICEsat Ice, Cloud and land Elevation Satellite

IRSTEA Institut national de recherche en sciences et technologies pour l'environnement et l'agriculture

JMP Joint Monitoring Programme

LiDAR Light Detection and Ranging

MAE Mean Absolute Error

ME Mean Error

MODIS MODerate resolution Imaging Spectroradiometer

NWIS National Water Information System

NASA National Aeronautics and Space Administration

NGA National Geospatial-Intelligence Agency

NRFA National River Flow Archive

NRMSE Normalized Root Mean Square Error

NSE Nash-Sutcliffe Efficiency

PDM Probability Distributed Model

PIV Particle Image Velocimetry

RADAR Radio Detection and Ranging

RMSE Root Mean Square Error

rRMSE relative Root Mean Square Error

RST Robust Satellite Techniques

SAR Synthetic Aperture Radar

SD Standard Deviation

SEHM² Structural and Environmental Health Monitoring and Management

SIWI Swedish International Water Institute

SIC² Simulation and Integration of Controls for Channels

SRTM Shuttle Radar Topography Mission

SWOT Surface Water and Ocean Topography

UN United Nations

UNISDR United Nations International Strategy fro Disaster Reduction

USGS United States Geological Survey

VE Volumetric Efficiency

WBM Water Balance Model

WCED World Commission on Environment and Development

List of Figures

List of Tables

Bibliography

Alsdorf, D. E. and Lettenmaier, D. P. (2003). Tracking fresh water from space. *Science*, 301(5639):1491–1494.

Alsdorf, D. E., Rodríguez, E., and Lettenmaier, D. P. (2007). Measuring surface water from space. *Reviews of Geophysics*, 45(2).

Andreadis, K. M., Clark, E. A., Lettenmaier, D. P., and Alsdorf, D. E. (2007). Prospects for river discharge and depth estimation through assimilation of swath-altimetry into a raster-based hydrodynamics model. *Geophysical Research Letters*, 34(10).

Andreadis, K. M. and Schumann, G. J. (2014). Estimating the impact of satellite observations on the predictability of large-scale hydraulic models. *Advances in water resources*, 73:44–54.

Archer, L., Neal, J., Bates, P., and House, J. (2018). Comparing TanDEM-X data with frequently used DEMs for flood inundation modeling. *Water Resources Research*, 54(12):10–205.

Aronica, G., Tucciarelli, T., and Nasello, C. (1998). 2D multilevel model for flood wave propagation in flood-affected areas. *Journal of water resources planning and management*, 124(4):210–217.

Asch, M., Bocquet, M., and Nodet, M. (2016). *Data assimilation: methods, algorithms, and applications*. SIAM.

Baade, J. and Schmullius, C. (2016). TanDEM-X IDEM precision and accuracy assessment based on a large assembly of differential GNSS measurements in Kruger National Park, South Africa. *ISPRS Journal of Photogrammetry and Remote Sensing*, 119:496–508.

Barnaba (1987). Studio idrogeologico e ambientale del bacino del Lago di Monate (Varese).

Barzaghi, R., Borghi, A., Carrion, D., and Sona, G. (2007). Refining the estimate of the Italian quasi-geoid.

Bates, P. and Anderson, M. (1996). A preliminary investigation into the impact of initial conditions on flood inundation predictions using a time/space distributed sensitivity analysis. *Catena*, 26(1-2):115–134.

Bates, P. D., Horritt, M. S., and Fewtrell, T. J. (2010). A simple inertial formulation of the shallow water equations for efficient two-dimensional flood inundation modelling. *Journal of Hydrology*, 387(1-2):33–45.

Bates, P. D., Neal, J. C., Alsdorf, D., and Schumann, G. J.-P. (2013). Observing global surface water flood dynamics. In *The Earth's Hydrological Cycle*, pages 839–852. Springer.

Batini, C., Blaschke, T., Lang, S., Albrecht, F., Abdulmutalib, H., Barsi, Á., Szabó, G., and Kugler, Z. (2017). Data quality in remote sensing. *International Archives of the Photogrammetry, Remote Sensing & Spatial Information Sciences*, 42.

Baugh, C. A., Bates, P. D., Schumann, G., and Trigg, M. A. (2013). SRTM vegetation removal and hydrodynamic modeling accuracy. *Water Resources Research*, 49(9):5276–5289.

Bayes, T. (1763). An essay towards solving a problem in the doctrine of chances.

Beck, H. E., van Dijk, A. I., De Roo, A., Miralles, D. G., McVicar, T. R., Schellekens, J., and Bruijnzeel, L. A. (2016). Global-scale regionalization of hydrologic model parameters. *Water Resources Research*, 52(5):3599–3622.

Bertero, M., Boccacci, P., and Mainzer Koenig, A. (2001). Introduction to inverse problems in imaging. *OptPN*, 12(10):46–47.

Biancamaria, S., Lettenmaier, D. P., and Pavelsky, T. M. (2016). The SWOT mission and its capabilities for land hydrology. *Surveys in Geophysics*, 37(2):307–337.

Birkett, C. M. and Mason, I. M. (1995). A new global lakes database for a remote sensing program studying climatically sensitive large lakes. *Journal of Great Lakes Research*, 21(3):307–318.

Birkinshaw, S. J., O'donnell, G., Moore, P., Kilsby, C., Fowler, H., and Berry, P. (2010). Using satellite altimetry data to augment flow estimation techniques on the Mekong River. *Hydrological Processes*, 24(26):3811–3825.

Bjerklie, D. M., Dingman, S. L., and Bolster, C. H. (2005). Comparison of constitutive flow resistance equations based on the Manning and Chezy equations applied to natural rivers. *Water resources research*, 41(11).

Bjerklie, D. M., Dingman, S. L., Vorosmarty, C. J., Bolster, C. H., and Congalton, R. G. (2003). Evaluating the potential for measuring river discharge from space. *Journal of Hydrology*, 278(1-4):17–38.

Boergens, E., Nielsen, K., Andersen, O. B., Dettmering, D., and Seitz, F. (2017). River levels derived with CryoSat-2 SAR data classification—A case study in the Mekong River Basin. *Remote Sensing*, 9(12):1238.

Boyle, D. (2001). Multicriteria calibration of hydrologic models. *PhD dissertation, Department of Hydrology and Water Resources Engineering, The University of Arizona.*

Brivio, P., LECHI-LECHI, G., and Zilioli, E. (2006). *Principi e metodi di telerilevamento.* CittaStudi.

Bronstert, A. (2003). Floods and climate change: interactions and impacts. *Risk Analysis: An International Journal*, 23(3):545–557.

Brown, C. G., Sarabandi, K., and Pierce, L. E. (2009). Model-based estimation of forest canopy height in red and Austrian pine stands using shuttle radar topography mission and ancillary data: A proof-of-concept study. *IEEE transactions on geoscience and remote sensing*, 48(3):1105–1118.

Buffington, J. M. (2012). Changes in channel morphology over human time scales [Chapter 32]. *In: Church, Michael; Biron, Pascale M.; Roy, Andre G., eds. Gravel-Bed Rivers: Processes, Tools, Environments. Chichester, UK: Wiley. p. 435-463.*, pages 435–463.

Camorani, G., Filippi, F., Cavazzini, A., Lombardo, G., Pappani, G., and Forlani, G. (2006). Il rilievo altimetrico e batimetrico del fiume Po nel tratto tra confluenza Ticino e l'incile. In *X Asita Nat. Conf.(in Italian).*

Campbell, J. B. and Wynne, R. H. (2011). *Introduction to remote sensing.* Guilford Press.

Carrassi, A., Bocquety, M., Bertino, L., and Evensenz, G. (2018). Data Assimilation in the Geosciences An overview on methods, issues and perspectives.

Castellarin, A., Domeneghetti, A., and Brath, A. (2011). Identifying robust large-scale flood risk mitigation strategies: A quasi-2D hydraulic model as a tool for the Po river. *Physics and Chemistry of the Earth, Parts A/B/C*, 36(7-8):299–308.

Castiglioni, S., Lombardi, L., Toth, E., Castellarin, A., and Montanari, A. (2010). Calibration of rainfall-runoff models in ungauged basins: A regional maximum likelihood approach. *Advances in Water Resources*, 33(10):1235–1242.

Cervi, F., Petronici, F., Castellarin, A., Marcaccio, M., Bertolini, A., and Borgatti, L. (2018). Climate-change potential effects on the hydrological regime of freshwater springs in the Italian Northern Apennines. *Science of the Total Environment*, 622:337–348.

Conner, J. T. and Tonina, D. (2014). Effect of cross-section interpolated bathymetry on 2D hydrodynamic model results in a large river. *Earth Surface Processes and Landforms*, 39(4):463–475.

Cretaux, J.-F., Berge-Nguyen, M., Calmant, S., Jamangulova, N., Satylkanov, R., Lyard, F., Perosanz, F., Verron, J., Samine Montazem, A., Le Guilcher, G., et al. (2018). Absolute calibration or validation of the altimeters on the Sentinel-3A and the Jason-3 over Lake Issykkul (Kyrgyzstan). *Remote Sensing*, 10(11):1679.

Cunge, J. A., Holly, F. M., and Verwey, A. (1980). Practical aspects of computational river hydraulics. *Advances in water resources*.

Di Baldassarre, G. and Montanari, A. (2009). Uncertainty in river discharge observations: a quantitative analysis. *Hydrology & Earth System Sciences*, 13(6).

Domeneghetti, A. (2016). On the use of SRTM and altimetry data for flood modeling in data-sparse regions. *Water Resources Research*, 52(4):2901–2918.

Domeneghetti, A., Carisi, F., Castellarin, A., and Brath, A. (2015a). Evolution of flood risk over large areas: Quantitative assessment for the Po river. *Journal of Hydrology*, 527:809–823.

Domeneghetti, A., Castellarin, A., and Brath, A. (2012). Assessing rating-curve uncertainty and its effects on hydraulic model calibration. *Hydrology and Earth System Sciences*, 16(4):1191.

Domeneghetti, A., Castellarin, A., Tarpanelli, A., and Moramarco, T. (2015b). Investigating the uncertainty of satellite altimetry products for hydrodynamic modelling. *Hydrological Processes*, 29(23):4908–4918.

Domeneghetti, A., Molari, G., Tourian, M. J., Tarpanelli, A., Behnia, S., Moramarco, T., Sneeuw, N., and Brath, A. (2021). Testing the use of single-and multi-mission satellite altimetry or the calibration of hydraulic models. *Advances in Water Resources*.

Domeneghetti, A., Tarpanelli, A., Brocca, L., Barbetta, S., Moramarco, T., Castellarin, A., and Brath, A. (2014). The use of remote sensing-derived water surface data for hydraulic model calibration. *Remote sensing of environment*, 149:130–141.

Durand, M., Andreadis, K. M., Alsdorf, D. E., Lettenmaier, D. P., Moller, D., and Wilson, M. (2008). Estimation of bathymetric depth and slope from data assimilation of swath altimetry into a hydrodynamic model. *Geophysical Research Letters*, 35(20).

Durand, M., Gleason, C., Garambois, P.-A., Bjerklie, D., Smith, L., Roux, H., Rodriguez, E., Bates, P. D., Pavelsky, T. M., Monnier, J., et al. (2016). An intercomparison of remote sensing river discharge estimation algorithms from measurements of river height, width, and slope. *Water Resources Research*, 52(6):4527–4549.

Egido, A. and Smith, W. H. (2016). Fully focused SAR altimetry: theory and applications. *IEEE Transactions on Geoscience and Remote Sensing*, 55(1):392–406.

Falorni, G., Teles, V., Vivoni, E. R., Bras, R. L., and Amaratunga, K. S. (2005). Analysis and characterization of the vertical accuracy of digital elevation models from the Shuttle Radar Topography Mission. *Journal of Geophysical Research: Earth Surface*, 110(F2).

Fewtrell, T. J., Duncan, A., Sampson, C. C., Neal, J. C., and Bates, P. D. (2011). Benchmarking urban flood models of varying complexity and scale using high resolution terrestrial LiDAR data. *Physics and Chemistry of the Earth, Parts A/B/C*, 36(7-8):281–291.

Frasson, R. P. d. M., Wei, R., Durand, M., Minear, J. T., Domeneghetti, A., Schumann, G., Williams, B. A., Rodriguez, E., Picamilh, C., Lion, C., et al. (2017). Automated river reach definition strategies: Applications for the surface water and ocean topography mission. *Water Resources Research*, 53(10):8164–8186.

Garambois, P.-A. and Monnier, J. (2015). Inference of effective river properties from remotely sensed observations of water surface. *Advances in Water Resources*, 79:103–120.

Gaultier, L., Ubelmann, C., and Fu, L.-L. (2017). SWOT Simulator Documentation.

Gauthier, P., Charette, C., Fillion, L., Koclas, P., and Laroche, S. (1999). Implementation of a 3D variational data assimilation system at the Canadian Meteorological Centre. Part I: The global analysis. *Atmosphere-Ocean*, 37(2):103–156.

Gejadze, I. and Malaterre, P.-O. (2017). Discharge estimation under uncertainty using variational methods with application to the full saint-venant hydraulic network model. *International Journal for Numerical Methods in Fluids*, 83(5):405–430.

Gejadze, I., Oubanas, H., and Shutyaev, V. (2017). Implicit treatment of model error using inflated observation-error covariance. *Quarterly Journal of the Royal Meteorological Society*, 143(707):2496–2508.

Gejadze, I. Y. and Malaterre, P.-O. (2016). Design of the control set in the framework of variational data assimilation. *Journal of Computational Physics*, 325:358–379.

Giustarini, L., Vernieuwe, H., Verwaeren, J., Chini, M., Hostache, R., Matgen, P., Verhoest, N. E., and De Baets, B. (2015). Accounting for image uncertainty in SAR-based flood mapping. *International journal of applied earth observation and geoinformation*, 34:70–77.

Gleason, C. J. and Hamdan, A. N. (2017). Crossing the (watershed) divide: Satellite data and the changing politics of international river basins. *The Geographical Journal*, 183(1):2–15.

Gleason, C. J. and Smith, L. C. (2014). Toward global mapping of river discharge using satellite images and at-many-stations hydraulic geometry. *Proceedings of the National Academy of Sciences*, 111(13):4788–4791.

Grimaldi, S., Li, Y., Walker, J., and Pauwels, V. (2018). Effective representation of river geometry in hydraulic flood forecast models. *Water Resources Research*, 54(2):1031–1057.

Harmancioglu, N. B., Ozkul, S. D., Fistikoglu, O., and Geerders, P. (2003). *Integrated technologies for environmental monitoring and information production*, volume 23. Springer Science & Business Media.

Hawker, L., Rougier, J., Neal, J., Bates, P., Archer, L., and Yamazaki, D. (2018). Implications of simulating global digital elevation models for flood inundation studies. *Water resources research*, 54(10):7910–7928.

Hilton, J. (2017). GEM Geospatial Editor. *v1. CSIRO. Software Collection. https://doi.org/10.4225/08/5a1611629ab3d.*

Honnorat, M., Monnier, J., and Le Dimet, F.-X. (2009). Lagrangian data assimilation for river hydraulics simulations. *Computing and Visualization in Science*, 12(5):235–246.

Hosch, W. (2017). Genetic algorithm.

Huxley, C. and Farr, A. (2013). Lower Clarence Flood Model Update 2013. *Brisbane (Australia): BMT WBM Ltd.*

Iwahashi, J., Yamazaki, D., Matsuoka, M., Thamarux, P., Herrick, J., Yong, A., and Mital, U. (2017). Global terrain classification using Multiple-Error-Removed Improved-Terrain (MERIT) to address susceptibility of landslides and other geohazards. *AGUFM*, 2017:NH43A–0207.

Jiang, L., Madsen, H., and Bauer-Gottwein, P. (2019). Simultaneous calibration of multiple hydrodynamic model parameters using satellite altimetry observations of water surface elevation in the Songhua River. *Remote sensing of environment*, 225:229–247.

Kinzel, P. J. and Legleiter, C. J. (2019). sUAS-based remote sensing of river discharge using thermal particle image velocimetry and bathymetric lidar. *Remote Sensing*, 11(19):2317.

Kleinherenbrink, M., Naeije, M., Slobbe, C., Egido, A., and Smith, W. (2020). The performance of CryoSat-2 fully-focussed SAR for inland water-level estimation. *Remote Sensing of Environment*, 237:111589.

Koch, A., Heipke, C., and Lohmann, P. (2002). Analysis of SRTM DTM–Methodology and practical results. In *International Archives of the Photogrammetry Remote Sensing and Spatial Information Sciences, Com. IV*. Citeseer.

Laplace, P.-S. (1820). Théorie analytique des probabilités.

Legleiter, C. J. and Kinzel, P. J. (2020). Inferring Surface Flow Velocities in Sediment-Laden Alaskan Rivers from Optical Image Sequences Acquired from a Helicopter. *Remote Sensing*, 12(8):1282.

Legleiter, C. J., Pavelsky, T., Durand, M., Allen, G. H., Tarpanelli, A., Frasson, R., Guneralp, I., and Woodget, A. (2020). Editorial for the Special Issue "Remote Sensing of Flow Velocity, Channel Bathymetry, and River Discharge".

Legleiter, C. J. and Roberts, D. A. (2009). A forward image model for passive optical remote sensing of river bathymetry. *Remote Sensing of Environment*, 113(5):1025–1045.

Leopold, L. B. and Maddock, T. (1953). *The hydraulic geometry of stream channels and some physiographic implications*, volume 252. US Government Printing Office.

Leuci, R. (2017). Modellazione numerica semi-distribuita del comportamento idrologico del lago di Monate (VA). *Master Degree Thesis*.

Li, D., Andreadis, K. M., Margulis, S. A., and Lettenmaier, D. P. (2020). A data assimilation framework for generating space-time continuous daily SWOT river discharge data products. *Water Resources Research*, 56(6):e2019WR026999.

Liang, J., Yang, Q., Sun, T., Martin, J., Sun, H., and Li, L. (2015). MIKE 11 model-based water quality model as a tool for the evaluation of water quality management plans. *Journal of Water Supply: Research and Technology—AQUA*, 64(6):708–718.

Lombardi, L., Toth, E., Castellarin, A., Montanari, A., and Brath, A. (2012). Calibration of a rainfall–runoff model at regional scale by optimising river discharge statistics: Performance analysis for the average/low flow regime. *Physics and Chemistry of the Earth, Parts A/B/C*, 42:77–84.

Lorenc, A. C. (1986). Analysis methods for numerical weather prediction. *Quarterly Journal of the Royal Meteorological Society*, 112(474):1177–1194.

Loucks, D. P. and Van Beek, E. (2005). Water Resources Systems Planning and Management-Exercises.

Ludwig, R. and Schneider, P. (2006). Validation of digital elevation models from SRTM X-SAR for applications in hydrologic modeling. *ISPRS Journal of Photogrammetry and Remote Sensing*, 60(5):339–358.

Luino, F., Cirio, C. G., Biddoccu, M., Agangi, A., Giulietto, W., Godone, F., and Nigrelli, G. (2009). Application of a model to the evaluation of flood damage. *Geoinformatica*, 13(3):339–353.

Malaterre, P.-O., Dorchies, D., and Baume, J.-P. (2014). Estimation of offtake discharge and cross-device parameters using data assimilation for the automatic control of an irrigation canal.

Matgen, P., Hostache, R., Schumann, G., Pfister, L., Hoffmann, L., and Savenije, H. (2011). Towards an automated SAR-based flood monitoring system: Lessons learned from two case studies. *Physics and Chemistry of the Earth, Parts A/B/C*, 36(7-8):241–252.

Mazzoleni, M., Bacchi, B., Barontini, S., Di Baldassarre, G., Pilotti, M., and Ranzi, R. (2014). Flooding hazard mapping in floodplain areas affected by piping breaches in the po river, italy. *Journal of Hydrologic Engineering*, 19(4):717–731.

Mazzoleni, M., Paron, P., Reali, A., Juizo, D., Manane, J., Brandimarte, L., et al. (2020). Testing uav-derived topography for hydraulic modelling in a tropical environment. *Natural Hazards: Journal of the International Society for the Prevention and Mitigation of Natural Hazards*, 103(1):139–163.

Mersel, M. K., Smith, L. C., Andreadis, K. M., and Durand, M. T. (2013). Estimation of river depth from remotely sensed hydraulic relationships. *Water Resources Research*, 49(6):3165–3179.

Merwade, V., Cook, A., and Coonrod, J. (2008). GIS techniques for creating river terrain models for hydrodynamic modeling and flood inundation mapping. *Environmental Modelling & Software*, 23(10-11):1300–1311.

Merz, B., Kreibich, H., Schwarze, R., and Thieken, A. (2010). Review article'Assessment of economic flood damage'. *Natural Hazards and Earth System Sciences (NHESS)*, 10(8):1697–1724.

Milzow, C., Krogh, P. E., and Bauer-Gottwein, P. (2011). Combining satellite radar altimetry, SAR surface soil moisture and GRACE total storage changes for hydrological model calibration in a large poorly gauged catchment. *Hydrology & Earth System Sciences*, 15(6).

Montanari, A. and Castellarin, A. (2012). Piano di Monitoraggio Ambientale delle Attività Estrattive presso Cava Faraona e del Lago di Monate (Varese).

Moore, R. (2007). The PDM rainfall-runoff model.

Moore, R. and Clarke, R. (1981). A distribution function approach to rainfall runoff modeling. *Water Resources Research*, 17(5):1367–1382.

Moramarco, T., Barbetta, S., Bjerklie, D. M., Fulton, J. W., and Tarpanelli, A. (2019). River bathymetry estimate and discharge assessment from remote sensing. *Water Resources Research*, 55(8):6692–6711.

Moramarco, T., Corato, G., Melone, F., and Singh, V. P. (2013). An entropy-based method for determining the flow depth distribution in natural channels. *Journal of hydrology*, 497:176–188.

Moramarco, T. and Singh, V. P. (2010). Formulation of the entropy parameter based on hydraulic and geometric characteristics of river cross sections. *Journal of Hydrologic Engineering*, 15(10):852–858.

Neal, J., Schumann, G., and Bates, P. (2012a). A simple model for simulating river hydraulics and floodplain inundation over large and data sparse areas. *Water Resour Res*, 48.

Neal, J., Schumann, G., and Bates, P. (2012b). A subgrid channel model for simulating river hydraulics and floodplain inundation over large and data sparse areas. *Water Resources Research*, 48(11).

Neal, J., Schumann, G., Bates, P., Buytaert, W., Matgen, P., and Pappenberger, F. (2009). A data assimilation approach to discharge estimation from space. *Hydrological Processes: An International Journal*, 23(25):3641–3649.

Neal, J. C., Odoni, N. A., Trigg, M. A., Freer, J. E., Garcia-Pintado, J., Mason, D. C., Wood, M., and Bates, P. D. (2015). Efficient incorporation of channel cross-section geometry uncertainty into regional and global scale flood inundation models. *Journal of Hydrology*, 529:169–183.

O'Loughlin, F., Paiva, R., Durand, M., Alsdorf, D., and Bates, P. (2016). A multi-sensor approach towards a global vegetation corrected SRTM DEM product. *Remote Sensing of Environment*, 182:49–59.

O'Loughlin, F., Trigg, M., Schumann, G.-P., and Bates, P. (2013). Hydraulic characterization of the middle reach of the Congo River. *Water Resources Research*, 49(8):5059–5070.

Oubanas, H. (2018). Variational assimilation of satellite data into a full Saint-Venant based hydraulic model in the context of ungauged basins. *PhD Thesis*.

Oubanas, H., Gejadze, I., Malaterre, P.-O., Durand, M., Wei, R., Frasson, R. d. M., and Domeneghetti, A. (2018a). Discharge estimation in ungauged basins through variational data assimilation: The potential of the SWOT mission. *Water Resources Research*, 54(3):2405–2423.

Oubanas, H., Gejadze, I., Malaterre, P.-O., and Mercier, F. (2018b). River discharge estimation from synthetic SWOT-type observations using variational data assimilation and the full Saint-Venant hydraulic model. *Journal of Hydrology*, 559:638–647.

Paiva, R. C., Durand, M. T., and Hossain, F. (2015). Spatiotemporal interpolation of discharge across a river network by using synthetic SWOT satellite data. *Water Resources Research*, 51(1):430–449.

Pappenberger, F., Beven, K., Horritt, M., and Blazkova, S. (2005). Uncertainty in the calibration of effective roughness parameters in HEC-RAS using inundation and downstream level observations. *Journal of Hydrology*, 302(1-4):46–69.

Pasternack, G. B. and Senter, A. (2011). *21st Century Instream Flow Assessment Framework for Mountain Streams: Final Project Report*. California Energy Commission.

Pavelsky, T. and Durand, M. (2012). Developing new algorithms for estimating river discharge from space. *Eos, Transactions American Geophysical Union*, 93(45):457–457.

Pereira-Cardenal, S., Riegels, N., Berry, P., Smith, R., Yakovlev, A., Siegfried, T., and Bauer-Gottwein, P. (2011). Real-time remote sensing driven river basin modeling using radar altimetry. *Hydrology & Earth System Sciences*, 15(1).

Preissman, A. (1961). Propagation des intumescences dans les canaux et rivieres.

R Core Team (2019). *R: A Language and Environment for Statistical Computing*. R Foundation for Statistical Computing, Vienna, Austria.

Rabuffetti, A. (2012). Valutazioni geotecniche e idrogeologiche relative all'ampliamento della Cava "Holcim Italia spa" in località Faraona, nell'ambito della Gestione produttiva ATEc2.

Reali, A. (2018). Potentialities of Unmanned Aerial Vehicles in Hydraulic Modelling. *Master Degree Thesis*.

Ritchie, H. (2017). Water Use and Stress. *Our World in Data*. https://ourworldindata.org/water-use-stress.

Rodriguez, E., Morris, C. S., and Belz, J. E. (2006). A global assessment of the SRTM performance. *Photogrammetric Engineering & Remote Sensing*, 72(3):249–260.

Rogers, K., Knoll, E. J., Copeland, C., and Walsh, S. (2016). Quantifying changes to historic fish habitat extent on north coast NSW floodplains, Australia. *Regional Environmental Change*, 16(5):1469–1479.

Roux, H. and Dartus, D. (2004). Data assimilation applied to hydraulic parameter identification. In *British hydrological society international conference*, pages 354–361.

Schneider, R., Tarpanelli, A., Nielsen, K., Madsen, H., and Bauer-Gottwein, P. (2018). Evaluation of multi-mode CryoSat-2 altimetry data over the Po River against in situ data and a hydrodynamic model. *Advances in water resources*, 112:17–26.

Schumann, G., Bates, P. D., Horritt, M. S., Matgen, P., and Pappenberger, F. (2009). Progress in integration of remote sensing–derived flood extent and stage data and hydraulic models. *Reviews of Geophysics*, 47(4).

Schumann, G., Domeneghetti, A., et al. (2016). Exploiting the proliferation of current and future satellite observations of rivers. *Hydrological Processes*, 30(16):2891–2896.

Schumann, G. J.-P., Andreadis, K. M., and Bates, P. D. (2014). Downscaling coarse grid hydrodynamic model simulations over large domains. *Journal of Hydrology*, 508:289–298.

Schwatke, C., Dettmering, D., Börgens, E., and Bosch, W. (2015). Potential of SARAL/AltiKa for inland water applications. *Marine Geodesy*, 38(sup1):626–643.

Scrucca, L. (2013). GA: A package for genetic algorithms in R. *Journal of Statistical Software*, 53(4):1–37.

Shastry, A. and Durand, M. (2019). Utilizing Flood Inundation Observations to Obtain Floodplain Topography in Data-Scarce Regions. *Frontiers in Earth Science*, 6:243.

Smith, L. C. and Pavelsky, T. M. (2008). Estimation of river discharge, propagation speed, and hydraulic geometry from space: Lena River, Siberia. *Water Resources Research*, 44(3).

Soar, P. J., Wallerstein, N. P., and Thorne, C. R. (2017). Quantifying river channel stability at the basin scale. *Water*, 9(2):133.

Soligno, I. (2015). Modello numerico per il bilancio idrologico del Lago di Monate. *Master Degree Thesis*.

Stumpo, F. (2019). Indagine numerico-sperimentale finalizzata alla caratterizzazione del bacino imbrifero sotterraneo del Lago di Monate (VA). *Master Degree Thesis*.

Tarpanelli, A., Barbetta, S., Brocca, L., and Moramarco, T. (2013a). River discharge estimation by using altimetry data and simplified flood routing modeling. *Remote Sensing*, 5(9):4145–4162.

Tarpanelli, A., Brocca, L., Lacava, T., Faruolo, M., Melone, F., Moramarco, T., Pergola, N., and Tramutoli, V. (2011). River discharge estimation through MODIS data. In *Remote Sensing for Agriculture, Ecosystems, and Hydrology XIII*, volume 8174, page 817408. International Society for Optics and Photonics.

Tarpanelli, A., Brocca, L., Lacava, T., Melone, F., Moramarco, T., Faruolo, M., Pergola, N., and Tramutoli, V. (2013b). Toward the estimation of river discharge variations using MODIS data in ungauged basins. *Remote Sensing of Environment*, 136:47–55.

Tarpanelli, A., Brocca, L., Melone, F., and Moramarco, T. (2013c). Hydraulic modelling calibration in small rivers by using coarse resolution synthetic aperture radar imagery. *Hydrological Processes*, 27(9):1321–1330.

Tomesani, G. (2016). Modelli numerici del comportamento idrologico del lago di Monate (VA): possibili schemi concettuali e strategie di calibratione. *Master Degree Thesis*.

Tourian, M., Elmi, O., Chen, Q., Devaraju, B., Roohi, S., and Sneeuw, N. (2015). A spaceborne multisensor approach to monitor the desiccation of Lake Urmia in Iran. *Remote Sensing of Environment*, 156:349–360.

Tourian, M., Tarpanelli, A., Elmi, O., Qin, T., Brocca, L., Moramarco, T., and Sneeuw, N. (2016). Spatiotemporal densification of river water level time series by multimission satellite altimetry. *Water Resources Research*, 52(2):1140–1159.

Tourian, M. J., Elmi, O., Mohammadnejad, A., and Sneeuw, N. (2017). Estimating river depth from SWOT-Type observables obtained by satellite altimetry and imagery. *Water*, 9(10):753.

Trigg, M. A., Wilson, M. D., Bates, P. D., Horritt, M. S., Alsdorf, D. E., Forsberg, B. R., and Vega, M. C. (2009). Amazon flood wave hydraulics. *Journal of Hydrology*, 374(1-2):92–105.

Vignudelli, S., Birol, F., Benveniste, J., Fu, L.-L., Picot, N., Raynal, M., and Roinard, H. (2019). Satellite altimetry measurements of sea level in the coastal zone. *Surveys in Geophysics*, 40(6):1319–1349.

Wang, F., Polcher, J., Peylin, P., and Bastrikov, V. (2018). Assimilation of river discharge in a land surface model to improve estimates of the continental water cycles. *Hydrology & Earth System Sciences*, 22(7).

Weise, T. (2009). Global optimization algorithms-theory and application. *Self-Published Thomas Weise*.

Wisser, D., Frolking, S., Douglas, E. M., Fekete, B. M., Schumann, A. H., and Vörösmarty, C. J. (2010). The significance of local water resources captured in small reservoirs for crop production–a global-scale analysis. *Journal of Hydrology*, 384(3-4):264–275.

Wood, M., Neal, J., Bates, P., et al. (2016). Calibration of channel depth and friction parameters in the LISFLOOD-FP hydraulic model using medium resolution SAR data and identifiability techniques. *Hydrology and Earth System Sciences*, 20(12):4983–4997.

Yamazaki, D., Ikeshima, D., Tawatari, R., Yamaguchi, T., O'Loughlin, F., Neal, J. C., Sampson, C. C., Kanae, S., and Bates, P. D. (2017). A high-accuracy map of global terrain elevations. *Geophysical Research Letters*, 44(11):5844–5853.

Yan, K., Tarpanelli, A., Balint, G., Moramarco, T., and Baldassarre, G. D. (2015). Exploring the potential of SRTM topography and radar altimetry to support flood propagation modeling: Danube case study. *Journal of Hydrologic Engineering*, 20(2):04014048.

Yuan, C., Gong, P., and Bai, Y. (2020). Performance Assessment of ICESat-2 Laser Altimeter Data for Water-Level Measurement over Lakes and Reservoirs in China. *Remote Sensing*, 12(5):770.